

AD_____

Award Number: W81XWH-12-1-0522

TITLE: Development and Testing of Iron Based Phantoms as Standards for the Diagnosis of Microbleeds and Oxygen Saturation with Applications in Dementia, Stroke, and Traumatic Brain Injury

PRINCIPAL INVESTIGATOR: Yu-Chung Norman Cheng

CONTRACTING ORGANIZATION: Wayne State University
Detroit, Michigan, 48202

REPORT DATE: October 2013

TYPE OF REPORT: Annual Report

PREPARED FOR: U.S. Army Medical Research and Materiel Command
Fort Detrick, Maryland 21702-5012

DISTRIBUTION STATEMENT: Approved for Public Release;
Distribution Unlimited

The views, opinions and/or findings contained in this report are those of the author(s) and should not be construed as an official Department of the Army position, policy or decision unless so designated by other documentation.

REPORT DOCUMENTATION PAGE				Form Approved OMB No. 0704-0188	
Public reporting burden for this collection of information is estimated to average 1 hour per response, including the time for reviewing instructions, searching existing data sources, gathering and maintaining the data needed, and completing and reviewing this collection of information. Send comments regarding this burden estimate or any other aspect of this collection of information, including suggestions for reducing this burden to Department of Defense, Washington Headquarters Services, Directorate for Information Operations and Reports (0704-0188), 1215 Jefferson Davis Highway, Suite 1204, Arlington, VA 22202-4302. Respondents should be aware that notwithstanding any other provision of law, no person shall be subject to any penalty for failing to comply with a collection of information if it does not display a currently valid OMB control number. PLEASE DO NOT RETURN YOUR FORM TO THE ABOVE ADDRESS.					
1. REPORT DATE October 2013		2. REPORT TYPE Annual Report		3. DATES COVERED 30September2012–29September2013	
4. TITLE AND SUBTITLE Development and Testing of Iron Based Phantoms as Standards for the Diagnosis of Microbleeds and Oxygen Saturation with Applications in Dementia, Stroke, and Traumatic Brain Injury				5a. CONTRACT NUMBER W81XWH-12-1-0522	
				5b. GRANT NUMBER W81XWH-12-1-0522	
				5c. PROGRAM ELEMENT NUMBER	
6. AUTHOR(S) Yu-Chung Norman Cheng E-Mail: yxc16@wayne.edu				5d. PROJECT NUMBER	
				5e. TASK NUMBER	
				5f. WORK UNIT NUMBER	
7. PERFORMING ORGANIZATION NAME(S) AND ADDRESS(ES) Wayne State University Detroit, Michigan, 48202				8. PERFORMING ORGANIZATION REPORT NUMBER	
9. SPONSORING / MONITORING AGENCY NAME(S) AND ADDRESS(ES) U.S. Army Medical Research and Materiel Command Fort Detrick, Maryland 21702-5012				10. SPONSOR/MONITOR'S ACRONYM(S)	
				11. SPONSOR/MONITOR'S REPORT NUMBER(S)	
12. DISTRIBUTION / AVAILABILITY STATEMENT Approved for Public Release; Distribution Unlimited					
13. SUPPLEMENTARY NOTES					
14. ABSTRACT Our first goal is to establish a standard protocol with accurate methods for the magnetic susceptibility quantifications of materials in straws that are further inserted in agar gel phantoms. In this first year, we have measured magnetic susceptibility values of four different concentrations of each of the following materials in distilled water from multiple echo gradient echo MR images: nanoparticles, gadolinium, calcium, and ferritin. We have used a high-pass filter, a quadratic fit program, a SHARP method, and our own algorithm to remove the background phase from each image. The SHARP method seems to be a reasonably good method, as the uncertainty resulted from the combined usages of SHARP and our CISSCO method is about 10% of each quantified susceptibility value. Our own algorithm in combination with the CISSCO method also leads to accurate susceptibility quantification. However, given the measured susceptibility based on phase distributions outside each straw, except for gadolinium solutions, the phase value inside each straw is usually at least 10% away from the expected value. As we know the uncertainty of each of our measurement, even a 10% deviation deserves our attention and will be important for the MRI community to be aware of these unexpected findings. We are trying to understand the causes. As a comparison, we have also measured the concentrations of nanoparticle and gadolinium solutions with ICP-AES.					
15. SUBJECT TERMS MRI, susceptibility quantification, gel phantoms, simulated brain images, numerical models, nanoparticles, gadolinium, ferritin, calcium, multiple concentrations, multiple echo times,					
16. SECURITY CLASSIFICATION OF:			17. LIMITATION OF ABSTRACT	18. NUMBER OF PAGES	19a. NAME OF RESPONSIBLE PERSON
a. REPORT	b. ABSTRACT	c. THIS PAGE			USAMRMC
U	U	U	UU	53	19b. TELEPHONE NUMBER (include area code)

Table of Contents

	<u>Page</u>
Introduction.....	4
Body.....	4-43
Key Research Accomplishments.....	44
Reportable Outcomes.....	45
Conclusion.....	45
References.....	46
Appendices.....	46-53

INTRODUCTION

Magnetic resonance imaging (MRI) offers a powerful, non-invasive means to image the human body. Recent advances in imaging the brain have led to the potential of monitoring iron build up, blood products in dementia, stroke, traumatic brain injury, and the measurement of oxygen saturation. These advances relate directly to both monitoring and measuring the amount of iron in brain tissues that have changes in magnetic susceptibility of each individual tissue. Therefore, the proper quantification of iron will play a key role in future radiology practice. While a number of groups using several methods are approaching this topic, the current problems are that no standard protocol has been established nor sensitivities and uncertainties of these methods have been properly evaluated. These methods include the background phase removal techniques. Without the standard protocol or understanding of uncertainties of developed methods, the quantified susceptibility values can be questionable. As a first step, we want to establish a standard protocol with accurate methods for the magnetic susceptibility quantifications of materials in phantoms. We have accurately quantified susceptibilities of several concentrations of four different materials in water with MRI. The detailed methods and results are presented below.

BODY

I. Phantom constructions

Our first step is to construct gel phantoms inserted with straws, in order to establish standards in the magnetic susceptibility quantification. Currently, we know that we can apply the 2D CISSCO (Complex Image Summation around a Spherical or a Cylindrical Object) method [Cheng et al., 2009], direct phase measurements (e.g., [Shen et al., 2008]), or $R2'$ measurements (e.g., [Haacke et al., 2005]) for susceptibility quantification of a given cylindrical object. In order to avoid partial volume and Gibbs ringing artifacts, the direct phase and $R2'$ measurements are better to be applied to cylindrical objects with diameters of more than 6 pixels. The 2D CISSCO method breaks through that limit.

We have obtained clear straws with three different diameters (roughly 3 mm, 5 mm, and 6 mm) and we also have straws with 4 different colors but all with diameters of 4 mm from the same manufacturer. It turned out that it was not that easy to obtain clear straws with different diameters from the same manufacturer, but we tried to do that in order to satisfy reviewers' request for this project. A general worry is that some straws may contain substances to influence our susceptibility quantification.

For our gel phantoms, we choose agar as the material. There are at least 5 different materials to make gel. Agar has one advantage as it becomes solid during the room temperature but gelatin (another material) will melt. However, this also means that we need to work with agar at a relatively high temperature (above 85 °C) and straws can melt at that temperature. Our experiments show that we can insert straws with liquid samples into agar solutions at around 75 °C without melting the straws. We also need to mix agar well when it is in the solution form. We have purchased a 4" long magnetic stir bar and it serves the purposes well.

For straws that are narrower than 5 mm, it is also a problem to place water or gel solution into those straws, due to the surface tension. We overcome this problem by covering both ends of each straw with wax. We pick a hole through wax at one of the ends and inject the liquid sample from the bottom end of each straw. Then we seal the hole with cement.

We have imaged several phantoms in order to examine the susceptibility effect due to the walls of straws. We fill each straw with the distilled water, as we expect minimal susceptibility difference between the distilled water and agar gel. In the following images and their associated tables, we show results from three phantoms acquired from the shortest and the longest echo times of an 11-echo SWI (susceptibility weighted imaging) sequence from our 3T MRI machine. The imaging resolution was 1 mm x 1 mm x 1 mm. The in-plane matrix size was 256 x 256. A total of 72 slices were acquired but only 64 were reconstructed, due to the choice of 12.5% oversampling. Repetition time TR was 37 ms and echo times ranged from 5.68 ms to 30.51 ms. Echo spacing was about 2.5 ms. Flip angle was 15°. The scan time was 11 min and 22 sec. A 32 x 32 high pass filter has been applied to phase images in the following examples. At the longest echo time, we can see very minor susceptibility effects from some straws, due to the walls of the straws. Some quick estimations of the

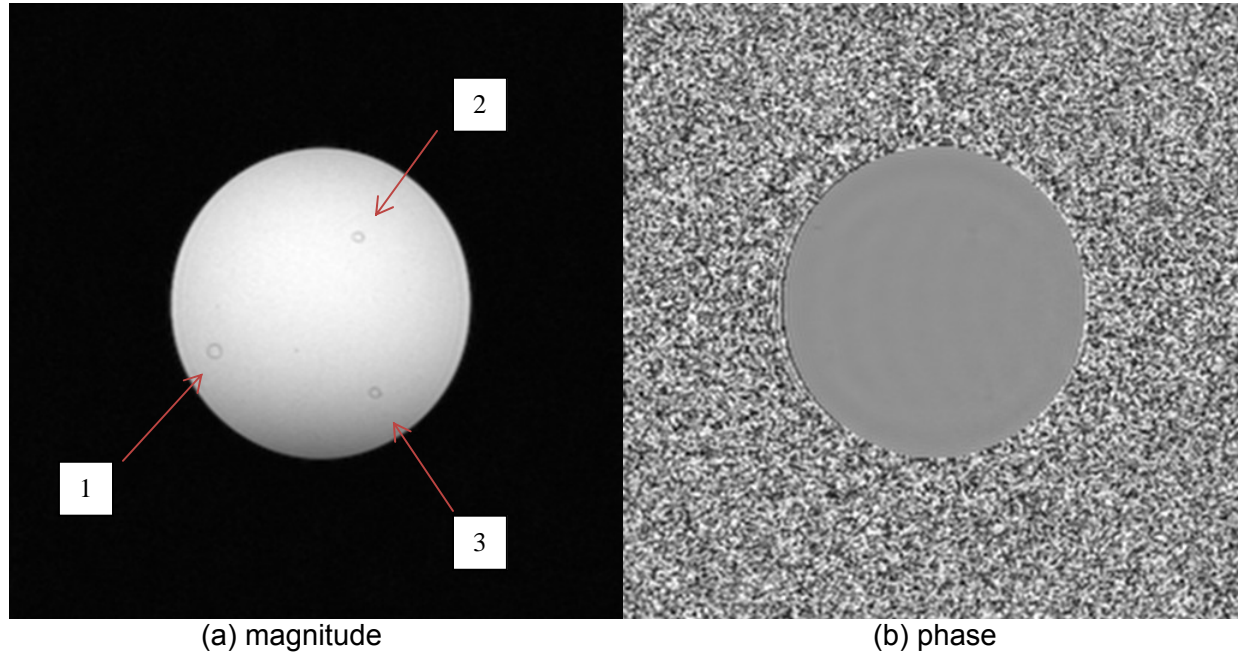
magnetic moments of the walls reveal that the values are around 3-5 radian*pixel². If we carefully examine the phase images, in general we see that smaller straws show some phase patterns in images. Thus, we choose to use straws with diameters of roughly 6.3 mm for our subsequent experiments, as those straws do not show any obvious susceptibility effect from the walls of straws.

Phantom 1: (Slice no. 33)

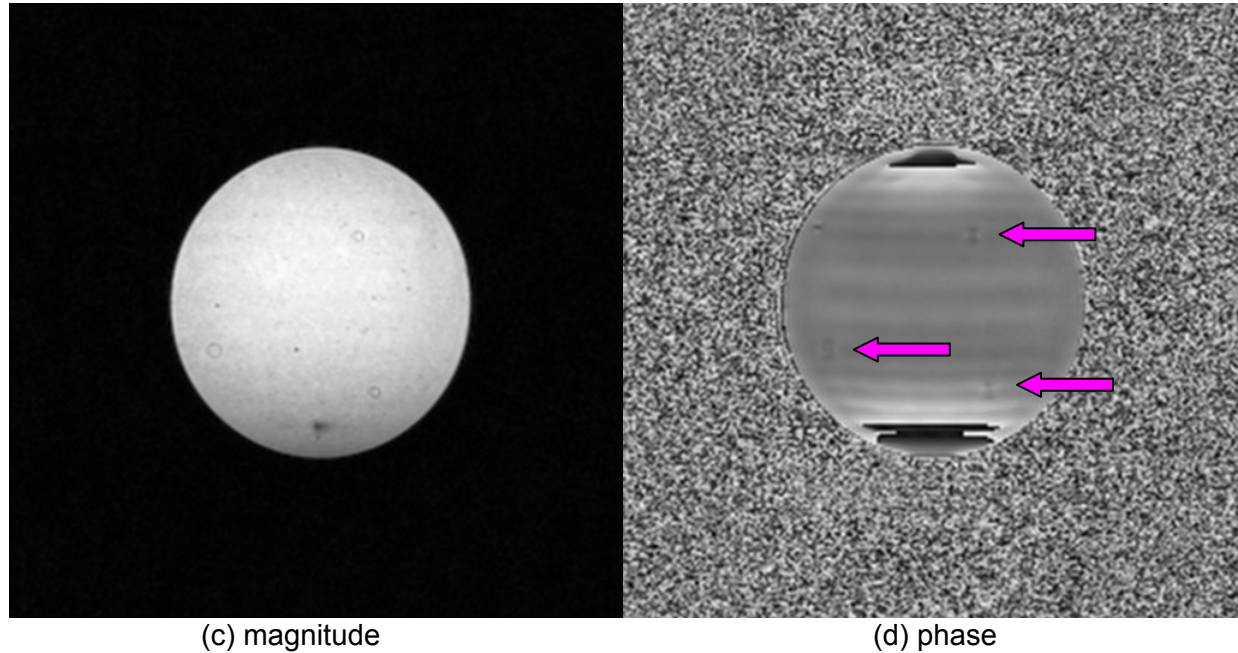
Straw info:

Straw No.	1	2	3
Color	Clear	Green	Orange
Diameter (mm)	5.99 ± 0.06	3.94 ± 0.05	3.90 ± 0.05

Echo time: 5.68 ms



Echo time: 30.51 ms

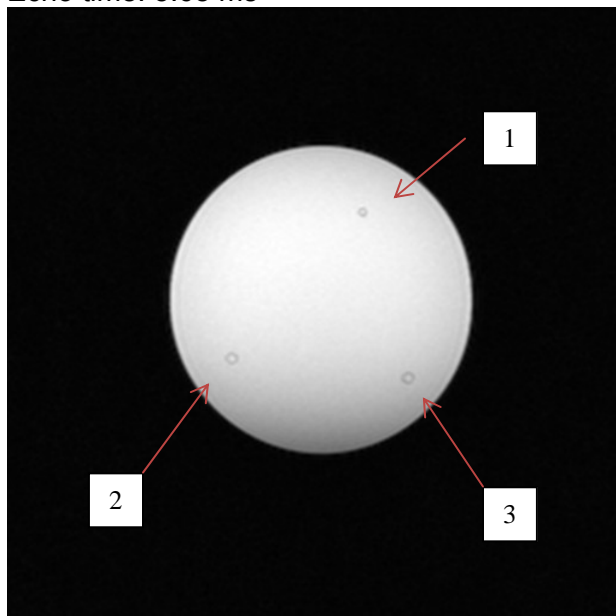


Phantom 2: (Slice no. 33)

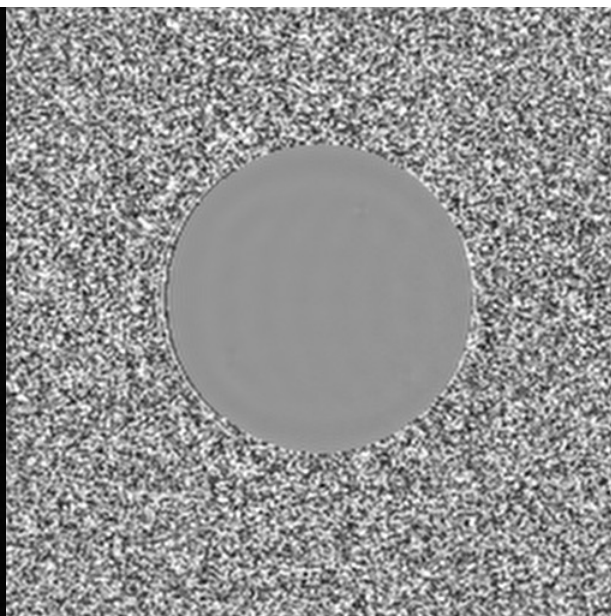
Straw info:

Straw No.	1	2	3
Color	Clear	Pink	Green
Diameter(mm)	2.63 ± 0.03	3.96 ± 0.05	3.94 ± 0.05

Echo time: 5.68 ms

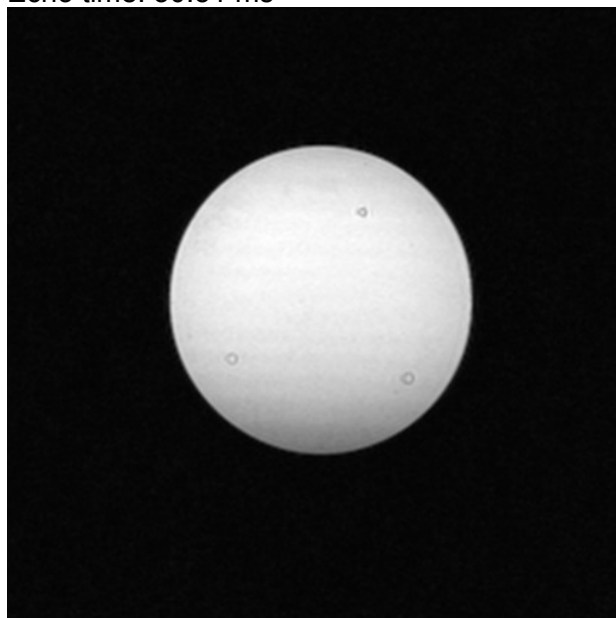


(e) magnitude

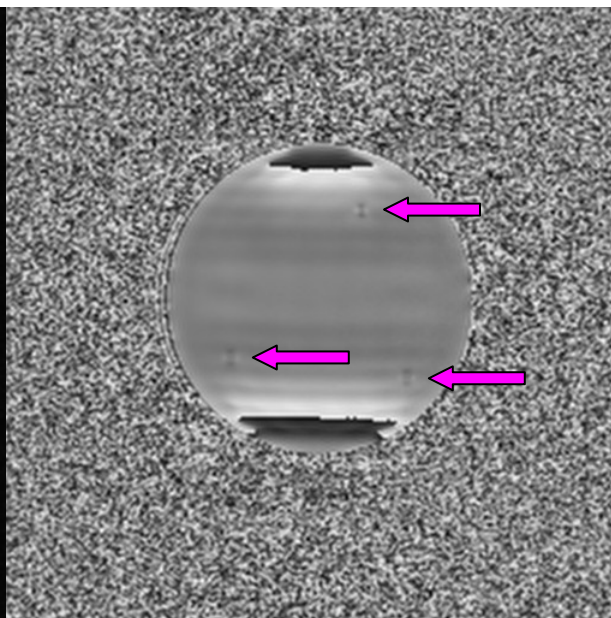


(f) phase

Echo time: 30.51 ms



(g) magnitude



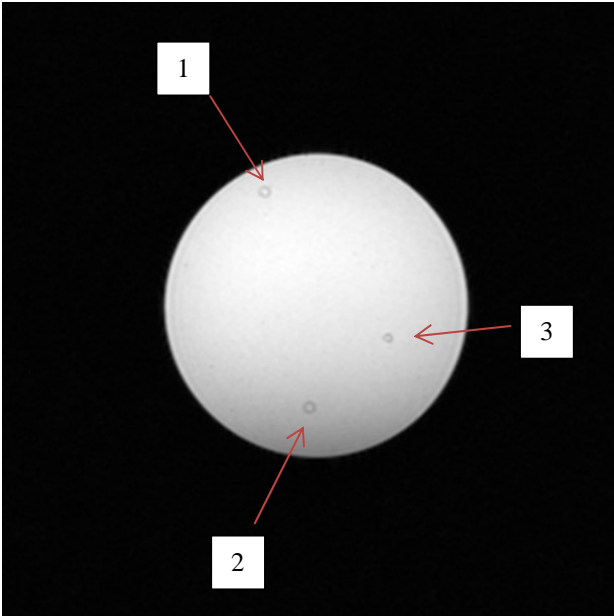
(h) phase

Phantom 3: (Slice no. 32)

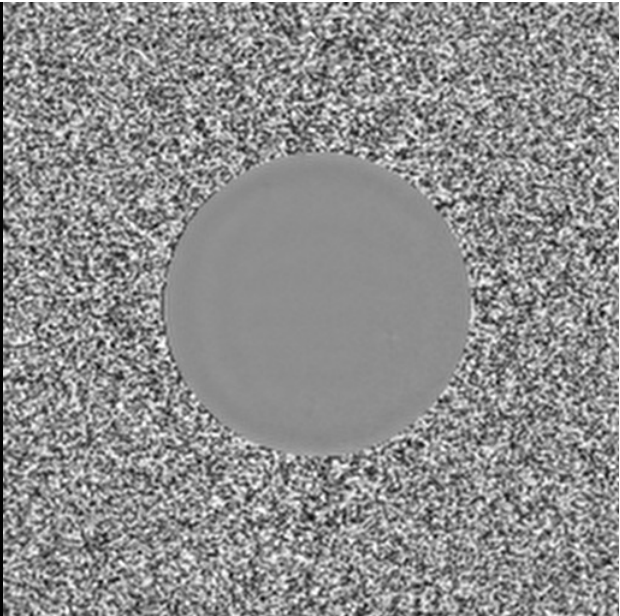
Straw info:

Straw No.	1	2	3
Color	Pink	Yellow	Clear
Diameter(mm)	3.96 ± 0.05	3.91 ± 0.05	2.63 ± 0.03

Echo time: 5.68 ms

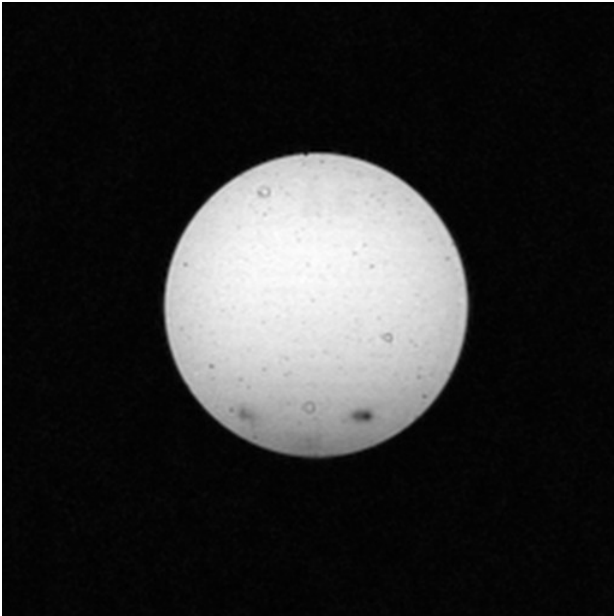


(i) magnitude

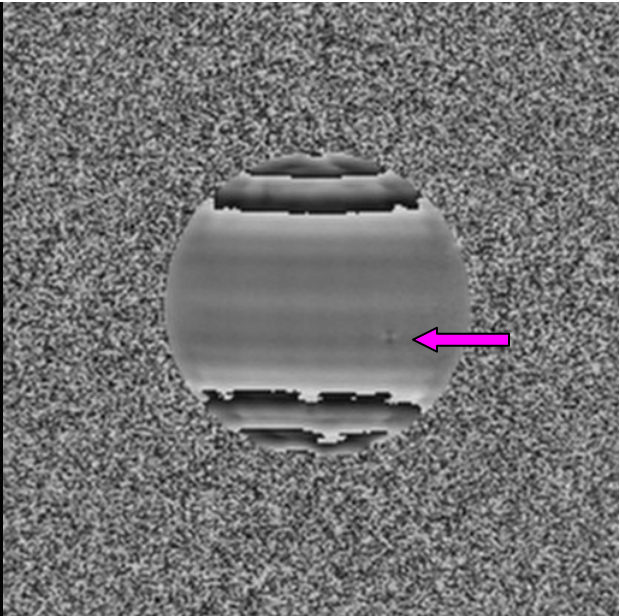


(j) phase

Echo time: 30.51 ms



(k) magnitude



(l) phase

II. Susceptibility and relaxation rate measurements from MRI and concentration measurements from ICP-AES

1) Sample preparations

We prepared several concentrations of nanoparticle, gadolinium, calcium, and ferritin solutions for measurements. Based on our experiences and results in the literature [Shen et al., 2008; Weisskoff and Kiihne, 1992; Zheng et al., 2013] or from sigma.com, the highest concentrations of nanoparticle, gadolinium, calcium, and ferritin solutions prepared by us were aimed at 25 mg/L of iron in nanoparticles, 927 mg/L of MR gadolinium contrast agent, 525 g/L of calcium, and 1455 mg/L of iron in ferritin, respectively. Except for nanoparticle solutions, these values would correspond to +2 ppm of magnetic susceptibility values relative to the susceptibility of water (which is -9.05 ppm in SI system). For nanoparticles, the 25 mg/L of iron would correspond to a relative susceptibility value of +1 ppm. In order to achieve these expected values, we first diluted the originally very high-concentrated nanoparticle solution, the MR contrast agent, and ferritin solution with distilled water. After creating those large-quantity batches, we further repeatedly diluted each solution with the distilled water by half of its previous concentration such that we produced at least four different concentrations for each of the four materials. For MRI experiments, we injected sufficient volume of each sample into a clear straw with a diameter of roughly 6.3 mm and sealed both ends of the straw. For each material, we placed 4 straws with different concentrations in one agar phantom. The remaining amount of each sample was stored in test tubes for inductively coupled plasma atomic emission spectrometer (ICP-AES), magnetometer, and any other future studies (when needed). Our plan was to measure each sample by MRI, ICP-AES, and a SQUID (superconducting quantum interference device) based magnetometer.

2) ICP-AES measurements

As our solutions have metallic concentrations in or above the mg/L range, it is more appropriate to measure our samples with ICP-AES. ICP-AES requires 2 ml of each sample and uses standard metallic concentrations as references to establish calibrations. Even at a very high concentration such as 850 mg/L, the quantified concentration can be differed by 1% from time to time. When the concentration is between 10 mg/L and 1 mg/L, the uncertainty is at least 10%. Below 1 mg/L, the uncertainty is more than 100%. We originally proposed to use inductively coupled plasma mass spectrometer (ICPMS) to measure metallic concentrations in solutions. However, ICPMS requires the concentration of each metallic content to be less than 0.2 mg/L. This means that we must dilute each sample for ICPMS measurements. This does not seem a problem in theory, but we prefer (and almost insist) to measure exactly the same sample by different techniques. In fact, we later found out from ICP-AES measurements that when the dilution of a sample was by a factor of 100, we easily observed at least 10% deviation from the concentration of the undiluted sample.

For nanoparticle measurements by ICP-AES, we were told that we need to "digest" the samples i.e., to break iron atoms inside each nanoparticle. Otherwise the measured concentration can be far less than the actual concentration of iron. This means, we need to add concentrated nitric acid to each of our nanoparticle samples for hours or days, and then dilute each sample such that the concentration of nitric acid is less than 5%. We have measured several nanoparticles concentrations by ICP-AES with and without "digestion." Surprisingly, ICP-AES consistently showed that each digested solution had a lower concentration than its undigested counterpart. This is completely contradicting to theory and we suspect that the problem may be due to dilutions. In the results below, we show the measurements of ICP-AES from undigested nanoparticle solutions. Digestion is not needed for the gadolinium MRI contrast agent or ferritin. However, as the concentrations of ferritin solutions are higher than the ICP-AES detection limits and the ICP-AES machine is currently under repair, we will simply rely on the concentration of the reference ferritin solution purchased from sigma.com. Similarly, the concentrations of calcium solutions are very very high. We thus can estimate the concentrations by weighing the amount of CaCl_2 (also purchased from sigma.com) and the amount of distilled water. The uncertainty of each estimated concentration for calcium solutions is about 10%.

3) MRI parameters and considerations of image analysis

We have imaged our phantoms on a 3 T Siemens Verio machine with a 3D 11-echo SWI sequence and a 2D 14-echo spin echo sequence without an echo train length. These two sequences allowed us to quantify

susceptibility and relaxation rates $R2^*$ and $R2$, respectively. As a 12-channel radiofrequency (rf) coil was used, it would be better to analyze images from each rf channel. Our best choice was to analyze the k-space data of four channels output from 3 T software. We also imaged each phantom with these sequences at two orientations, when straws were perpendicular and parallel to the main field. The in-plane imaging resolutions for both sequences were 1 mm x 1 mm. The in-plane matrix size was 256 x 256. For SWI, repetition time TR was 37 ms and echo times ranged from 5.68 ms to 29.48 ms, with an echo spacing of 2.38 ms. Flip angle was 15°. A total of 72 slices with slice thickness 1 mm were acquired but only 64 were reconstructed, due to the choice of 12.5% oversampling. The scan time was 11 min and 22 sec. A 32 x 32 high pass filter with the Hanning window to smooth data in k-space was applied to phase images as one of the means to remove the background phase before susceptibility quantifications. Later we will show results from other background phase removal method. For the 14-echo spin echo sequence, the echo time ranged from 12 ms to 168 ms with an echo spacing of 12 ms. The repetition time TR was 300 ms. Only the middle 4 slices with slice thickness of 4 mm were acquired. The scan time per slice was about 76 sec such that the total scan time for this spin echo sequence was about 5 min 4 sec. We have noted that the actual field strength of our Verio machine is 2.89 T.

To quantify susceptibility values, as a standard procedure, we typically applied our 2D CISSCO method to straws from the central slice of an SWI dataset. We applied the CISSCO method to other slices when we wanted to check whether the quantified susceptibility values were consistent throughout the entire phantom. The current CISSCO method provides us the measurements of magnetic moment and its uncertainty from each straw. Then we can calculate the susceptibility value of each sample by dividing the magnetic moment by cross section of each straw, as we have measured the inner diameter and outer diameter of each type of straw with a Vernier calibrator. In addition, for our susceptibility quantification of an intended sample inside a straw, we tried to choose the phase image from an rf channel with the highest intensity around the straw in its corresponding magnitude image. This is to reduce the Gaussian noise around the straw of interest in the phase image. However, the final magnitude image for the CISSCO analysis was the sum-of-squares magnitude image from all four channels. This is to minimize the magnitude intensity variation around the straw and the error of susceptibility quantification.

4) Susceptibility quantification of Fe_3O_4 nanoparticles

Figures 1 and 2 show two phantoms with 4 straws and 3 straws, respectively, filled by 7 different concentrations of Fe_3O_4 nanoparticles. The high pass filter has been applied to phase images. We quantified the susceptibility values of straws directly from complex images with TE of 15.24 ms and we were able to achieve reasonably accurate measurements, as listed in Table 1. The phase pattern of the 5th straw in Fig. 2 also indicates that we can quantify its susceptibility. We do not show that result here due to the large error. If we can properly remove the background field from phase images at longer echo times, we can reduce the uncertainty of each measured susceptibility value from our CISSCO method. Similarly, the uncertainty of a quantified susceptibility value is smaller if the susceptibility value is larger.

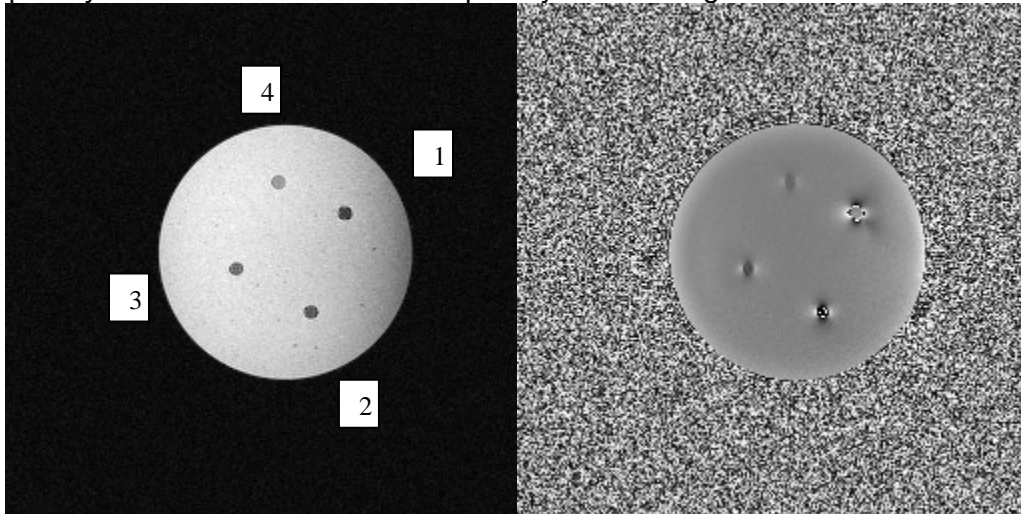


Figure 1: Coronal magnitude (left panel) and filtered phase (right panel) images of nanoparticles with concentrations #1, #2, #3, and #4. This set of image was acquired from echo time 15.24 ms and slice No. 33.

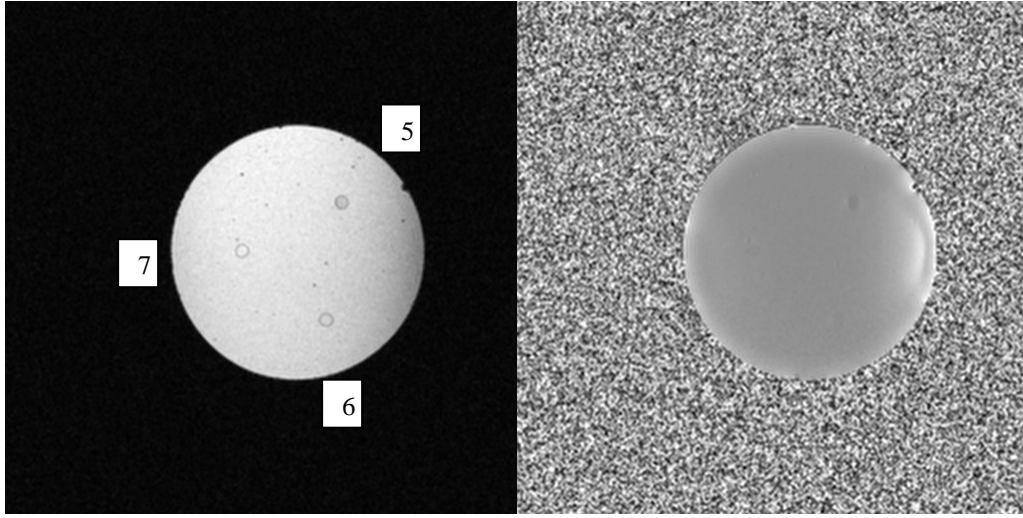


Figure 2: Coronal magnitude (left panel) and filtered phase (right panel) images of nanoparticles with concentration #5, #6, and #7. This set of image was acquired from echo time 15.24 ms and slice No. 33.

The quantified results from ICP-AES and MRI for the first 4 straws are listed in Table 1. Given our experimental findings mentioned above, we assume no susceptibility effect from the straw walls for the susceptibility ($\Delta\chi$) quantification. The linear fit between the ICP-AES and MRI susceptibility measurements is shown in Fig. 3. For the straws shown in Fig. 2, we have tried to select different echo times for susceptibility quantifications of different straws, in order to obtain sufficient phase distributions around each straw. Reliable quantification of low susceptibility values from those straws requires a background removal procedure that we continue to work on.

No.	Conc (mg/L)	$\Delta\chi$ (ppm)	$\delta(\Delta\chi)/\Delta\chi$ (%)
1	25.70	1.08	3.8
2	12.59	0.56	4.3
3	6.80	0.25	8.3
4	3.00	0.12	17.3

Table 1: Quantified results from ICP-AES and MRI for different concentrations of nanoparticles. The first column labels each straw. The second column lists the concentrations of iron atoms measured by ICP-AES. These concentrations are different from the concentrations of nanoparticles (which is Fe_3O_4) but can be converted. The third column $\Delta\chi$ lists the quantified susceptibility values from CISSCO. The fourth column lists the percentage error of each susceptibility measurement derived from the CISSCO method.

As the CISSCO method currently only uses phase distributions outside each straw for the susceptibility quantification, in order to check consistency of our results, we also checked whether the phase value inside each straw agree with that calculated from the quantified susceptibility. From both orientations (parallel and perpendicular to the main field), we have discovered that phase values inside many straws were not well predicted by the quantified susceptibility values. Closer examines revealed that phase values inside different straws in Fig. 1 appeared to be somewhat proportional to the quantified susceptibility values. Similar situation was also observed from the parallel orientation. However, phase values inside straws from the parallel case were much less than phase values from the perpendicular case for those nanoparticle solutions. This is completely opposite to theoretical predictions. We had suspected materials inside straws other than nanoparticles, as we recalled that those nanoparticles were mixed with sodium hydroxide (NaOH) for coating purposes during their manufacture processes. However, when we imaged the NaOH solution inside a straw, we did not observe any substantial phase value inside the straw, when the straw was perpendicular to the main field. Thus, we have carefully examined this issue by simulating the effect due to the 32 x 32 high pass filter applied to the nanoparticle concentrations, locations of straws, and phantom sizes. In addition, we have examined the outcomes due to different background phase removal methods. We will present those results later in this report.

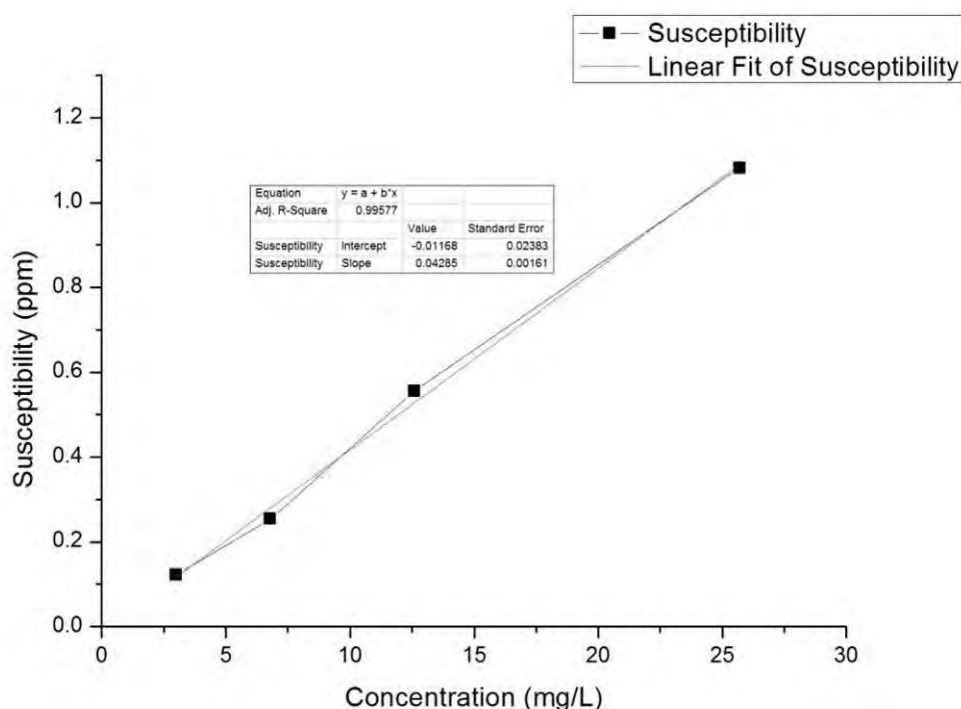


Figure 3: Quantified susceptibility values from MRI versus concentrations of nanoparticles from ICP-AES.

5) Susceptibility quantification of gadolinium Magnevist MRI contrast agent

Similar to nanoparticle experiments, we applied the same procedures to gadolinium. Examples are shown in Figs. 4 and 5 and results are listed in Table 2 and plotted in Fig. 6. We again see a good linear fit between the susceptibility and concentration measurements. We also note that the susceptibility and concentration is convertible, as the atomic weight of gadolinium is 157.25 g (per mole) and the molar susceptibility for gadolinium is 0.339 ppm/mM provided by Weisskoff and Kihne [1992]. With the conversion factor calculated from these numbers, our susceptibility measurements agree very well with the concentrations measured from ICP-AES listed in Table 2.

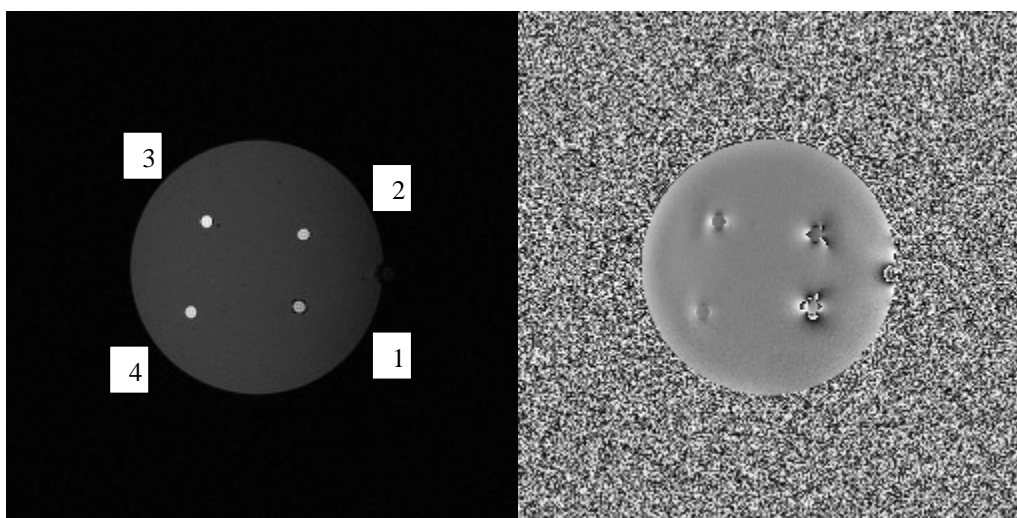


Figure 4: Coronal magnitude (left panel) and filtered phase (right panel) images of gadolinium with concentrations #1, #2, #3, and #4. This set of image was acquired from echo time 15.24 ms and slice No. 33.

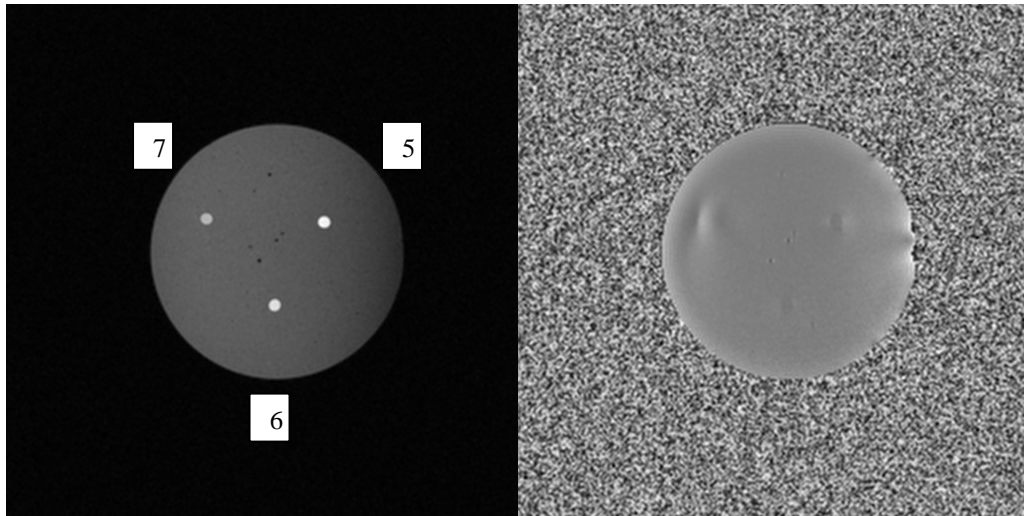


Figure 5: Coronal magnitude (left panel) and filtered phase (right panel) images of gadolinium with concentration #5, #6, and #7. This set of image was acquired from echo time 15.24 ms and slice No. 33.

No.	Conc (mg/L)	$\Delta\chi$ (ppm)	$\delta(\Delta\chi)/\Delta\chi$ (%)
1	855.03	1.78	3.6
2	467.59	0.95	3.7
3	213.62	0.52	4.6
4	109.03	0.28	8.0

Table 2: Quantified results from ICP-AES and MRI for different concentrations of gadolinium MRI contrast agent. The first column labels each straw. The second column lists the concentrations of gadolinium atoms measured by ICP-AES. The third column $\Delta\chi$ lists the quantified susceptibility values from CISSCO. The fourth column lists the percentage error of each susceptibility measured from the CISSCO method.

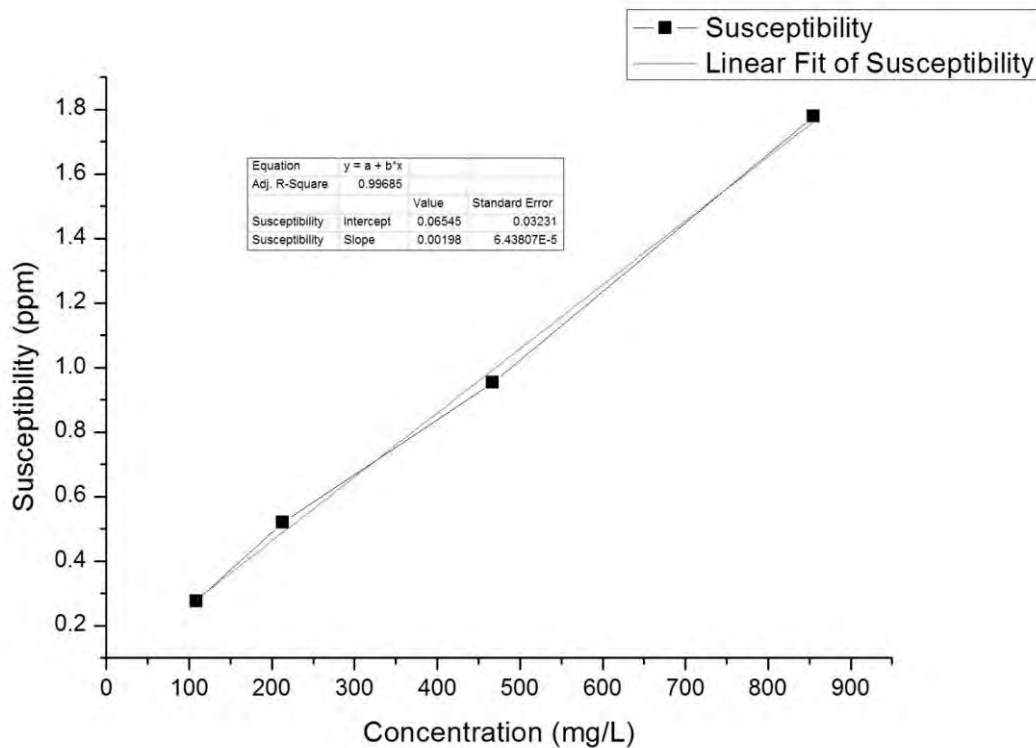


Figure 6: Quantified susceptibility values from MRI versus concentrations of Gd-DTPA from ICP-AES.

6) Measurements of relaxation rates for nanoparticle and gadolinium solutions

The relaxation rates $R2^*$ and $R2$ are calculated from the 11-echo SWI and the 14-echo spin echo images, respectively, with an in-house software SPIN. From the statistical point of view, it is better to use at least 6 echoes for $R2^*$ or $R2$ estimations. However, if $R2$ or $R2^*$ is large, then it is also important to check whether the signal-to-noise ratio (SNR) is at least 3:1 in images. As $R2$ or $R2^*$ quantifications rely on exponential fit to the MR signals, it does not make sense to include images with very low SNRs for analyses. With the concentrations or susceptibility values we have considered, we may use less than 6 echoes to quantify $R2$ or $R2^*$. In the phantoms shown in Figs. 1 and 3, we only use 1 pixel inside each straw for $R2$ or $R2^*$ calculations. This is to avoid partial volume or Gibbs ringing effect. In addition, with the given SNR in images and the number of pixels for measurements, we will also be able to estimate the uncertainty for each measurement through error propagations.

In addition to measurements, we are also interested in theoretical predictions of $R2$ and $R2^*$. Gillis et al. [1999] and Koenig and Kellar [1995] have several theoretical formulas for the estimations of $R2$ values based on susceptibility values or concentrations. However, we have found that none of the formulas can properly predict the $R2$ values measured from our nanoparticle or gadolinium phantoms. In fact, all the theoretical values are at least two orders of magnitude away from the measured $R2$ values. Thus, we are not including those confounding results in this report.

On the other hand, by neglecting the $R2$ value of water or gel, we may be able to estimate theoretical $R2^*_{\text{theory}}$ value given by [Yablonskiy and Haacke, 1994; Shen et al., 2008]

$$R2^*_{\text{theory}} = 0.4 \gamma \Delta\chi B_0 \quad (1)$$

where γ is the gyromagnetic ratio ($2\pi \cdot 42.58$ MHz/T), $\Delta\chi$ is the quantified susceptibility of the composite sample or material (in which the volume fraction has been included), and B_0 is the main field strength (2.89 T). We tested Eq. 1 with nanoparticles mixed in gel in Shen et al. [2008]. With those straws in Figs. 1 and 3, we have quantified their $R2$ and $R2^*$ values and list them in Tables 3 and 4.

	Conc (mg/L)	$R2$ (Hz)	$R2^*$ (Hz)	$R2^*_{\text{theory}}$ (Hz)
Straw 1	25.70	28.1 ± 2	128.2 ± 11	334.02
Straw 2	12.59	22.2 ± 1.5	109.3 ± 9	173.19
Straw 3	6.80	14.7 ± 2	78.7 ± 8	77.32
Straw 4	3	11.7 ± 2.5	44.8 ± 7	37.11

Table 3: Quantified results from ICP-AES and MRI relaxation rates with uncertainties for different concentrations of nanoparticles diluted in distilled water. The first column labels each straw. The second column lists the concentrations of iron atoms measured by ICP-AES. The third column lists measured $R2$ values from the spin echo sequence. The fourth column lists $R2^*$ values measured from SWI. These measurements are from the first phantom shown in Fig. 1. Only the first 6 echoes were chosen for $R2$ and $R2^*$ quantifications. The fifth column lists the theoretical $R2^*$ values calculated from Eq. 1.

	Conc (mg/L)	$R2$ (Hz)	$R2^*$ (Hz)	$R2_{\text{theory}}$ (Hz)
Straw 1	855.03	30.3 ± 0.2	31 ± 2	23.6
Straw 2	467.59	15.4 ± 0.1	16 ± 2	12.6
Straw 3	213.62	5.7 ± 0.7	5.8 ± 2	6.9
Straw 4	109.03	3.0 ± 0.1	3.2 ± 2	3.7

Table 4: Quantified results from ICP-AES and MRI relaxation rates with uncertainties for different concentrations of gadolinium diluted in distilled water. The second column lists the concentrations of iron atoms measured by ICP-AES. The fifth column lists the theoretical $R2$ values estimated from the molar susceptibility of gadolinium, quantified susceptibility values (from Table 2), and relaxivity 4.5 /mM/sec from Haacke et al., Magnetic Resonance Imaging, Ch. 22 [1999]. Other columns have been described in Table 3. Again, only the first 6 echoes were chosen to quantify $R2$ and $R2^*$ along with uncertainties for all 4 straws.

We also plot the results as a function of susceptibility values (which are linearly proportional to concentrations) and show them in Figs. 7 and 8. Clearly shown in both Table 3 and Fig. 7, $R2^*_{\text{theory}}$ only agrees with quantified $R2^*$ of low concentration nanoparticle solutions in straws #3 and #4. Between the listed $R2^*_{\text{theory}}$ values in Table 3 and measured $R2^*$ values in Table 4, it is also clear that Eq. 1 cannot predict $R2^*$ values from gadolinium solutions. The theoretical $R2$ values in Table 4 are based on the empirically measured relaxivity 4.5 /mM/sec for gadolinium from Haacke et al., Magnetic Resonance Imaging, Ch. 22 [1999]. Given the estimated uncertainties of $R2$ values, those theoretical $R2$ values do not quite agree with measured values.

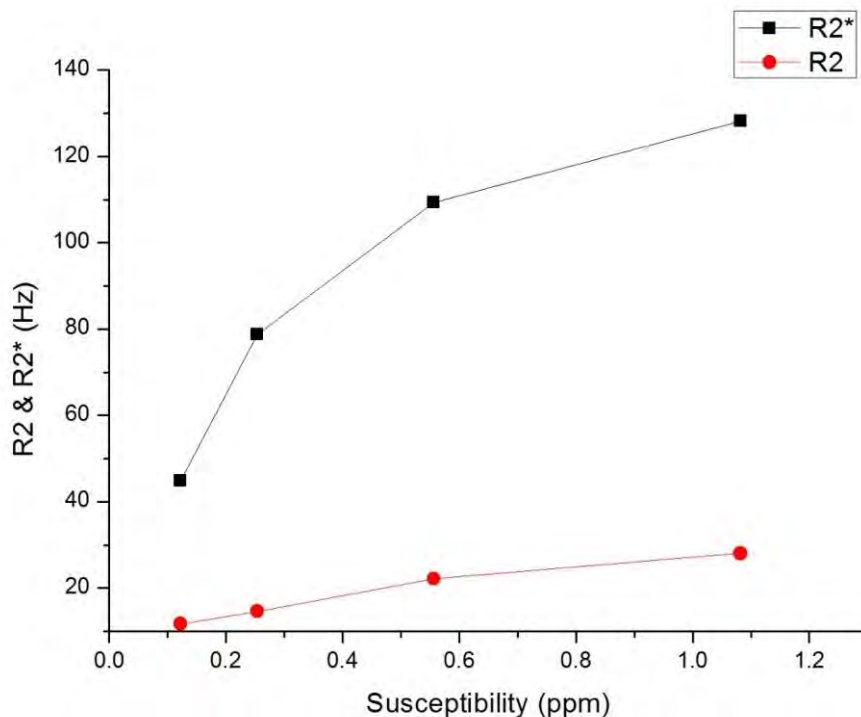


Figure 7: Quantified R_2 and R_2^* values versus quantified susceptibilities of nanoparticles. The relation between the susceptibility and $R2^*$ measurements is not linear.

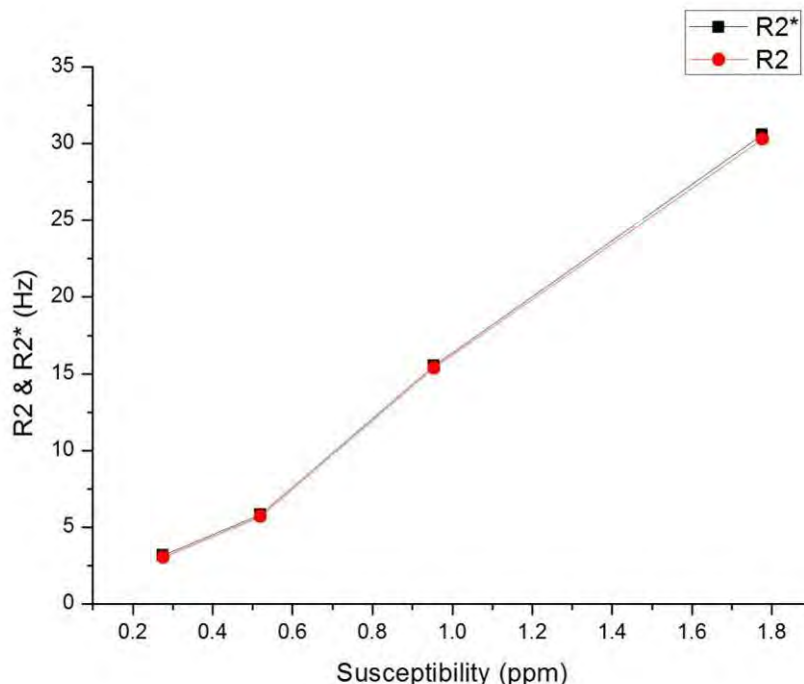


Figure 8: Quantified R_2 and R_2^* values versus quantified susceptibilities of Gd-DTPA.

Nonetheless, Fig. 8 shows linear relations between $R2/R2^*$ and susceptibility values (and thus concentrations) of gadolinium solutions. All these results prompted us to further investigate the $R2$ and $R2^*$ quantifications. We have prepared a few more phantoms with straws and tubes briefly described below. We have also mixed nanoparticles with gelatin solutions and have made solidified samples.

In the third phantom, we prepared a straw with nanoparticle solution having 27.50 mg/L of iron in water and two plastic tubes of diameter 14 mm with nanoparticles mixed in the gelatin solutions. For tube #1, 30 mg/mL of gelatin solution was prepared and mixed with 27.50 mg/L nanoparticle solution in 1:1 ratio by volume. For tube #2, 50 mg/mL of gelatin solution is prepared and mixed with nanoparticles solution in 1:1 ratio by volume. The concentrations of iron nanoparticles in both tubes were 12.59 mg/L. A total of 16 pixels inside each tube were used for $R2$ and $R2^*$ quantifications. The results are listed in Table 5. We now see the agreement between $R2^*_{\text{theory}}$ and measured $R2^*$ for solidified samples. However, the $R2$ or $R2^*$ values from those solidified samples are statistically significantly higher than those in Table 3 with the same concentration.

	Conc (mg/L)	$R2$ (Hz)	$R2^*$ (Hz)	$R2^*_{\text{theory}}$ (Hz)
Straw 1	25.70	13.6 ± 0.8	112 ± 6	334.02
Tube 1	12.59	34 ± 3	159 ± 9	173.19
Tube 2	12.59	34 ± 3	172 ± 8	173.19

Table 5: Relaxation rates of nanoparticles diluted with water in a straw and mixed with gelatin in tubes. Nanoparticles mixed with gel were solidified in tubes. These results were from the third phantom. For $R2$ and $R2^*$ quantifications, the first 6 echoes were used for the straw but only 3 echoes were used for both tubes, due to the insufficient SNR after the third echo. The meaning of each column was given in Table 3.

In the fourth phantom, the three straws had the same mixtures as in the straw and the two tubes in the third phantom, respectively. The results are listed in Table 6. Again, $R2^*_{\text{theory}}$ and measured $R2^*$ values agree for solidified samples in straws #2 and #3. This indicates that measurements of relaxation rates do not seem to depend on geometry. However, there may be a minor concern about different $R2^*$ values between Table 5 and Table 6 from the highest concentration, but we cannot make a firm conclusion as two standard deviations of estimated uncertainties still overlap with each other. Nonetheless, the $R2$ values seem to be affected by the gelatin concentrations but this is inconsistent between straws #2 and #3 shown in Table 6. In addition, we do not place the highest nanoparticle concentration in gelatin form, as the theoretical $R2^*$ value (334 Hz) indicates that we will need echo times between 1 ms and 6 ms with echo spacing of roughly 1 ms. There is no such a practical sequence to use.

	Conc (mg/L)	$R2$ (Hz)	$R2^*$ (Hz)	$R2^*_{\text{theory}}$ (Hz)
Straw 1	25.70	18 ± 1.2	132 ± 6.5	334.02
Straw 2	12.59	39 ± 5.8	159 ± 13	173.19
Straw 3	12.59	58.8 ± 6.6	177 ± 14	173.19

Table 6: Similar to Table 5, relaxation rates of nanoparticles in water or in solidified gelatin are shown. For all 3 straws, the first 6 echoes are chosen to quantify $R2^*$ and their corresponding uncertainties. However, for $R2$ quantification, only the first 3 echoes are used for straws #2 and #3 but the first 6 echoes are used for straw 1.

We constructed the fifth phantom with similar containers used in the third phantom. We placed 855.03 mg/L of gadolinium diluted in water in a straw and mixed gadolinium with the 1:1 ratio by volume with 30 mg/mL and 50 mg/mL of gelatin solutions, respectively, in tubes #1 and #2 with diameters of 11 mm. The concentrations of gadolinium in both tubes were 469.59 mg/L. Table 7 lists the results. The results in the straw are consistent with the results shown in Table 4. However, the results from tubes with solidified gel indicate higher $R2$ or $R2^*$ values as their counterparts in Table 4. As in theory, relaxation rates are inversely proportional to the diffusion constant, it is expected that the relaxation rates measured from solidified samples (whose diffusion constant is lower) are higher than those measured from liquid samples with the same concentrations (whose diffusion constants would be higher).

	Conc (mg/L)	R2 (Hz)	R2* (Hz)
Straw 1	855.03	29.5 ± 0.2	31.3 ± 1.6
Tube 1	467.59	19.8 ± 0.04	21.4 ± 0.5
Tube 2	467.59	18.5 ± 0.03	19.9 ± 0.4

Table 7: Relaxation rates of gadolinium diluted with water in a straw and mixed with gelatin in tubes. Gadolinium mixed with gel were solidified in tubes. These results were from the fifth phantom. For R2 and R2* quantifications, the first 6 echoes were used for analyses.

We placed the same solutions from the straw and tube #1 used in the fifth phantom into the straws #1 and #2 in the sixth phantom, respectively. We also placed the same solution in straw #2 in a tube for the sixth phantom. The results are shown in Table 8 and they are consistent with results shown in Table 7. We further rotated and imaged the sixth phantom and quantified the relaxation rates inside the straws and tube again. The results listed in Table 9 are consistent with those shown in Table 8.

	Conc (mg/L)	R2 (Hz)	R2* (Hz)
Straw 1	855.03	29 ± 0.2	31.4 ± 1.4
Straw 2	467.59	20 ± 0.1	22 ± 1.3
Tube 1	467.59	20 ± 0.2	21 ± 1.4

Table 8: Relaxation rates of gadolinium solutions from the sixth phantom. For quantification of relaxation rates, the first 6 echoes have been used.

	Conc (mg/L)	R2 (Hz)	R2* (Hz)
Straw 1	855.03	29.3 ± 0.3	30 ± 1.5
Straw 2	467.59	20 ± 0.2	21.3 ± 1.8
Tube 1	467.59	19.2 ± 0.1	21 ± 1.7

Table 9: Quantification of relaxation rates from the sixth phantom with a 90° rotation such that before and after the rotation, straws and the tube are always perpendicular to the main field.

From the above results above, it is apparent that relaxation rates of either nanoparticle or gelatin solutions are higher in solidified gel than in water. However, the ratios of increased relaxation rates are not the same for nanoparticle and gadolinium samples. This means that a simple diffusion constant is not the only factor to affect the changes of relaxation rates from liquid samples to solidified samples. In addition, for nanoparticles, R2 and R2* are very different but R2 and R2* are about the same for gadolinium samples. Furthermore, the R2* theory can only predict the values of nanoparticles in solidified gels. R2 theory cannot predict any measured R2 values. However, when the gadolinium samples have the same concentration as that of the second straw listed in Table 2, regardless whether the samples were mixed with water or gelatin, the susceptibility measurements from CISSCO agreed very well with the value (within the uncertainty) shown in Table 2. Similarly, susceptibility values of nanoparticle samples are basically the same for the same concentration, independent of the material used for sample preparations. Some results are listed in Table 10. All these findings are important knowledge to the MRI community.

	Conc (mg/L)	$\Delta\chi$ (ppm)
Straw 1	25.70	1.28
Straw 2	12.59	0.66
Straw 3	12.59	0.68

Table 10: Quantified susceptibility values from the fourth phantom, Table 6, at TE = 8.07 ms, with the use of the high pass filter to remove the background phase. As the susceptibility measured from the first straw (containing nanoparticles in distilled water) is higher than the susceptibility of the first straw shown in Table 1, this indicates that we should scale the quantified susceptibility values of straws #2 and #3 in this table before we compare these results to the measured susceptibility of straw #2 in Table 1. This is because lower

concentrations were always diluted from the highest concentration in a phantom. After this scaling, the quantified susceptibility values of straws #2 and #3 in this table agree very well with the susceptibility of the second straw in Table 1.

7) Four methods for removing the background phase

As mentioned above, the susceptibility values quantified from our CISSCO method did not fully agree with results derived from phase values inside each straw. The question was whether the disagreements were due to post processing techniques or physical phenomena such as susceptibility tensor. We first examined the images of the phantom (e.g., Fig. 4) containing 4 straws filled with different concentrations of Gd-DTPA in distilled water. The nanoparticle samples contained NaOH which may further complicated the susceptibility quantification and thus would be examined later. We began our investigations with the use of the 32 x 32 high-pass filter and then other background removal techniques including SHARP [Schweser et al., 2011], quadratic fitting (i.e., second order polynomial fit to the background phase), and our proposed algorithm. These were a total of 4 methods. It is necessary to remove the unwanted background phase before any susceptibility quantification method can be applied to images. In order to use SHARP and quadratic fitting method, we had to unwrap phase in phase images. After applying any of these background removal techniques, we directly measured the averaged phase values inside each straw (which contained a solution at a given concentration) from different echo times. Different background removal methods also allow us re-quantify the susceptibility value using CISSCO again. Then we compared these results for consistency checks.

a) High-pass filter and simulations of its effect

The high-pass filter has been widely used due to its fast post-processing capability. To examine the high-pass filter effect on susceptibility quantification and phase measurements, we have conducted various simulations. In those simulations, we set up an initial 4096^2 matrix and properly generate a straw with a radius of 3 pixels centered at a final matrix of 256×256 . We either simulate the actual diameter (125 pixels) of the phantom or fill the entire matrix space by the gel phantom. The quantified magnetic moments from former and latter cases are labeled by p'' and p' , respectively, In Fig. 9. We assign a series of magnetic moments p to straws and generate phase images with straws perpendicular and parallel to the main field. In both perpendicular and parallel orientations, we apply a 32 x 32 high-pass filter to those simulated images. For the perpendicular orientation, we quantify each magnetic moment value p by CISSCO. The results are shown in Fig. 9 and are compared to the originally assigned p values.

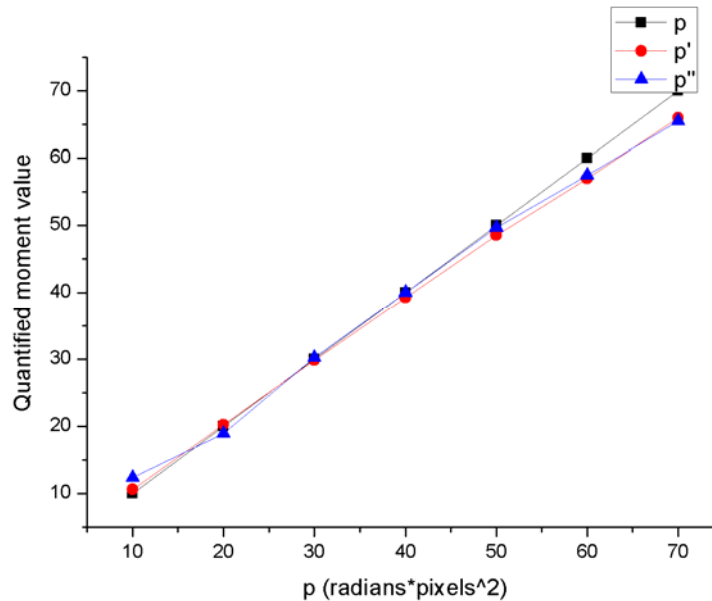


Figure 9: Comparisons between magnetic moment values before and after the high-pass filter. p' denotes the results with the entire matrix space filled by the gel phantom and p'' denotes the results with a sizable gel phantom. p indicates the input value we assigned in each simulation.

Figure 9 indicates that the high-pass filter affects nonlinearly to the magnetic moment quantification. In particular, the quantified magnetic moments in general are smaller than the actual values, except for the case when $p = 10$ radians·pixel². The error induced by the high-pass filter effect is within 7% in the range of p shown in Fig. 9.

To further study the background phase effect in the gel phantom, we have also added a constant background phase of 2 radians inside the gel phantom. The simulated phase images for $p = 10, 40$, and 70 radians·pixel² are shown in Fig. 10. We apply the high-pass filter and quantify the magnetic moment with CISSCO. These results are almost the same as those obtained from zero background phase, labeled by p'' in Fig. 9.

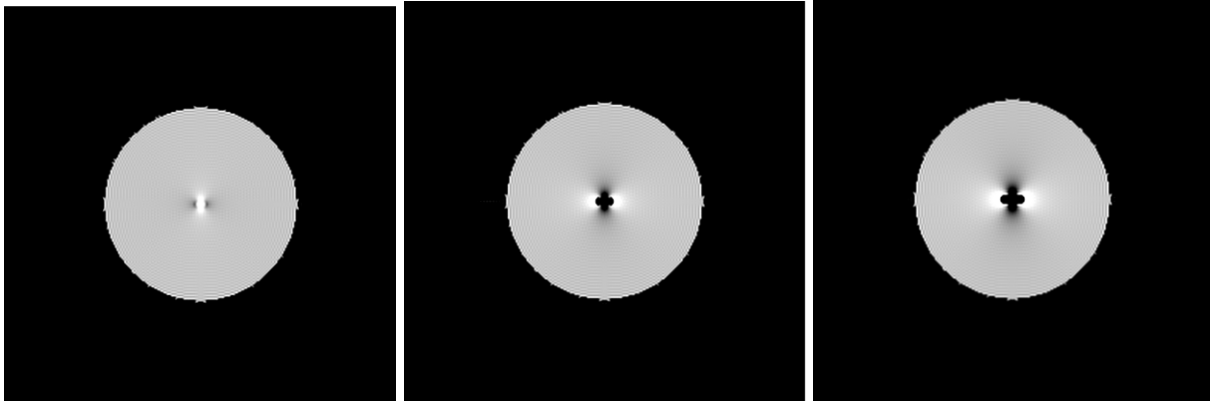


Figure 10: Simulated phase images with a constant background phase of 2 radians inside the gel phantom for $p = 10, 40$, and 70 radians·pixel². A straw is simulated at the center of the phantom.

In addition to the quantification of magnetic moment, we have also examined the high-pass filter effect on phase values inside straws. From simulated phase images in both the perpendicular and parallel orientations, we compare the input phase values with those after the application of the high-pass filter, either with a sizable phantom size or with the entire field-of view (FOV) filled by the phantom. Results are shown in Fig. 11 (perpendicular orientation) and Fig. 12 (parallel orientation).

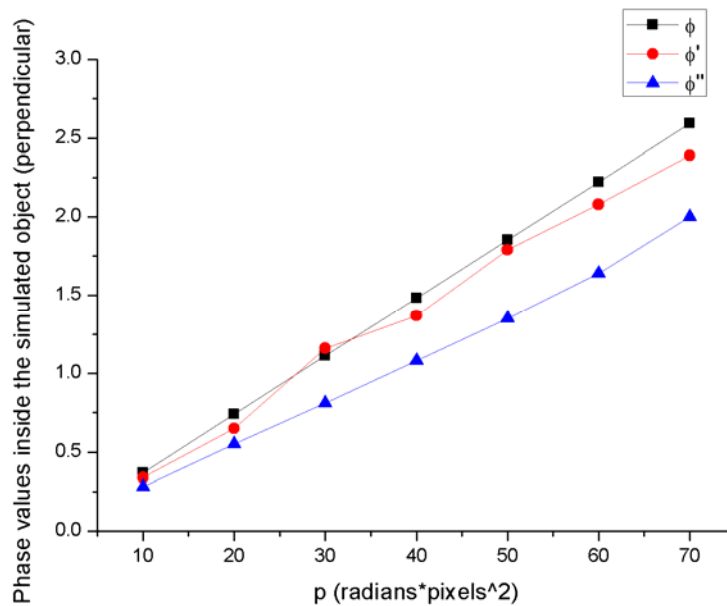


Figure 11: Comparisons between phase values inside straws before and after the high-pass filter in the perpendicular orientations. ϕ' denotes the results with the entire matrix space filled by the gel phantom and ϕ'' denotes the results with a sizable gel phantom. ϕ indicates the input value calculated from the given p value in each simulation.

Figures 11 and 12 show that the high-pass filter reduces the phase value inside each straw. This is expected. However, they show that the size of the gel phantom has to be included in simulations when the high-pass filter is applied. Otherwise we will observe a large difference (or error) in phase measurements for the perpendicular orientation (see Fig. 11). *This is a big surprise to us.* On the other hand, when we use CISSCO to quantify the magnetic moment with the application of the high-pass filter, as shown in Fig. 9, the size of the phantom is not necessary to be included in simulations. Although the high-pass filter has also affected the phase distributions outside each straw, these results indicate that our CISSCO method is quite robust for the quantification of the magnetic moment, which utilizes the phase distributions outside each straw.

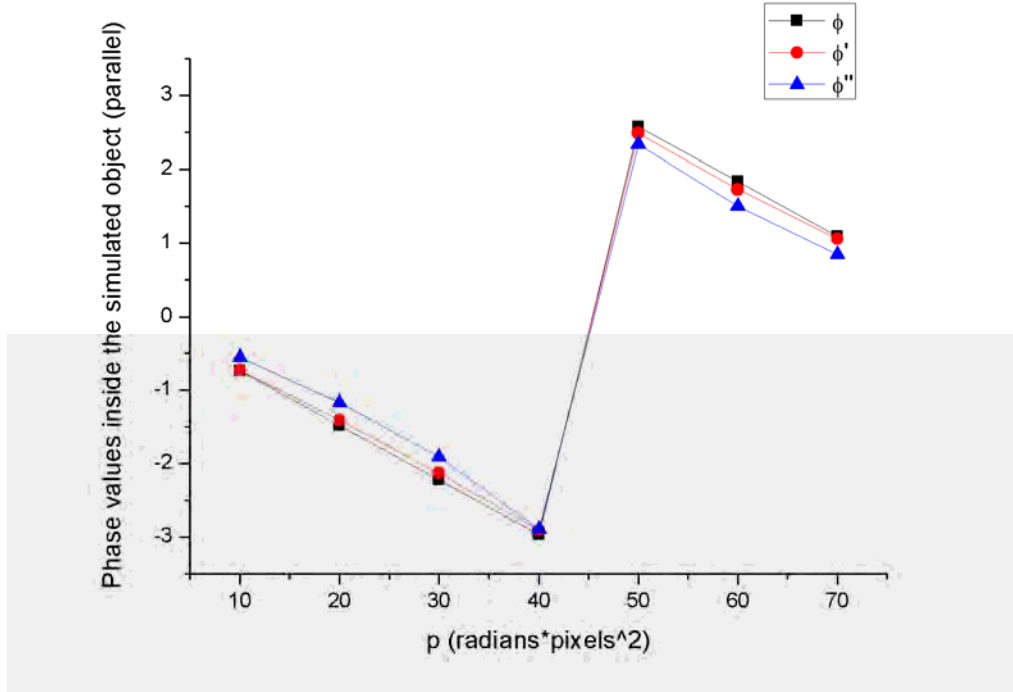


Figure 12: Comparisons between phase values inside straws before and after the high-pass filter in the parallel orientation. ϕ' denotes the results with the entire matrix space filled by the gel phantom and ϕ'' denotes the results with a sizable gel phantom. ϕ indicates the input value calculated from the given p value in each simulation.

As simulated phase values ϕ' and ϕ'' do not deviate much from their corresponding actual phase values in Fig. 12 (but it is not the case in Fig. 11), these suggest that the high-pass filter affects more on areas around straws where induced phase distributions are stronger for the perpendicular orientation. Effectively, those areas may be treated as part of a straw by the high-pass filter. As we know that the high-pass filter affects more on larger objects, non-uniform deviations between ϕ' and ϕ'' shown in Figs. 11 and 12 may be explained by this reason.

When we compare high-pass filtered phase values inside straws from actual phantom images with ϕ'' in Figs. 11 and 12, only phase values from the first two echoes for the perpendicular orientation agree well with predicted ϕ'' . Closer investigations reveal that the leftover background phase in images after the high-pass filter is not close to zero for images from longer echoes or the parallel orientation. This prompts us to consider other background phase removal methods.

Our high-pass filter results based on CISSCO were quantified from TE = 8.07 ms, 10.46 ms, 12.85 ms, and 17.63 ms for the 1st, 2nd, 3rd, and 4th straw, respectively. These echo times were chosen in order to optimize the application of the high-pass filter for relatively accurate quantification. The results are given in Table 11 below and they can be considered as reference values. However, for phase measurements inside straws listed in Table 12, we do not treat those values as references. Figure 11 demonstrates the obvious reason.

b) SHARP

SHARP is a state-of-art tool for removing the background phase. As this is a method developed by Schweser et al., [2011] we have re-built the algorithm. For SHARP, we could take the images from the longest echo time

at TE = 29.58 ms and unwrap the phase in images with the prelude algorithm in FSL. With the unwrapped phase images, we utilized SHARP in both perpendicular and parallel orientation.

In the perpendicular orientation, we quantified the effective magnetic moment and susceptibility for all 4 straws and compared them with the ICP-AES measurements, results from the high-pass filter, and results from our own algorithm (described below with choices of echo times). Susceptibility or phase values of ICP-AES were calculated from their measured concentrations. The results are given in Table 11. Both SHARP and our own algorithm were performed at the echo time of 29.58 ms. The echo times used for the high-pass (HP) filter and for different straws were given above.

Table 11 shows that different methods led to similar results. For comparisons, we performed SHARP with two different radii, 8 and 18 pixels, labeled by SHARP-8 and SHARP-18, respectively. Between these two choices in SHARP, the results of SHARP-18 gave closer values to the susceptibility values derived from ICP-AES measurements. The uncertainty of each measurement from CISSCO is no more than 5% and thus is not listed. The uncertainty of each ICP-AES measurement is also small and has been mentioned above. The accuracy of our proposed algorithm depends on the accuracy of the results from the high-pass filter used at shorter echo times. Different methods agreed better at higher concentrations. We will continue to investigate those slight differences between SHARP and other methods.

Straw	#1	#2	#3	#4
ICP-AES	1.84	1.01	0.46	0.24
HP filter	1.78	0.95	0.52	0.28
SHARP-8	1.75	0.90	0.47	0.22
SHARP-18	1.82	0.92	0.47	0.25
Proposed algorithm	1.74	0.94	0.55	0.30

Table 11: Susceptibility quantifications (in ppm) of different methods for background phase removal from the perpendicular orientation. Each straw is labeled in the first row.

For phase values inside straws at the perpendicular orientation, the application of SHARP leads to consistent results between measured phase values of gadolinium solutions and quantified susceptibility values using CISSCO. However, some differences remain for nanoparticle solutions.

To further examine the consistency among our quantified results, we also applied SHARP to parallel orientation and measured the phase values inside each straw from four different echo times. The results from TE = 8.07 ms are listed in Table 12. Phase values from ICP-AES were calculated from measured concentrations. As the SNR was high in each image, the uncertainty of each average phase value listed in Table 12 is small and thus neglected.

Straw	#1	#2	#3	#4
ICP-AES	-2.45	2.10	0.96	0.50
HP filter	-1.62	1.57	0.78	0.43
SHARP-8	-2.15	2.04	1.10	0.58
Quadratic fitting	-2.22	2.05	1.06	0.58

Table 12: Phase measurements inside straws in units of radian from different methods at the parallel orientation at TE = 8.07 ms. Again, each straw is labeled in the first row.

Table 12 shows that the high-pass filter can significantly alter the phase values when the background phase distributions are strong. SHARP and the quadratic fitting method give more reasonable results than those from the high-pass filter. In this study, SHARP-8 and SHARP-18 give almost the same outcomes so we only show results from one of them. Comparing results between Table 11 and Table 12 and using ICP-AES results as references, it seems that results from our proposed algorithm are the most consistent with results from ICP-AES. For example, the susceptibility values from our proposed algorithm are less than values from ICP-AES for straws #1 and #2 in Table 11 but more than values from ICP-AES for straws #3 and #4. These trends agree with results in Table 12 from SHARP-8 and quadratic fitting method, if we can believe that the quadratic fitting

method has also properly removed the background phase. However, following the same logic, results from SHARP are not self-consistent between Table 11 and Table 12.

c) Quadratic fitting

From original phase images of the parallel orientation, phase aliasing (wrapping) can occur along the radial direction. This is due to the background phase from the gel phantom itself. As the straws parallel to the field do not produce magnetic fields outside the straws, we fit the phase in the agar gel part without straws to a quadratic equation. Again, we first unwrap phase aliasing in original phase images, and then apply binary masks to exclude the straws and the noise region outside the agar gel phantom. Then, from the masked phase images we are able to perform the quadratic fitting method and remove the background phase with a complex division procedure. The resulting image is shown in Fig. 13c. We then measure the phase inside each straw at different echo times. Results scaled by echo times are consistent within 10% differences. Results from TE = 8.07 ms are listed in Table 12. For the perpendicular orientation, as straws induce phase distributions outside, it would be less accurate to apply the quadratic fitting method.

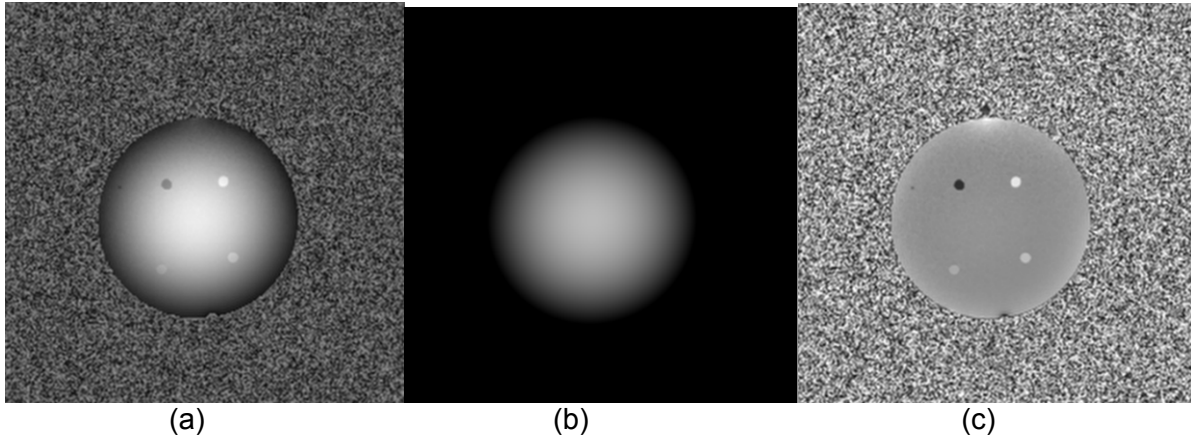


Figure 13: (a) Unwrapped phase from the original image. (b) Background phase from the quadratic fitting method. (c) Resulting phase image after removing the background phase (b) from (a).

d) Our proposed algorithm

A simple algorithm described in the proposal was also applied in the perpendicular orientation, in order to remove the background phase for susceptibility quantification. The procedures are described below:

1. We applied the 32 x 32 high-pass filter on phase images from a shorter echo time of the 11-echo SWI, for example, TE = 15.24 ms, and then quantified magnetic moment for each straw;
2. From the quantified magnetic moment, we simulated phase distributions inside and around each straw;
3. We applied complex division to remove the simulated phase pattern around each straw (step 2) from the filtered phase in step 1. This was to obtain phase images containing only “background phase”;
4. We multiplied the “background” phase pattern by an integer, e.g. 2, to obtain a “background” phase at TE = 30.48 ms ($2 \times 15.24 = 30.48$);
5. We complex divided the “background” phase (step 4) from the phase image at a longer echo time, e.g. TE = 29.58 ms, and then applied an 8 x 8 high-pass filter.
6. We obtained a phase image at TE = 29.58 ms, with most of the background phase removed but phase induced by the straws remained. We quantified the magnetic moment for each straw, calculated the susceptibility, and compared it with results from other methods. The results are also listed in Table 11.

The above steps show a simplified version of our algorithm. Some errors can exist, as in general the simulated phase distributions were less than the actual values due to the application of the 32 x 32 high-pass filter.

Additional background phase in images unremoved by the high-pass filter can significantly reduce the quantified magnetic moment of each straw. However, increasing the high-pass filter size will also reduce the quantified magnetic moment. This is the reason why this algorithm needs to be applied to a shorter echo time first and then to a long echo time from a multiple echo gradient echo sequence. Results in Table 11 for straws #3 and #4 were from TE = 15.24 ms in step 1, while for straw #2, it was from TE = 10.46 ms with a multiplication of 3 (rather than 2) in step 4. For straw #1, TE = 8.06 ms should be used in step 1 and then a multiplication factor of 3 or 4 can be used. However, in this case the uncertainty will be amplified due to the multiplication factor.

8) Susceptibility quantification of calcium

We purchased CaCl_2 in powder forms from sigma.com and prepared them to be 4 different solutions. Their concentrations and quantified susceptibility values using the high-pass filter and CISSCO are listed in Table 13. In order to achieve desired susceptibility values, we have to prepare very high concentrations of calcium. The quantified susceptibility values (except from the first straw) are self-consistent among echo times, with differences within 5% (considered as uncertainty). The quantified susceptibility values from the first straw vary by roughly 10%, due to the high-pass filter effect on large magnetic moment values. Note that the negative signs of susceptibility values indicate that calcium solutions are diamagnetic to water.

Straw No.	Concentration (mg/mL)	TE (ms)	$\Delta\chi$ (ppm)
1	503.9	8.07	-1.79
		10.46	-1.60
		12.85	-1.47
2	252.0	8.07	-1.13
		10.46	-1.11
		12.85	-1.06
3	126.0	8.07	-0.63
		10.46	-0.60
		12.85	-0.60
4	63.0	8.07	-0.35
		10.46	-0.33
		12.85	-0.32

Table 13: Susceptibility quantifications of CaCl_2 solutions using the high-pass filter and CISSCO. The first column lists the straw number. The second column lists the concentration inside each straw. The third column lists the echo time of the images that we quantified the susceptibility. The fourth column lists the measured susceptibility corresponding to each echo time.

To compare results with those from the high-pass filter, we have also applied SHARP to remove the background phase and results are listed in Table 14. The results shown in Table 14 are consistent for each straw at different echo times. The averaged susceptibility values are calculated from the three shorter echo times, as at TE = 29.58 ms, the quantified susceptibility values are normally smaller due to the use of SHARP. We will investigate the reason in the future. The quantified susceptibility values from both high-pass filter and SHARP are plotted in Fig. 14. The susceptibility values from high-pass filter plotted in Fig. 14 are chosen from TE = 8.07 ms, which has the minimal effect among the three echo times listed in Table 13.

Straw No.	$\Delta\chi$ (TE=8.07ms)	$\Delta\chi$ (TE=10.46ms)	$\Delta\chi$ (TE=12.85ms)	$\Delta\chi$ (TE=29.58ms)	$\Delta\chi$ (avg.)
1	-1.93	-1.90	-1.92	-1.91	-1.92
2	-1.16	-1.15	-1.16	-1.13	-1.16
3	-0.63	-0.62	-0.61	-0.61	-0.62
4	-0.35	-0.34	-0.34	-0.32	-0.34

Table 14: Susceptibility quantifications of calcium solutions using SHARP and CISSCO. The first column lists the straw number. The second to the fifth column list the susceptibility quantified at the given echo time. The last column lists the averaged susceptibility values from the three shorter echo times.

We have further checked the phase values inside straws for the calcium solutions, against the phase values calculated from quantified susceptibility values listed in Tables 13 and 14. Table 15 shows that the phase values after using SHARP to remove the background phase are closer to and thus more consistent with phase values calculated from quantified susceptibilities. For easier comparisons, some phase values are unwrapped. As the inverse of SNR is one standard deviation of the noise in phase images, the last column of Table 15 allows us to see whether the differences between measured and expected phase values are due to the presence of noise. It is clear that the differences are not only due to noise but also due to possibly the method of SHARP itself. In the human brain model section later, we will show some evaluations of the SHARP method. We will continue to investigate and evaluate the outcome of SHARP.

	Straw	Echo Time (ms)	Perpendicular		Parallel		
			Phase _{theory}	Phase _{actual}	Phase _{theory}	Phase _{actual}	1/SNR
SHARP	1	8.07	2.01	1.59	-4.02	-4.14	0.024
		10.46	2.56	2.03	-5.11	-5.37	0.024
		12.85	3.18	2.48	-6.35	-5.85	0.025
	2	8.07	1.21	0.72	-2.41	-2.41	0.042
		10.46	1.55	1.00	-3.10	-3.01	0.042
		12.85	1.91	1.20	-3.83	-4.02	0.042
	3	8.07	0.66	0.28	-1.32	-1.28	0.025
		10.46	0.83	0.39	-1.66	-1.65	0.024
		12.85	1.01	0.53	-2.03	-2.02	0.025
	4	8.07	0.37	0.06	-0.73	-0.65	0.040
		10.46	0.46	0.15	-0.91	-0.84	0.040
		12.85	0.56	0.29	-1.11	-1.00	0.042
High-Pass Filter	1	8.07	1.86	1.14	2.55	1.94	0.024
		10.46	2.16	1.33	1.97	0.66	0.024
		12.85	2.43	1.35	1.42	-0.24	0.025
	2	8.07	1.18	0.55	-2.36	-2.24	0.042
		10.46	1.50	0.73	-2.99	N/A	0.042
		12.85	1.75	0.70	2.77	2.37	0.042
	3	8.07	0.66	0.27	-1.31	-0.99	0.025
		10.46	0.81	0.37	-1.63	-1.16	0.024
		12.85	0.99	0.37	-1.98	-1.26	0.025
	4	8.07	0.36	0.05	-0.73	-0.5	0.040
		10.46	0.45	0.12	-0.90	-0.59	0.040
		12.85	0.53	0.10	-1.07	-0.69	0.042

Table 15: Comparisons between measured and expected phase values inside each straw for calcium solutions at both perpendicular and parallel orientations at three different echo times. The first column lists the method of choice (SHARP or high-pass filter) to remove the background field. The second column lists the straw number. The third column lists the echo time of the images for quantifications. The fourth and sixth column list the expected phase values calculated from quantified susceptibility values listed in Tables 13 and 14. Note that susceptibility values from Tables 13 and 14 are used for calculating phase values based on the use of the high-pass filter or SHARP, respectively. The fifth and seventh column list the measured phase values. The last column lists the noise of one standard deviation in phase images for the parallel orientation. Signal-to-noise ratios were measured for each straw at different echo times. N/A in the table means no phase value was measured due to reasons such as obvious artifacts.

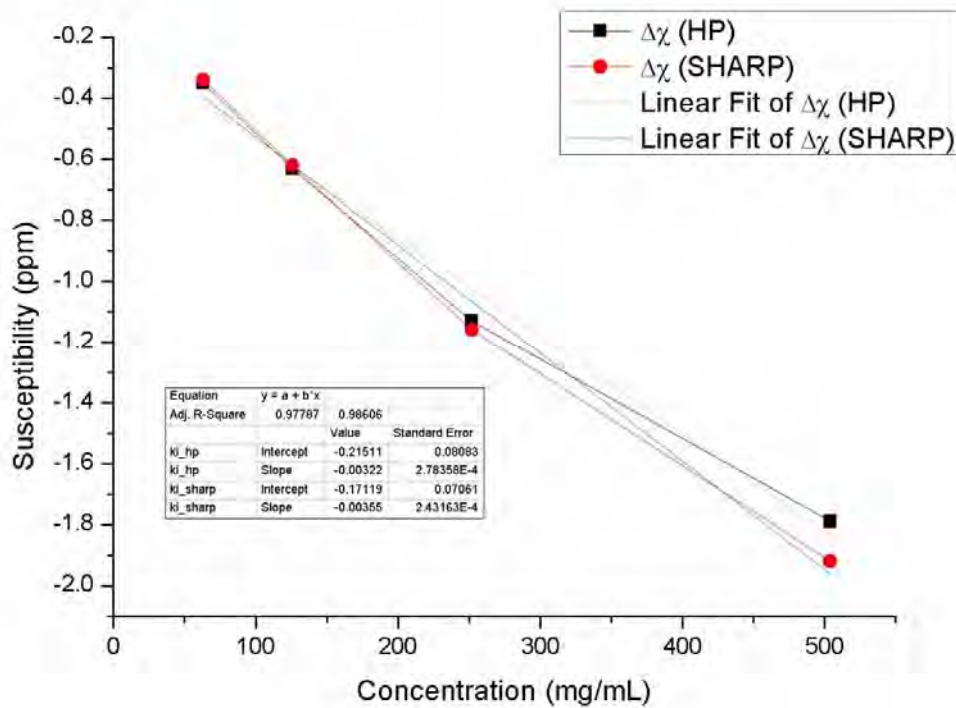


Figure 14: Quantified susceptibility values based on CISSCO with either the use of the high-pass filter or SHARP versus concentrations of CaCl_2 . Linear relations between the susceptibility and concentration are given in the chart. This figure clearly shows that SHARP leads to better results than the high-pass filter. Note that the slopes of the fitted lines are negative as CaCl_2 is diamagnetic to water.

9) Susceptibility quantification of ferritin

Similar to the calcium case, we have quantified the susceptibility of 4 different ferritin concentrations. Table 16 lists the results from the high-pass filter. Again, quantified susceptibility values from different echo times are only consistent at low concentrations. The high-pass filter leads to inconsistent values at high concentrations.

Straw No.	Concentration (mg/mL)	TE (ms)	$\Delta\chi$ (ppm)
1	1.87	8.07	2.25
		10.46	2.08
		12.85	1.97
2	0.93	8.07	1.25
		10.46	1.22
		12.85	1.12
3	0.47	8.07	0.63
		10.46	0.63
		12.85	0.60
4	0.23	8.07	0.32
		10.46	0.33
		12.85	0.32

Table 16: Quantified susceptibility values for ferritin solutions with the use of the high-pass filter. The second column lists the iron concentrations rather than the ferritin concentrations. The meanings of other columns have been explained in Table 13.

To compare quantified susceptibility values from CISSCO, between the uses of the high-pass filter and SHARP to remove the background field, we obtain results from SHARP and show them in Table 17. When ferritin

concentrations are relatively low, we see from Tables 16 and 17 that quantified susceptibility values agree with each other, regardless of whether the high-pass filter or SHARP is applied to original phase images. At a high concentration, SHARP (from Table 17) shows more consistent results than the high-pass filter (from Table 16). As the results shown in Table 17 are very consistent for each straw at the first three echo times, the averaged susceptibility values are calculated only from the three shorter echo times. At TE = 29.58 ms, the quantified susceptibility values are slightly smaller due to the use of SHARP. The quantified susceptibility values from both high-pass filter and SHARP are plotted in Fig. 15. The fit from SHARP shows a good linear relation between susceptibility and sample concentration. The slope of the fit is 1.38 ± 0.01 ppm*ml/mg, which is more than 20% higher than our previous results [Zheng et al., 2013]. This difference is likely due to the use of different ferritin samples and it is for this conjecture we are re-doing experiments on ferritin solutions. In addition, our uncertainty 0.01 ppm*ml/mg is likely underestimated, as error due to each susceptibility measurement from CISSCO and SHARP was not included in the uncertainty estimations. The susceptibility values from high-pass filter plotted in Fig. 15 are again chosen from TE = 8.07 ms, which has the minimal effect among the three echo times listed in Table 16.

Straw No.	$\Delta\chi$ (TE=8.07ms)	$\Delta\chi$ (TE=10.46ms)	$\Delta\chi$ (TE=12.85ms)	$\Delta\chi$ (TE=29.58ms)	$\Delta\chi$ (avg.)
1	2.59	2.59	2.58	2.53	2.59
2	1.30	1.32	1.31	1.30	1.31
3	0.65	0.65	0.63	0.63	0.64
4	0.33	0.33	0.32	0.31	0.33

Table 17: Quantified susceptibilities of ferritin solutions using SHARP and CISSCO. The meaning of each column has been explained in Table 14.

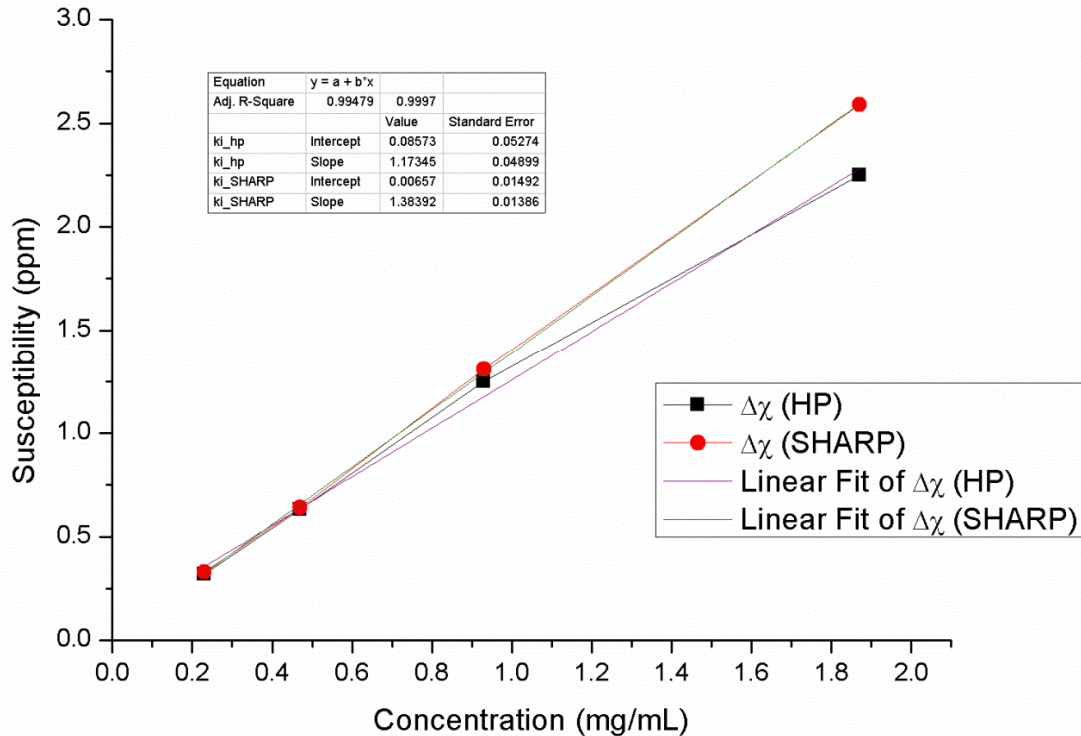


Figure 15: Quantified susceptibility values based on CISSCO with either the use of the high-pass filter or SHARP versus ferritin concentrations. Linear relations between the susceptibility and concentration are given in the chart. This figure clearly shows that SHARP leads to more consistent results than the high-pass filter.

We have again checked the phase values inside straws for the ferritin solutions, against the phase values calculated from quantified susceptibility values listed in Tables 16 and 17. The results are listed in Table 18. For easier comparisons, some phase values have been unwrapped due to the subtle details in phase unwrapping software. We also list the inverse of SNR inside each straw in Table 18 for the parallel orientation,

as $1/\text{SNR}$ is one standard deviation of the noise in phase images. However, in most cases, the measured phase values differ from expected phase values by more than two standard deviations. This suggests that other scientific reasons rather than the Gaussian noise are needed to explain those differences.

	Straw	Echo Time (ms)	Perpendicular		Parallel		
			Phase _{theory}	Phase _{actual}	Phase _{theory}	Phase _{actual}	1/SNR
SHARP	1	8.07	-2.69	-2.27	5.39	5.43	0.020
		10.46	-3.49	-3.11	6.99	7.46	0.021
		12.85	-4.26	-3.77	8.53	8.85	0.024
		29.58	-9.65	-8.44	19.31	20.82	0.050
	2	8.07	-1.35	-1.54	2.70	2.91	0.026
		10.46	-1.77	-1.95	3.55	3.82	0.028
		12.85	-2.17	-2.44	4.33	4.69	0.029
		29.58	-4.97	-5.69	9.94	10.74	0.042
	3	8.07	-0.67	-0.71	1.35	1.48	0.024
		10.46	-0.88	-0.91	1.76	1.96	0.024
		12.85	-1.05	-1.14	2.10	2.38	0.024
		29.58	-2.40	-2.83	4.80	5.55	0.029
	4	8.07	-0.34	-0.33	0.68	0.80	0.017
		10.46	-0.44	-0.43	0.89	1.08	0.017
		12.85	-0.54	-0.55	1.08	1.26	0.017
		29.58	-1.20	-1.37	2.40	2.86	0.019
High-Pass Filter	1	8.07	-2.34	-2.01	-1.60	-0.41	0.020
		10.46	-2.80	-2.54	-0.68	0.99	0.021
		12.85	3.02	N/A	2.23	2.27	0.024
	2	8.07	-1.30	-1.53	2.60	2.98	0.026
		10.46	-1.65	-1.95	-2.99	-2.22	0.028
		12.85	-1.85	-2.47	-2.57	-1.24	0.029
	3	8.07	-0.66	-0.71	1.32	1.41	0.024
		10.46	-0.84	-0.85	1.69	1.80	0.024
		12.85	-0.99	-1.01	1.99	2.08	0.024
	4	8.07	-0.34	-0.43	0.68	0.83	0.017
		10.46	-0.44	-0.55	0.88	0.96	0.017
		12.85	-0.53	-0.69	1.07	1.02	0.017

Table 18: Comparisons between measured and expected phase values inside each straw for ferritin solutions at both perpendicular and parallel orientations at different echo times. The meaning of each column is described in the caption of Table 15, except that the expected phase values (Phase_{theory}) are calculated from results in Tables 16 or 17, depending on whether SHARP or the high-pass filter was used to remove the background phase.

10) Status of SQUID-based magnetometer for measuring the magnetic moment of each sample

Due to the national liquid helium crisis, we have not been able to measure our samples with a SQUID-based magnetometer in our Physics Department. In responding to the helium crisis, the Physics Department had already moved all helium consumed equipment to the basement and reinstalled them between April and July 2013. However, after the reinstallations, the Physics Department had identified some problems in the basement. Thus they are now in the process of moving all the helium consumed equipment to the third floor of their building. We are hoping that they will be able to reinstall all the equipment by the end of this year and then we will be able to measure the magnetic moment of each sample with the SQUID-based magnetometer.

III. Human brain modeling

Our intended human brain model (see Fig. 16) includes the red nucleus, substantia nigra, crus cerebri, thalamus, caudate nucleus, putamen, globus pallidus, vessels, grey matter, white matter in the cerebral cortex, and the cerebellum along with cerebrospinal fluid (CSF). This model is a generalized model of the structures. The input susceptibility value of each tissue is given in Table 19 and other tissue parameters are shown in Fig. 17. Relative positions of the structures will vary for different individuals and this inter-individual variability is expected. The knowledge of the general shape and positions of the structures in the brain model helps to study a general phase behavior of the structures relative to each other in the same 3D space.

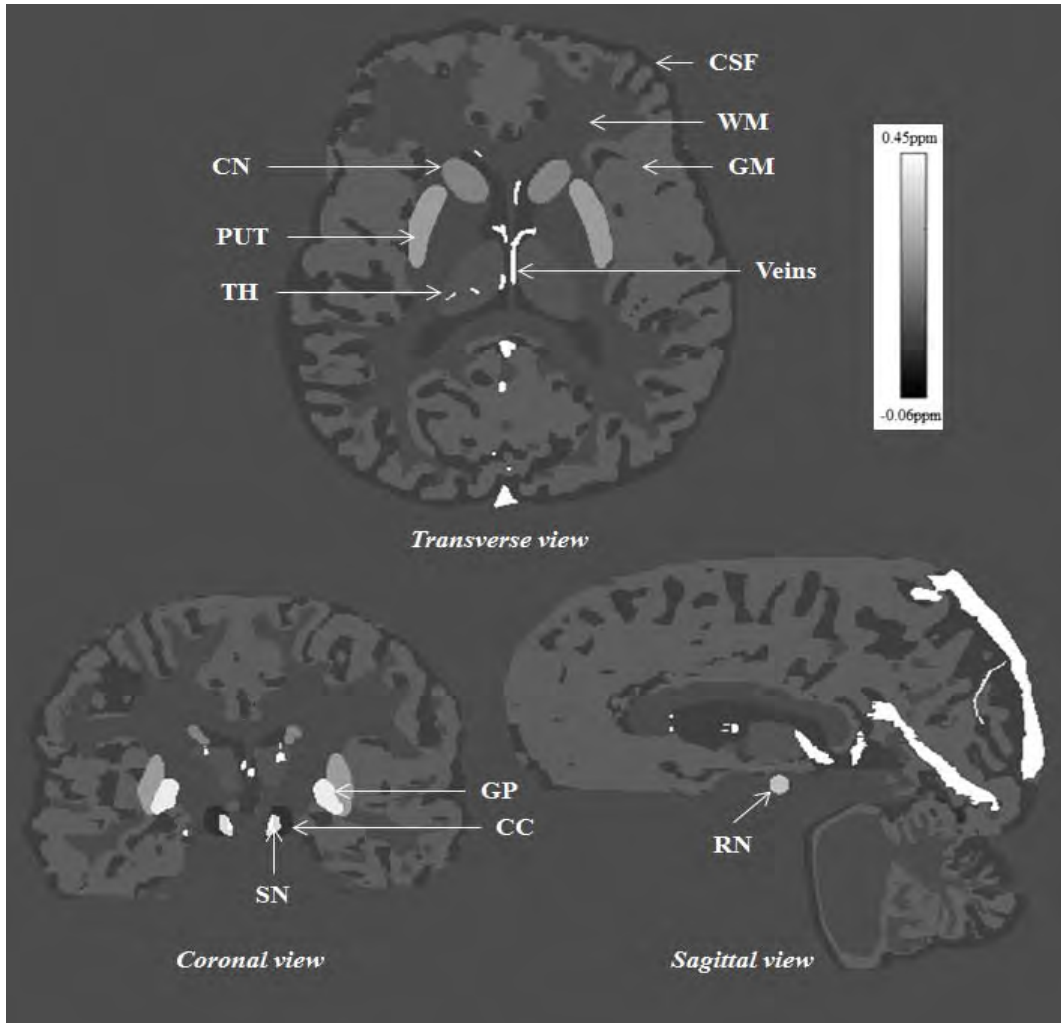


Figure 16: Transverse, Coronal, and Sagittal views of the 3D brain model. The structures are differentiated by their susceptibility values which are listed in Table 19. CN = Caudate nucleus, SN = Substantia nigra, RN = Red nucleus, GP = Globus pallidus, CC = Crus Cerebri, PUT = Putamen, TH = Thalamus, WM = White matter, GM = Grey matter, CSF = Cerebrospinal fluid.

Structure	χ value (in ppm)	Structure	χ value (in ppm)
White matter	0	Veins	0.45
Grey matter	0.02	Red Nucleus	0.13
Globus Pallidus	0.18	Substantia Nigra	0.16
Putamen	0.09	Thalamus	0.01
Caudate Nucleus	0.06	Crus Cerebri	-0.03
Cerebrospinal Fluid	-0.014		

Table 19: Susceptibility values used in our human brain model.

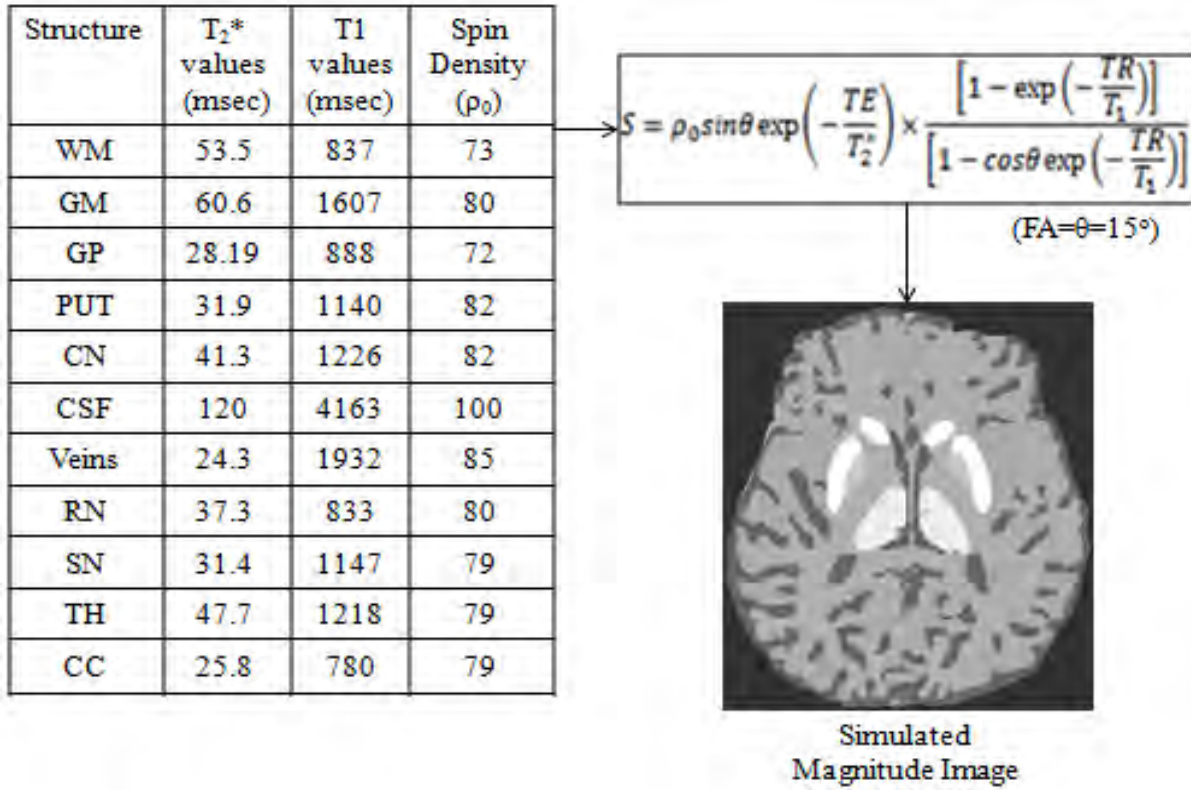


Figure 17: Spin density (ρ₀), T₁ and T₂* properties are added to each tissue in the brain model in order to generate magnitude images at main magnetic field, B₀, of 3 Tesla for different echo times (TE = 4 ms, 7 ms, 10 ms, 13 ms, 16 ms, 19 ms, 22 ms, and 25 ms) using Eq. (2) where flip angle of 15° is used. The reasonable values for ρ₀, T₁ and T₂* are selected from real data processing (for spin density and T₂* values of basal ganglia structures) and literature at TR = 35 ms.

1) Simulations of magnitude images and phase images

We first simulate the brain with a matrix size of 512 × 512 × 512 grid points, which corresponds to an image resolution of 0.5 × 0.5 × 0.5mm³. The biological tissues used in the model have different relaxation times T₁ and T₂*, given in Fig. 17, and susceptibility values listed in Table 19.

The magnitude signal-intensity from an rf-spoiled short-TR gradient-echo sequence is given by

$$S = \rho_0 \sin\theta \exp\left(-\frac{TE}{T_2^*}\right) \times \left[1 - \exp\left(-\frac{TR}{T_1}\right)\right] / \left[1 - \cos\theta \exp\left(-\frac{TR}{T_1}\right)\right] \quad (2)$$

where TR is the repetition time and θ is the flip angle.

2) Simulations of partial volume effects for tissues including small and large vessels

The phase simulations of the brain model can be compared with the *in vivo* human phase images by introducing confounding factors, such as partial volume effects (due to discretization of the MR signal) and white Gaussian noise (incorporated through real and imaginary part of signals).

In order to simulate the effect due to partial volume and Gibbs ringing, we performed a process analogous to the MRI image acquisition. We start by simulating magnitude and phase images, with a matrix size of 2048 x 2048 x 2048 grid points. Then, lower resolution images are obtained by taking the central 128 x 128 x 128 points of the Fourier transform of the high density matrix, followed by an inverse Fourier transform. *This new data comprises of experimental artifacts such as Gibbs ringing and partial volume effects, making the phase behavior much more realistic.*

Figure 18 shows the changes in susceptibility values due to the partial volume effect, before and after applications of post-processing techniques such as homodyne high-pass filter (with different sizes) and SHARP. The susceptibility values were quantified using our developed SWIM (susceptibility weighted imaging mapping) program [Haacke et al., 2010]. The diameter of a septal vein (2 pixels) is much smaller than that of the straight sinus (8 pixels). Hence, the phase integration due to the partial volume effect clearly affects the susceptibility quantification of septal vein more than that of the straight sinus.

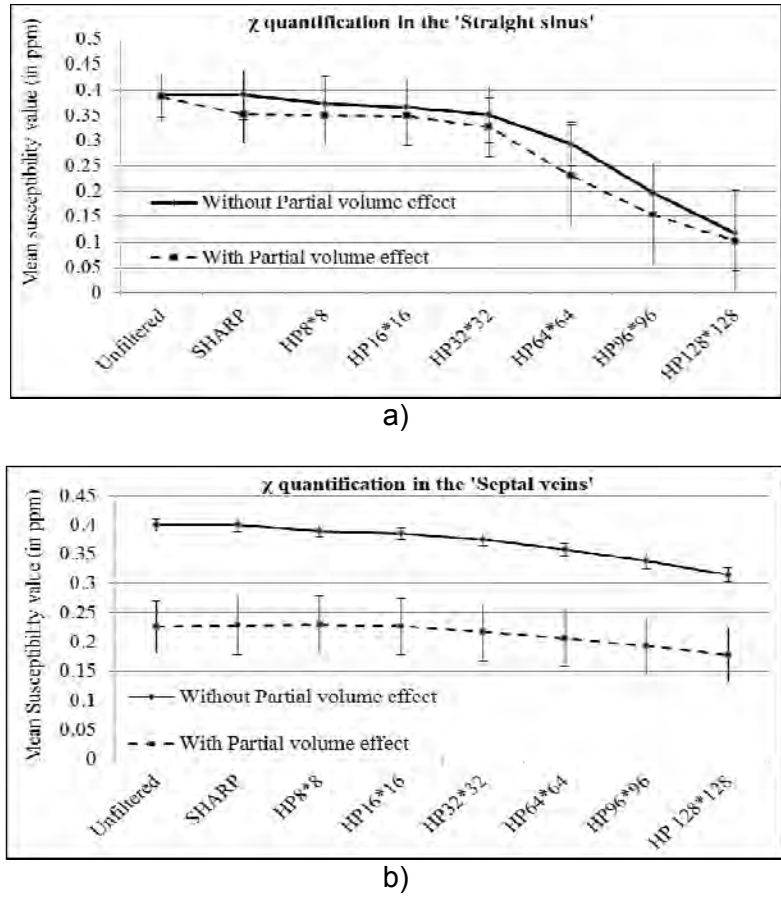
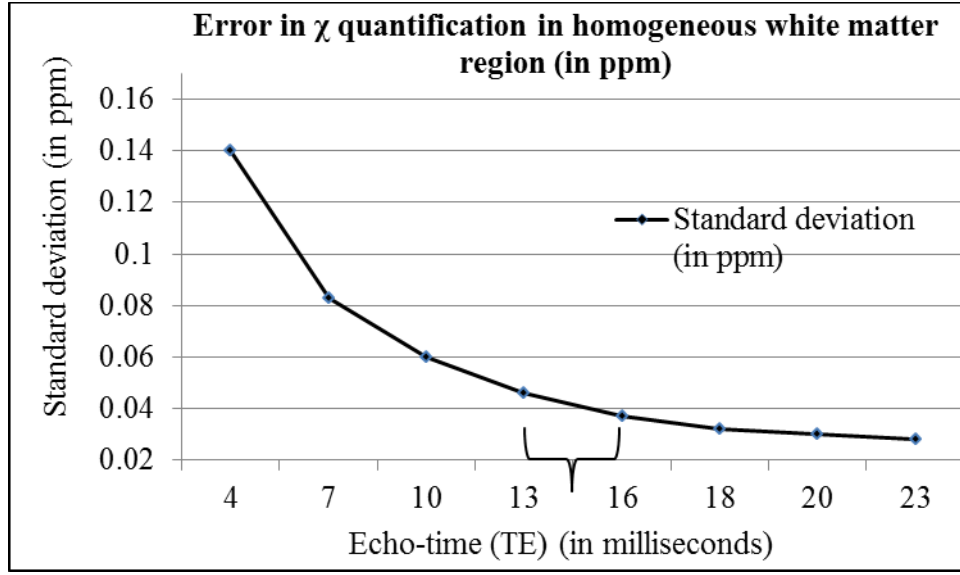


Figure 18: Mean susceptibility value measurements of (a) the straight sinus and (b) septal veins, from the susceptibility maps, generated from filtered and unfiltered phase, before and after simulating the partial volume effects (and mimicking the discrete sampling of the MR signal). The susceptibility value of the septal vein is severely affected by the partial volume effect. The diameter of the straight sinus is around 8 pixels and the diameter of the septal vein is 2 pixels in the model. The initial susceptibility value inside these veins was set to, $\Delta\chi = 0.45$ ppm.

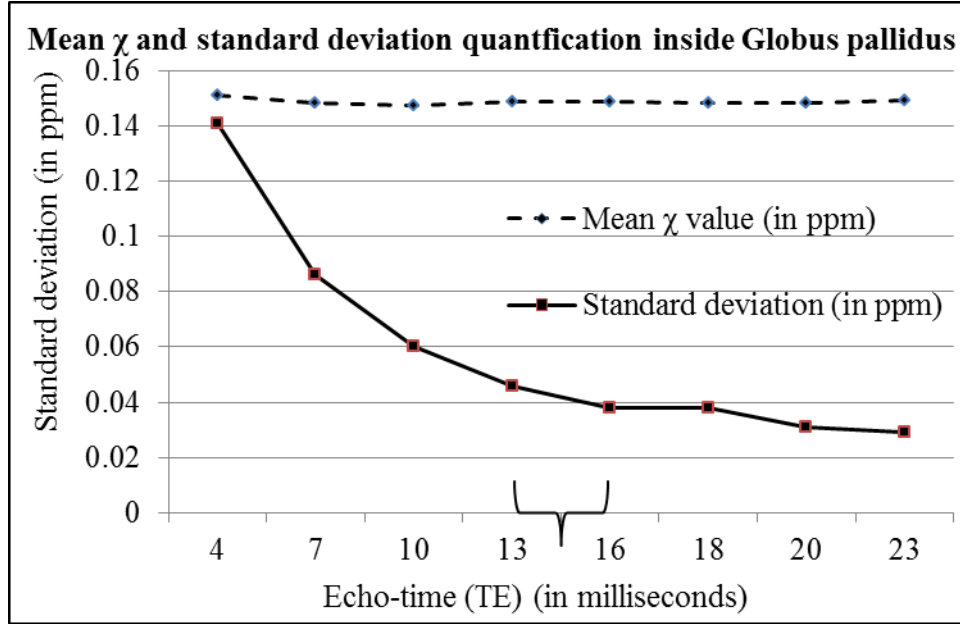
3) Estimating the ideal echo time for SWIM

One of the critical features in assessing iron with quantitative susceptibility mapping (QSM) is the choice of echo time. This is particularly important for traumatic brain injury where high iron content can exist in microbleeds.

As seen in Fig. 19, the error in the susceptibility maps decreases as we increase the echo time. The reduction in error seems significant between $TE = 4$ ms and $TE = 13$ ms. It should be noted that when the echo time equals to the T_2^* value of the structure, it produces high SNR in phase images. The standard deviation in phase images is equal to the inverse of SNR in magnitude images. This may be the reason why we see the lowest standard deviation at around $TE = 20$ ms (T_2^* (globus pallidus) = 19 ms in the model). The susceptibility values generated from echo times longer than 16 ms do not show much reduction in errors. This fact suggests that using echo time of 13 ms will be a good practice for susceptibility quantifications with SWIM, as such a choice allows us to shorten the acquisition time.



a)



b)

Figure 19: The relationship between echo time and error in susceptibility quantifications using SWIM. A Gaussian noise (mean/standard deviation = 10/1) was added to the real and imaginary parts of the simulated data. (a) The measurements are performed in a homogeneous white matter region where the expected mean value is ideally zero. A small homogeneous white matter region of 50 pixels in size was chosen to calculate the mean susceptibility value. (b) The measurements of mean χ value and the standard deviation are calculated inside the Globus pallidus ($\chi_{\text{(globus pallidus)}} = 0.18$ ppm). A total of 100 pixels inside the globus pallidi, avoiding the edges, were used for calculating the mean susceptibility and its associated uncertainty.

4) Human brain model simulations with more grid points and results

We have further properly improved and simulated human brain magnitude and phase images by including the partial volume effects due to discrete voxels containing MR signals, with a final matrix size of 256^3 . This matrix size mimics the typical 1 mm isotropic images for better depiction of tissues. This simulation procedure required a very long computer time, as we first generated a 4096^3 complex matrix, Fourier transformed the 4096^3 complex matrix, took the central 256^3 points of the matrix, and performed an inverse Fourier transform of the 256^3 matrix to obtain images in the spatial domain. Such a ratio (or higher) between the two matrices is needed for properly generating the partial volume effect for relatively small objects. The Gaussian noise can be

added to the 256^3 complex images. This new dataset comprises of actual artifacts such as Gibbs ringing and partial volume effects, making the phase behavior much more realistic. Examples are shown in Fig. 20. We can see clear differences of small structures between the high and low density matrices.

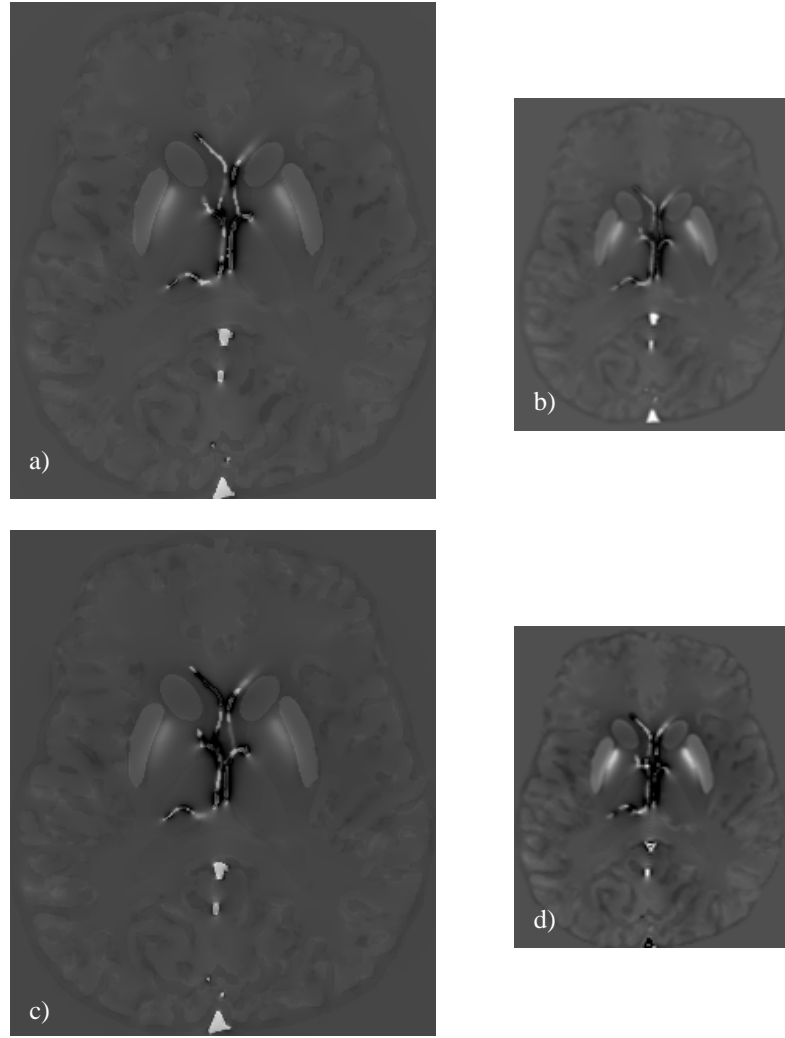


Figure 20: Comparisons between the simulated phase images without partial volume effects (a) and (c) and with the partial volume effects (b) and (d). Imaging parameters used for (a) and (b) are $B_0 = 3$ T and $T_E = 15$ ms and for (c) and (d) are $B_0 = 3$ T and $T_E = 29$ ms. Partial volume effects are generated by cropping the central $256 \times 256 \times 256$ k-space elements from a high grid matrix of $4096 \times 4096 \times 4096$. K-space cropping also introduces Gibbs ringing in the image.

Addition of the partial volume effects in the simulations is a key factor in understanding the actual phase data. When the current SWIM technique was applied, the mean susceptibility inside a relatively small vessel, such as the right septal vein with a diameter of 2 pixels (white arrows in Fig. 21), shows significant reduction of the susceptibility value after introducing the partial volume effect. The quantified susceptibility inside the right septal vein quantified by SWIM based on original images without the partial volume effect is $\Delta\chi = 0.38 \pm 0.02$ ppm, which is about 16% lower than the actual value of $\Delta\chi = 0.45$ ppm. On the other hand, the mean susceptibility value of the same vein quantified by SWIM from images with the partial volume effect is $\Delta\chi = 0.17 \pm 0.03$ ppm, with a much worse error of 62%. These values also agree with results shown in Fig. 18.

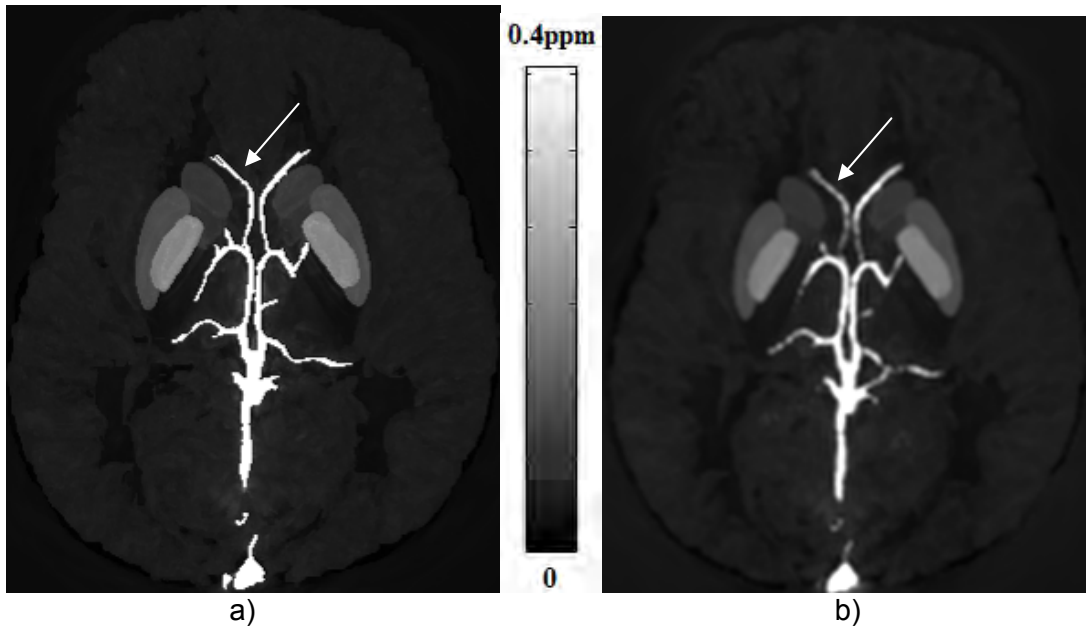


Figure 21: Maximal Intensity Projection (MIP) images of the susceptibility maps. (a) MIP (over 42 slices) of the susceptibility maps generated from the original phase images, and (b) MIP (over the same FOV as in (a)) of the susceptibility maps generated from phase images with the partial volume effect. The susceptibility values inside veins are fairly a constant for (a) irrespective of the size of a vessel, whereas in (b) the susceptibility values of veins show variations, depending on the vessel size. The white arrow identifies the right septal vein, where the reduction can be clearly seen in (b).

After the above simulations, Gaussian noise is added to the real part and imaginary part of the 256^3 complex images. An example image with an SNR of 20:1 is shown in Fig. 22. Constructing such a numerical phantom through forward simulations with known input susceptibility values is essential for our tests of methods in the future. Below we present some examples.

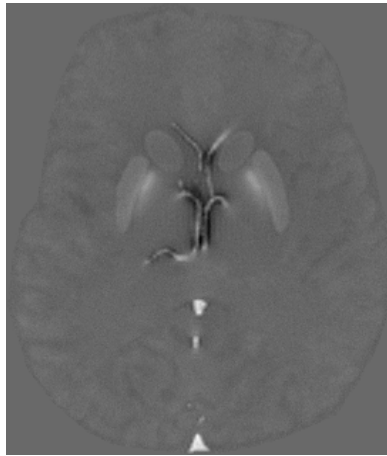


Figure 22: An example of the phase images including the partial volume effects, Gibbs ringing effects, and Gaussian noise.

5) Accuracy in background phase removal methods with SWIM: SHARP, homodyne high-pass filtering, and variable high-pass filtering tested on our human brain model

In this section, the errors in estimated susceptibility values using different background phase removal methods are evaluated on our simulated 3D brain model. Particularly, three phase processing methods are evaluated: SHARP, homodyne high-pass filtering (HP) and variable high-pass filtering (VHP). Homodyne high-pass filtering is the most traditional phase processing method and it and SHARP have been also used with CISSCO in earlier sections. It is known that high-pass filtering process will lead to reduction of phase values, especially

to relatively large structures. SHARP is based on the spherical mean value property of the background field, but the accuracy of SHARP depends on the choices of the kernel size (i.e., volume of a sphere inside which phase values are added) and the regularization threshold. The variable high-pass filtering is also based on spherical mean value theorem. It uses variable filter sizes to reduce the signal loss to structures in central part of the brain.

a) Theory

SHARP

Assuming that the total field variation ΔB can be considered as a combination of the local field variation and the background field variation

$$\Delta B = \Delta B_l + \Delta B_b \quad [3].$$

In different phase/field processing methods, different properties of the background field are utilized. In SHARP it is assumed that the background field variation, ΔB_b has the spherical mean value property (SMV) inside the brain region (the value of certain pixel, e.g., A, of ΔB_b is the mean field value for all pixels in a sphere, centered at A).

The first step of SHARP is similar to a high-pass filtering

$$\Delta B - \Delta B * s = (\Delta B_l - \Delta B_l * s) + (\Delta B_b - \Delta B_b * s) = \Delta B_l - \Delta B_l * s \quad [4],$$

where s is a normalized sphere in image domain (i.e., a numerical sphere which is 1/num for pixels inside the sphere and 0 outside, and “num” is the number of pixels inside the sphere. Thus, this is essentially an averaging filter. * denotes for the convolution process).

Let's denote the result of Eq. 4 as ΔB^f . Since the convolution does not give correct value near the edge, an eroded mask, M has to be applied. Equation 4 with the application of the mask can be written as

$$\Delta B^f = \Delta B_l * (\delta - s) \cdot M \quad [5].$$

It is possible to solve Eq. 5 for ΔB_l

$$\Delta B_l = \Delta B^f * (\delta - s)^{-1} \quad [6]$$

where $(\delta - s)^{-1}$ is the inverse of the kernel $(\delta - s)$. This inverse process has to be regularized typically through a Fourier domain truncation (TSVD) by setting a threshold, th . i.e., the inverse of the Fourier transform of $(\delta - s)$ is set to 0 when the absolute value of the Fourier transform of $(\delta - s)$ is below th . Obviously, the accuracy of SHARP is dependent on the size of the sphere that is used in Eq. 4, and the threshold th is the deconvolution process in Eq. 6.

Homodyne high-pass filtering

In Homodyne high-pass filtering, the background field component in Eq. 3 is assumed to have low spatial frequency and hence can be removed through a high-pass filtering, as shown below

$$Mag_{hp} e^{i\phi_{hp}} = FT^{-1} \{ FT [Mag \cdot e^{i\phi}] \cdot Hann \} \quad [7],$$

$$\phi_{hp} = \arg \left(e^{i(\phi - \phi_{hp})} \right) \quad [8].$$

The size of the Hann window in k-space in Eq. 7 is usually selected as 64 x 64 in order to obtain the low spatial-frequency components and to avoid too much signal loss to the local field variation.

b) Theory: variable high-pass filtering

In variable high-pass filtering, the background field component will be estimated by applying a spherical mean filter to the original phase images

$$\Delta B * s = \Delta B_b + \Delta B_i * s \quad [9].$$

and the high-pass filtered image is calculated as

$$\Delta B_{hp} = \Delta B - \Delta B * s \quad [10].$$

This is the same as Eq. 4. However, when the size of s is large enough, the average value of the local field is close to 0 ($\Delta B_i * s \approx 0$). Thus,

$$\Delta B_{hp} \approx \Delta B - \Delta B_b = \Delta B_i \quad [11].$$

However, the size of the spherical kernel s is limited by the dimension of the image matrix. In addition, since the spherical mean value property cannot be applied across the edge of the brain, we gradually reduce the size of the spherical filter from the central part of the brain to the periphery. A large spherical window is used for the central region (and is applied in image domain and can be considered as a very mild high-pass filter), and smaller spherical windows (stronger high-pass filter) are used for regions close to the edge.

c) Method

Phase simulations and processing

The phase images of the 3D brain model were calculated using the fast-forward field calculation shown in Cheng et al. [2009b] with a magnetic field strength of 3 T at an echo time of 10 ms. The susceptibility of the sinuses was set to be 9 ppm, in order to simulate the background field variations induced by the air-tissue interfaces. Phase images of the brain structures Φ_{brain} and of the sinuses Φ_{sin} were calculated independently. The sum of these two components is referred to as the phase images of the brain model (Φ_{sum}). An example image is shown in Fig. 23.

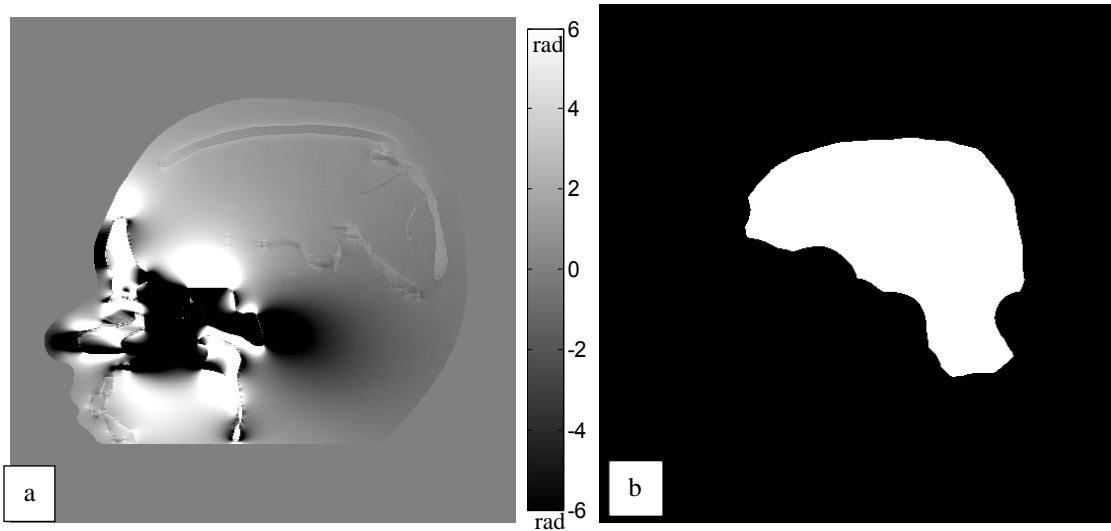


Figure 23: (a) Simulated phase image of the brain model and (b) the reference region used for evaluating the accuracy in the processed phase images after the background phase is removed.

SHARP with different kernel sizes ranging from 1 pixel to 16 pixels (i.e., radius of the sphere used in SHARP) and different thresholds (th ranging from 0.005 to 0.1 with a step size 0.005) was applied to Φ_{sum} . A brain mask was used in SHARP (Eq. 5). Note that the mask has to be eroded by different distances depending on the size/radius of the spherical kernel. Thus the number of eroded brain pixels was also measured for different kernel sizes.

Homodyne high-pass filter with a k-space window size of 64 x 64 was also applied to ϕ_{sim} for comparisons. Variable high-pass filter was applied with a big sphere (radius = 32 pixels) for central regions and with smaller spheres for regions close to the edge. At the edge, the kernel size/radius of the sphere is 1 pixel. The size of the spherical kernel for a particular pixel was determined as the distance from that pixel to the nearest edge of the 3D brain.

The processed phase images, which correspond to the local phase induced by various brain structures, were compared with the simulated phase of purely various structures inside the brain (ϕ_{lsim}). RMSE (defined in Eq. 12) was calculated in a reference region which corresponds to the eroded mask in SHARP when the largest sphere was used (see Fig. 23), for all three background phase removal methods.

$$RMSE = \sqrt{\frac{\sum (\phi_{processed} - \phi_{lsim})^2}{N}} \quad [12],$$

where N is the total number of pixels in the reference mask.

Susceptibility quantification

Susceptibility maps were generated using a truncated k-space division approach, with a threshold value of 0.1 [Haacke et al., 2010]. The mean susceptibility values were measured for a total of 9 different structures, as listed in Table 20. In order to independently analyze the errors in susceptibility quantifications induced by background phase removal methods, reference susceptibility maps were generated using the ideal phase images containing only the local structures, with the same k-space threshold value. The errors in the reference susceptibility maps were purely caused by the inverse filter in SWIM.

The relative error in susceptibility quantification of each structure is calculated as $\frac{\chi_{est} - \chi_{true}}{|\chi_{true}|}$, where χ_{est} is the estimated susceptibility value and χ_{true} is the true susceptibility value. The effects of the kernel size and threshold in SHARP were studied using the overall RMSE in the processed phase and susceptibility maps, as well as the relative error in estimated susceptibility for each structure. The overall RMSE in susceptibility maps were also calculated in a similar way to Eq. 12.

d) Results

Methods	True Susceptibility	Original Phase	SHARP (r=8, th=0.02)	SHARP (r=8, th=0.05)	HP64	VHP
Veins	0.45	0.41 ± 0.04	0.40 ± 0.04	0.39 ± 0.04	0.33 ± 0.07	0.40 ± 0.05
Thalamus	0.01	0.01 ± 0.02	0 ± 0.02	0 ± 0.02	0 ± 0.02	0 ± 0.02
Red Nucleus	0.13	0.12 ± 0.01	0.11 ± 0.01	0.11 ± 0.01	0.07 ± 0.02	0.11 ± 0.01
Substantia Nigra	0.16	0.15 ± 0.02	0.14 ± 0.02	0.14 ± 0.02	0.10 ± 0.04	0.13 ± 0.02
Subthalamic Nucleus	0.20	0.19 ± 0.02	0.19 ± 0.02	0.19 ± 0.02	0.14 ± 0.03	0.18 ± 0.02
Crus Cerebri	-0.03	-0.03 ± 0.02	-0.04 ± 0.02	-0.04 ± 0.02	-0.03 ± 0.03	-0.04 ± 0.02
Caudate	0.06	0.05 ± 0.01	0.04 ± 0.01	0.04 ± 0.01	0.02 ± 0.02	0.04 ± 0.01
Putamen	0.09	0.08 ± 0.01	0.06 ± 0.01	0.04 ± 0.01	0.01 ± 0.03	0.05 ± 0.01
Globus Pallidus	0.18	0.16 ± 0.01	0.14 ± 0.01	0.12 ± 0.01	0.05 ± 0.03	0.11 ± 0.01

Table 20: The quantified susceptibility values (mean ± st. dev. in ppm) using SWIM for different structures and background phase removal methods. The first column lists the 9 structures. The second column lists the true susceptibility values in ppm. The third column lists results from the reference images, without background phase added into images. The fourth and the fifth column list results for SHARP with radius = 8 pixels, threshold = 0.02 and 0.05, respectively. The sixth column lists the results after the application of a 64 x 64 high pass filter. The seventh column lists results from the Homodyne high-pass filter.

The RMSE estimated from processed phase images for different kernels (radii) and thresholds in SHARP are shown in Fig. 24a. These RMSE represent overall error levels in the phase images processed by SHARP. For a given kernel size, a minimal RMSE can be seen from Fig. 24a and is plotted in Fig. 24c. This minimal RMSE is decreasing as the size of the kernel increases (Fig. 24c), but the information loss (the number of eroded pixels) also increases (Fig. 24d). At the minimal RMSE for a given kernel size, the optimal threshold values are shown in Fig. 24b. As a comparison, the RMSE for the HP processed phase is 0.05 radian and the RMSE for the VHP processed phase is 0.02 radian.

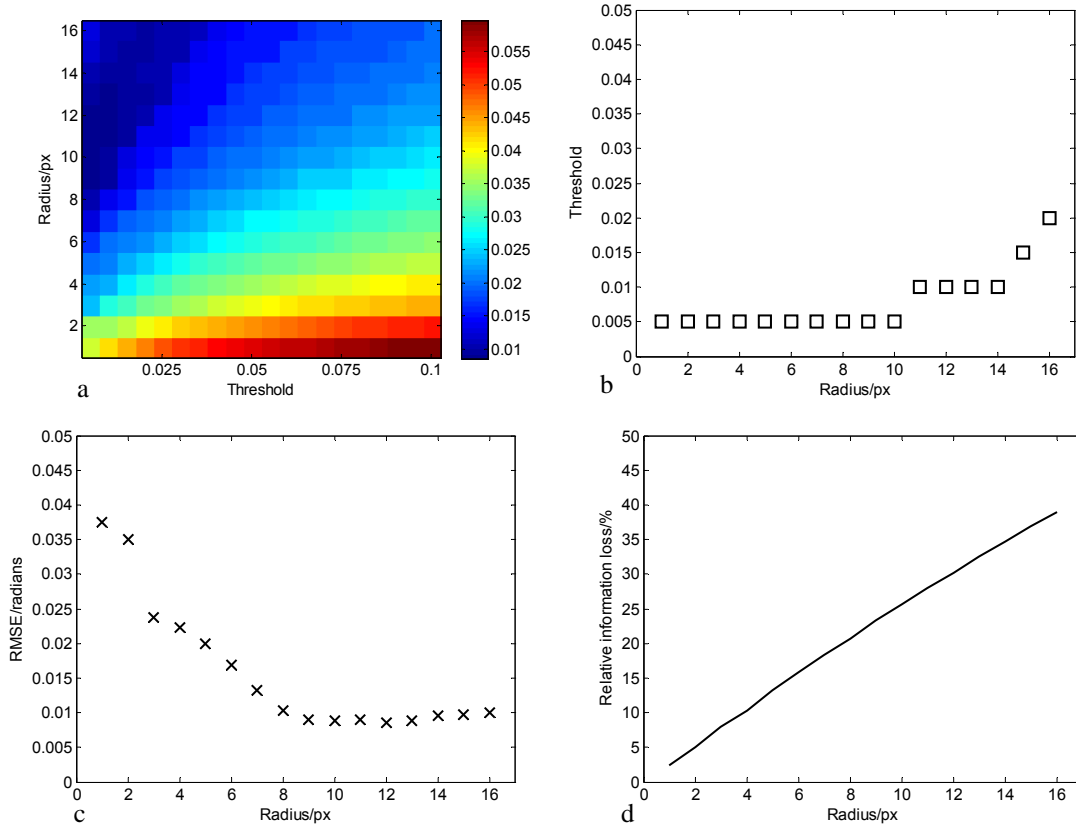


Figure 24: (a) RMSE from phase images for different radii of the spherical kernels and different threshold values used in SHARP. (b) Optimal threshold (minimal RMSE) for different radii. (c) Minimal RMSE obtained from the optimal threshold shown in (a) for each given kernel (radius). (d) Relative information loss (the number of eroded pixels over the total number of pixels in the brain mask) for different spherical kernels (radii).

The overall RMSE in the susceptibility maps, generated from SHARP processed phase images are shown in Fig. 25a. The minimal RMSE for each kernel size is shown in Fig. 25b. These two figures resemble the results shown in Figs. 24a and 24c.

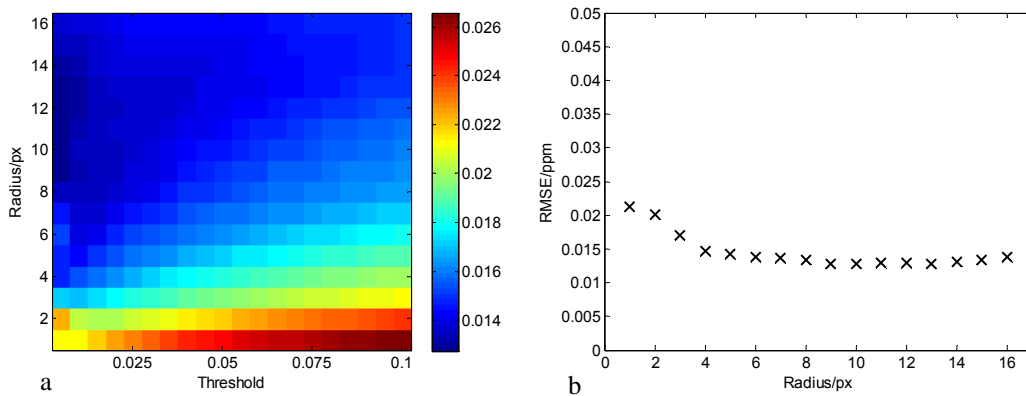
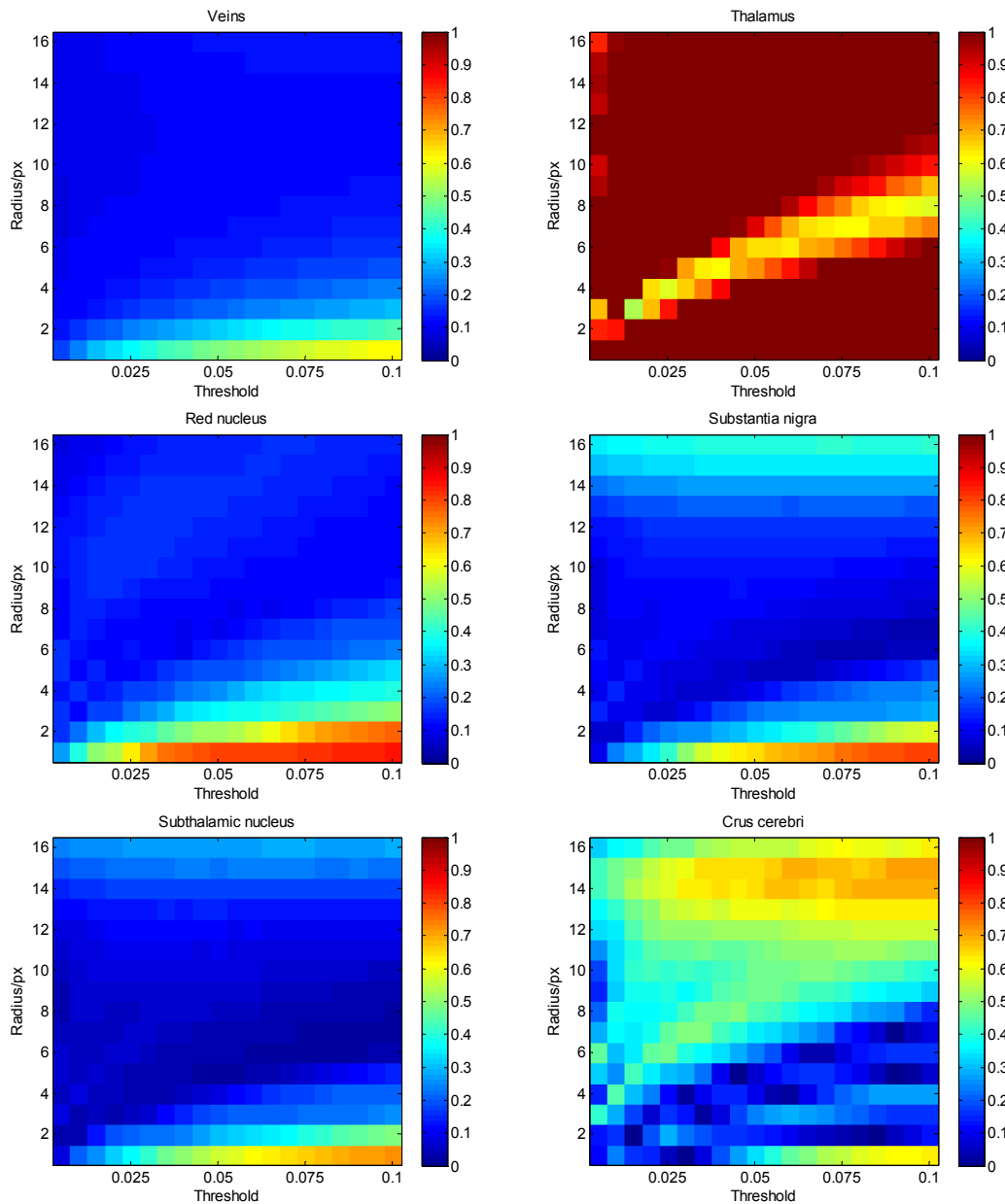


Figure 25: (a) Overall RMSE in susceptibility quantification for different kernel sizes (radii) and different thresholds. (b) The minimal RMSE for a given kernel size (radius).

Generally speaking, larger radii of spherical kernels lead to smaller errors. In addition, the radius of the sphere should be larger than 4 pixels, in order to maintain a low RMSE. However for each individual structure listed in Table 20, the optimal kernel size and threshold may vary, as shown in Fig. 26, which shows the relative errors of susceptibility quantifications (in absolute values). For basal ganglia structures, the inverse filter itself will cause an underestimation around 10%-20%. The SHARP and VHP processed phase images lead to an underestimation of around 30%-40%. This suggests that SHARP and VHP will cause roughly 20% error for basal ganglia structures. For other structures such as veins, the underestimation is smaller. The most severe error is seen from thalamus. In this case, the errors in the measured susceptibility values are high for all three phase processing methods. Even using the phase images without the background field in susceptibility quantifications, the uncertainties are still high. This might suggest that the problem is largely caused by the inverse filter itself.

From Fig. 26, it can be seen that generally the errors in susceptibility estimates decrease as the radius of the SHARP kernel increases (except for substantia nigra and crus cerebri). Considering the relatively higher signal loss at larger kernel sizes, a reasonable choice for the size of the spherical kernel in SHARP should be around 6-8 pixels. The threshold value should be kept as small as possible ($th \leq 0.05$). In some situations, a higher threshold value may be desired, in order to suppress non-harmonic phase artifacts.



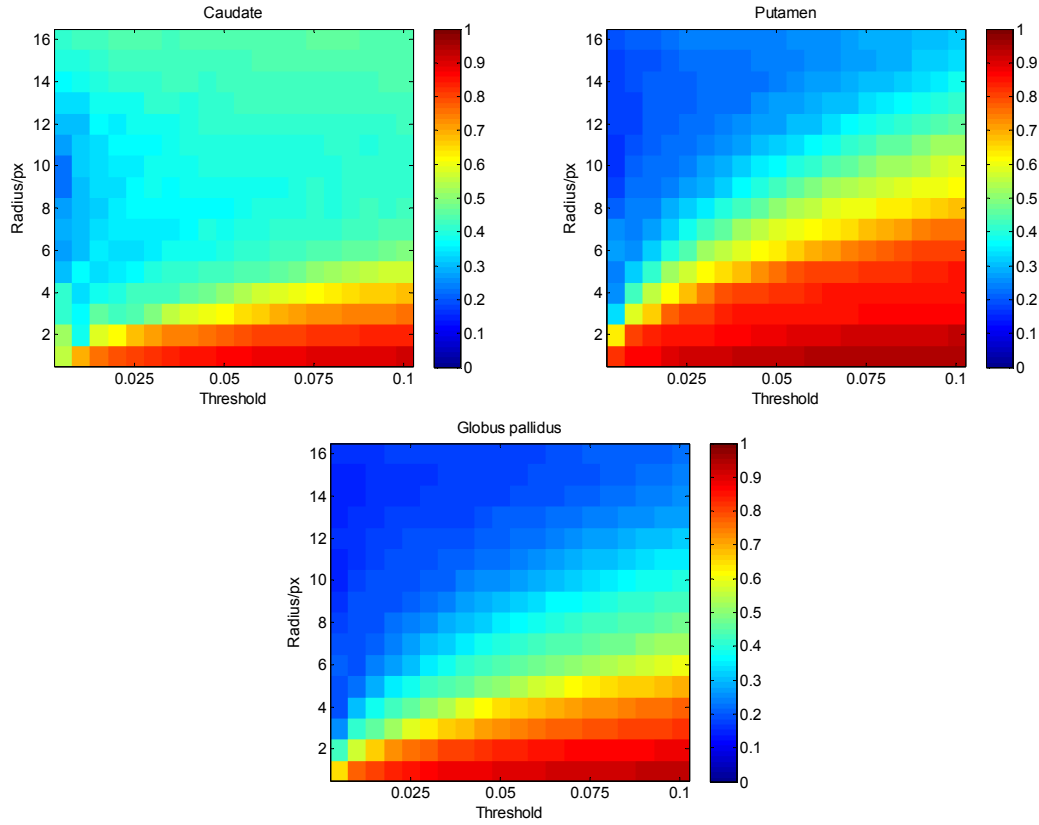
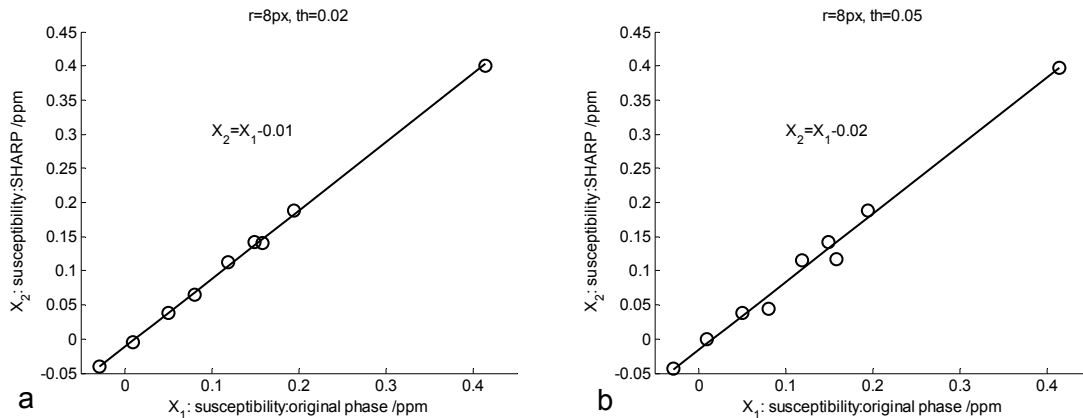


Figure 26: Relative errors measured from susceptibilities (in absolute values) using different parameters in SHARP for 9 different structures.

In addition, the estimated susceptibilities using the original phase images (i.e., images without the background phase) were plotted against the estimates using the processed phase images, as shown in Fig. 27. Each x-axis shows the susceptibility estimates obtained using the original phase images, and each y-axis shows the estimates obtained through the three background phase removal methods. Figures 27a and 27b are obtained through SHARP with different regularization parameters (see Table 20).

Figure 27 demonstrates possible effects of different background phase removal methods on susceptibility quantifications. When using SHARP with proper thresholds, the estimated susceptibilities are almost the same as those estimated using the original phase (the slope is close to 1). However, it is also noticed that, when the threshold value becomes larger, the correlations between the estimates become worse. On the other hand, using the phase images processed by the homodyne high-pass filter (64 x 64 window size), the susceptibilities are certainly underestimated. Using the phase images processed by variable high-pass filter, again the estimated susceptibilities are almost the same as those obtained from the original phase images.



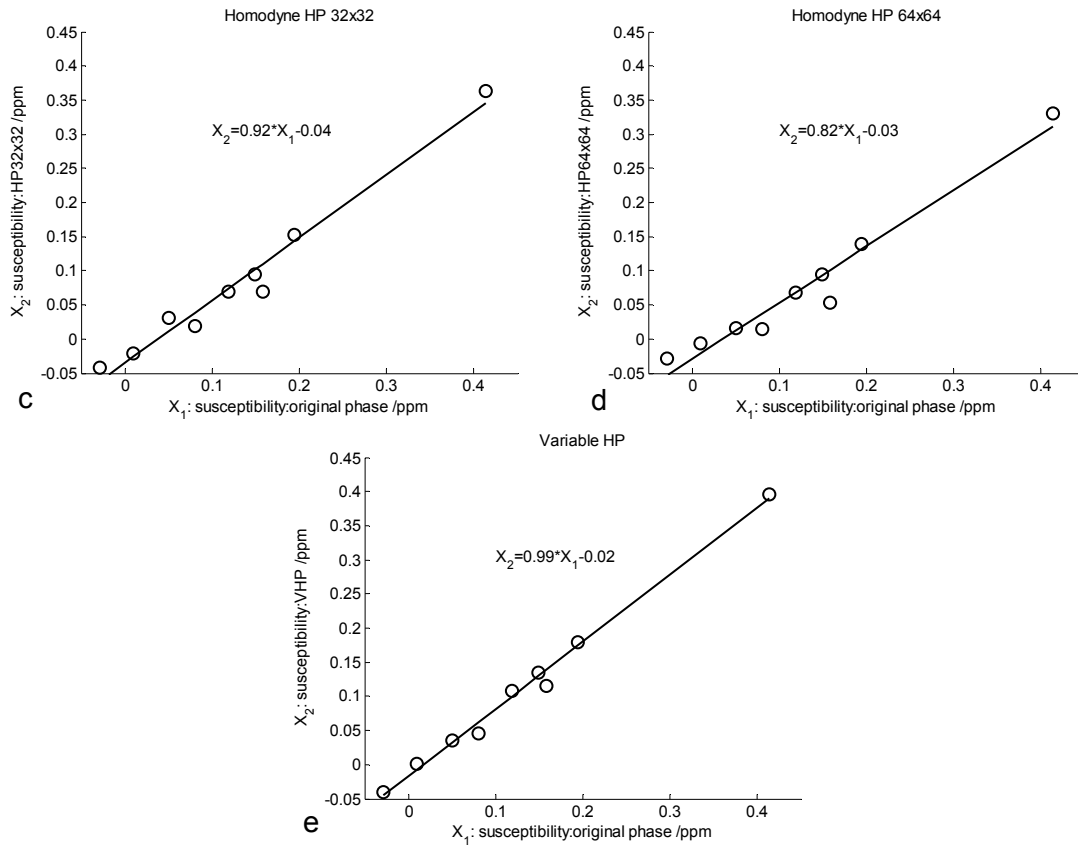


Figure 27: Estimated Susceptibility values using the original phase vs. different background phase removal methods: (a) SHARP (radius = 8 pixels, th = 0.02), (b) SHARP (radius = 8 pixels, th = 0.05), (c) Homodyne HP 32 x 32, (d) Homodyne HP 64 x 64, and (e) Variable HP.

e) Discussion

It can be concluded that errors derived from SHARP processed phase images decrease as the size of the spherical kernel increases (Fig. 25). This is mainly due to the deconvolution process, as larger spherical kernel leads to less amplification of any remnant background field.

Clearly the variable high-pass filtering method leads to less underestimation in susceptibility quantifications, compared with the traditional homodyne high-pass filter. In variable high-pass filter, the spherical kernel is used to generate a low-pass filtered phase image (the averaged phase image) which is close to the background phase. No additional deconvolution is required. Thus there is no need to select any regularization parameter as it is done in SHARP. As can be seen from the results, variable high-pass filtering leads to similar results as in SHARP.

The SHARP and VHP processed phase images lead to small errors for most structures. However for thalamus or structures with small susceptibility values (below 0.1 ppm), even though some structures are large (occupy many pixels), the errors from susceptibility quantifications are large. On the other hand, for veins and basal ganglia structures with relatively larger susceptibility values (above 0.1 ppm), the errors seem small. However, Table 20 shows that the errors of susceptibility value estimated from Globus Pallidus with SHARP and VHP are not small. *This indicates that some systematic errors in SHARP and VHP have not been identified yet.* This subtlety is also supported by results shown between Table 11 and Table 12, as discussed earlier. One theoretical problem of SHARP is that the mean value theory for SHARP becomes *invalid* when the spherical kernel crosses the boundary of an object. This includes the situation when an object is completely enclosed by the volume of the spherical kernel, as the mean value theory was applied to the surface of the spherical kernel rather than its volume. Thus, a better background phase removal technique is still useful to be developed.

6) Evaluating the errors in Laplacian based phase processing algorithms

The Laplacian based phase processing algorithms are a substitute for the phase unwrapping procedure. As we mentioned before, phase unwrapping is needed for SHARP and quadratic fitting methods. Thus, it becomes important to evaluate errors caused by these algorithms. Currently there are mainly two ways to calculate the Laplacian of phase. One method is to use the phase differences and discrete Laplacian operator, and the other is to use the sine and cosine functions together with Fourier transform. While the former method is essentially a discrete approximation of Laplacian, the latter method is based on continuous functions of phase. Given the fact that MRI phase images are discrete, it might be more consistent to use all operators in discrete forms. In this report, the errors associated with both phase processing methods are evaluated using both numerical model and *in vivo* data.

a) Theory

The total field can be written as the sum of the local field and background field

$$\Delta B(r) = \Delta B_b(r) + \Delta B_l(r) \quad [13]$$

In a homogenous region, the background field satisfies the Laplace's equation

$$\nabla^2[\Delta B_b(r)] = 0 \quad [14]$$

From Eqs. 13 and 14, the relation between the total field and local field can be derived as

$$\nabla^2[\Delta B(r)] = \nabla^2[\Delta B_l(r)] \quad [15]$$

The left side of Eq. 15, the Laplacian of the total field can be calculated using the discrete Laplacian operator.

$$\nabla^2\phi = \phi^{i+1,j,k} + \phi^{i-1,j,k} + \phi^{i,j+1,k} + \phi^{i,j-1,k} + \phi^{i,j,k+1} + \phi^{i,j,k-1} - 6\phi^{i,j,k} \quad [16]$$

where $\phi^{i,j,k}$ is the phase value of the pixel at index (i,j,k), and $\phi = -\gamma\Delta BTE$ for a right-handed system. The right hand side of Eq. 16 can be calculated through the differences of two neighboring pixels in the original phase image with phase wraps (ϕ_w). For example,

$$\phi_{i+1,j,k} - \phi_{i,j,k} = \arctan\{\exp[i(\phi_w^{i+1,j,k} - \phi_w^{i,j,k})]\} \quad [17]$$

In this study, Eqs. 16 and 17 will be denoted as “discrete operators”. Alternatively, as proposed by Schofield and Zhu [2003], the Laplacian of the unwrapped phase can be calculated from ϕ_w

$$\nabla^2\phi = \cos\phi_w \nabla^2(\sin\phi_w) - \sin\phi_w \nabla^2(\cos\phi_w) \quad [18]$$

The Laplacians can be calculated using properties of Discrete Fourier Transforms

$$\nabla^2 f(r) = -\frac{4\pi^2}{N^2} FT^{-1}\{k^2 FT[f(r)]\} \quad [19]$$

As both Eqs. 18 and 19 are for continuous functions, they will be denoted as “continuous operators” in this study. Then from Eq. 15,

$$\nabla^2\phi = \nabla^2\phi_l, \text{ or } \nabla^2(\phi - \phi_l) = 0. \quad [20]$$

Solving Eq. 20 requires boundary condition, which is usually unknown. However, if the Laplacian is calculated using Fourier transform, then periodicity is imposed on the boundary. In this case,

$$\phi = FT^{-1}\{FT[MV^2\phi]L^{-1}(k)\} \quad [21]$$

where M is an eroded brain mask, $L^{-1}(k)$ is the regularized inverse of $L(k)$, the Fourier transform of the discrete Laplacian kernel.

$$L^{-1}(k) = \begin{cases} \{FT[L(r)]\}^{-1}, & \text{when } |FT[L(r)]| > th \\ 0, & \text{when } |FT[L(r)]| \leq th \end{cases} \quad [22]$$

where th is the truncation threshold in Fourier domain, which was set as 0.015 in this study. If the continuous form of Laplacian was used, then the local phase can be reconstructed by inverting Eq. 19. Regularization is also required for inverting Eq. 19. Particularly, the truncation threshold was empirically set to be 4×10^{-4} . The whole process is illustrated in Fig. 28.

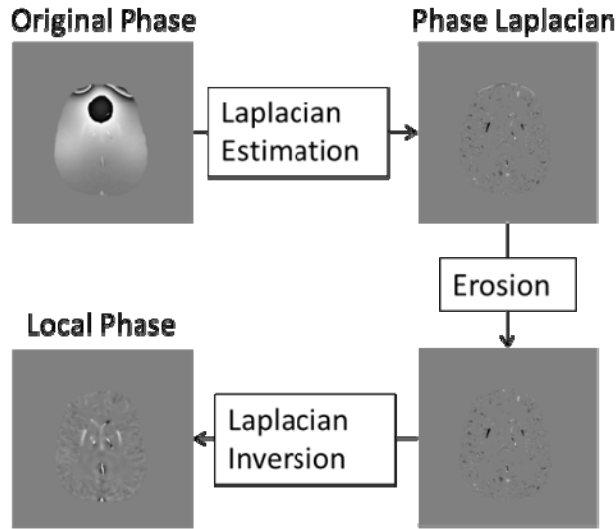


Figure 28: Illustration of the Laplacian based phase image processing steps.

b) Method

The above 3D numerical brain model was used for evaluating the Laplacian based algorithms. The background phase was added by including the air-sinuses which have a susceptibility of 9 ppm relative to the brain tissue. The phase images were simulated with $B_0 = 3$ T, $TE = 10$ ms. Aliased phase images were processed using both discrete and continuous Laplacian based algorithms.

The errors in the phase processing were evaluated by comparing the extracted local phase information, ϕ_l' in Eq. 21, with the actual local phase information produced from the forward calculations. In order to determine the effects of phase processing on susceptibility quantifications, susceptibility maps were further generated with a threshold of 0.1. Susceptibility values of the veins were measured and their relative errors were calculated.

c) Results

The Laplacians of the phase obtained using the discrete and continuous operators are shown in Fig. 29. The major differences in the Laplacians as well as in the reconstructed local phase images are associated with the veins. This difference is also seen in Fig. 30, which shows that the phase image processed using the continuous operator has errors near the veins. After susceptibility maps were generated using both the processed phase images (e.g., Figs. 29d and 29e), susceptibility values of the veins (as shown in Fig. 29d and 29e, excluding the superior sagittal sinus) were measured as 0.41 ± 0.03 ppm and 0.36 ± 0.04 ppm, for phase images processed using discrete and continuous operators, respectively. Using the discrete operator, the relative error in the measured susceptibility value is 9%, compared with the input value of 0.45 ppm. The relative error is 20% for the continuous operator.

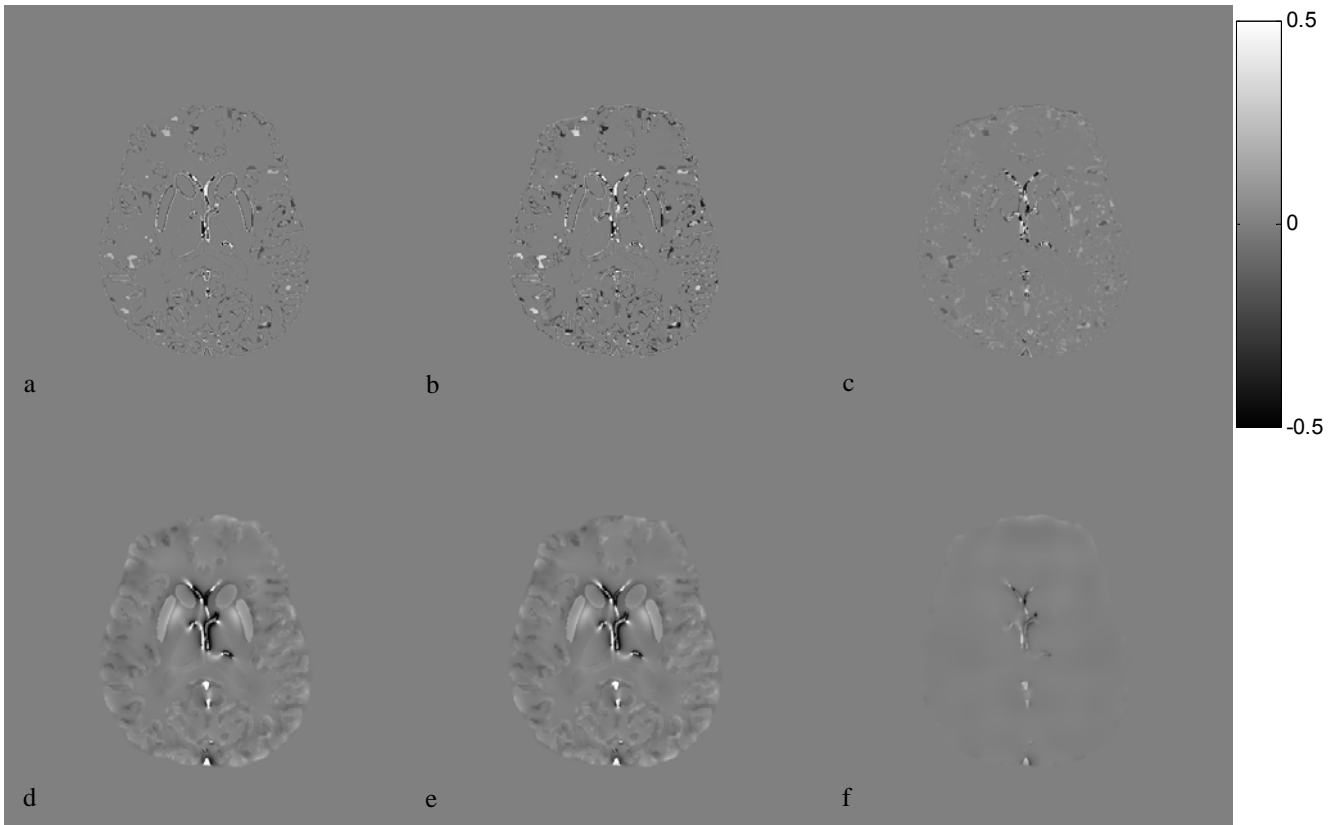


Figure 29: (a) Laplacian of the phase calculated using the discrete Laplacian operator. (b) Laplacian calculated using the continuous operator. (c) The resulting image of (b) subtracted from (a). (d) Local phase images obtained using the discrete Laplacian operator. (e) Phase image using the continuous operator. (f) The resulting image of (e) subtracted from (d).

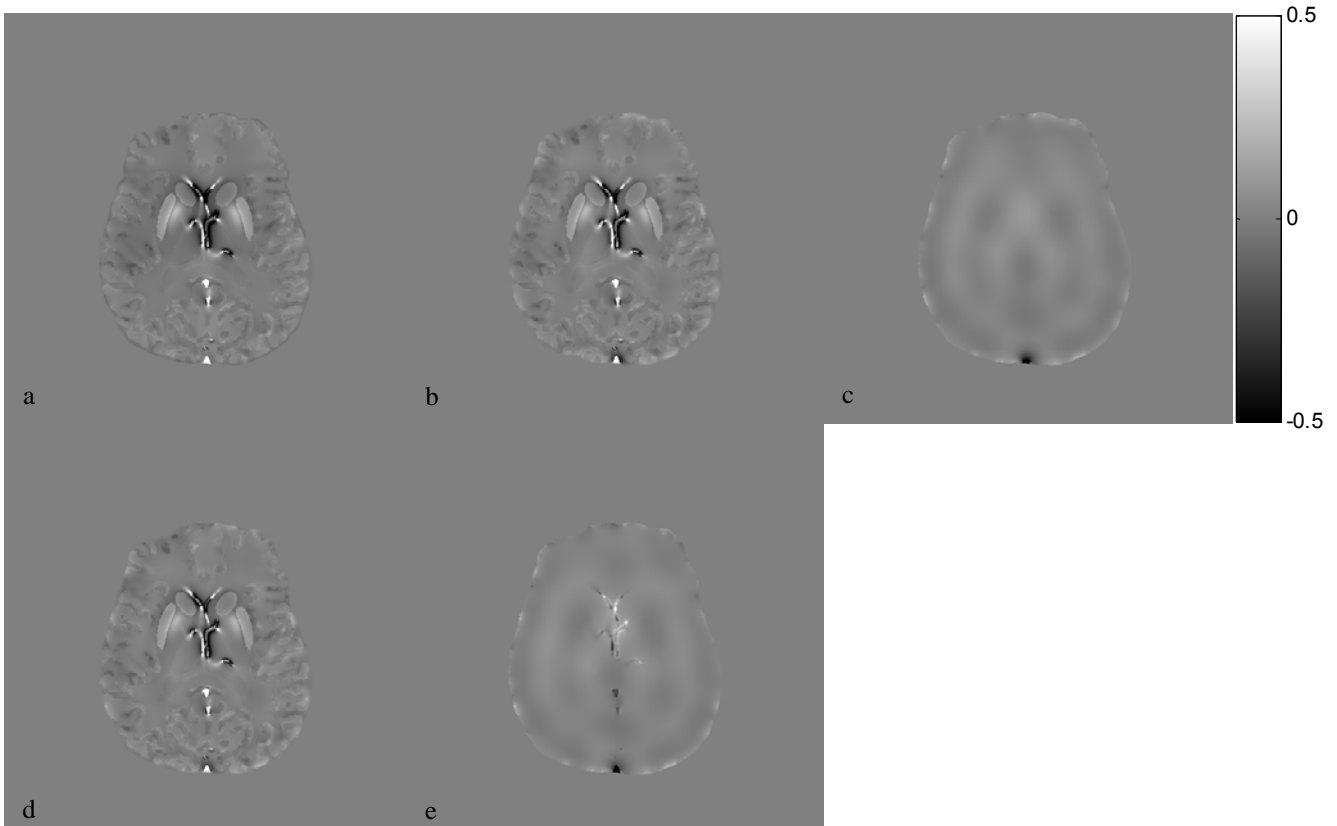


Figure 30: (a) The simulated phase image. (b) Phase image generated using the discrete operator (c) The resulting image of (b) subtracted from (a). (d) Phase image generated using the continuous operator. (e) The resulting image of (d) subtracted from (a).

d) Discussion

The Laplacian of phase can be calculated using the discrete Laplacian kernel and phase differences between pixels, or using the continuous Laplacian operator based on sine and cosine functions and Fourier transforms. In recent studies, we see a mixture of these two methods. For example, Schofield and Zhu [2003] used the continuous method for phase unwrapping. They claim that using the Fourier transform property to calculate the derivatives and using the sine and cosine functions help to avoid noise amplifications. In this study, random noise was not considered. Hence the propagation of noise was not fully evaluated. Since for phase unwrapping, it is the number of multiples of 2π that need to be determined, rather than the local phase information, it might not have much error associated with veins, as long as the absolute value of Laplacian of the local phase information does not exceed π (if it exceeds, the number of multiples of 2π may not be accurately determined). However, if the Laplacian is directly used in phase image processing, the discrete Laplacian operator should still be used. Phase images processed using the continuous operator may lead to an additional 10% error in our estimated susceptibility. Given the fact that MRI images are discrete signal, it is natural and more consistent to use the discrete forms.

It should also be noted that, once the Laplacian kernel is directly used in SHARP, it is equivalent to a kernel size of 1 pixel. This creates other problems related to the deconvolution step in SHARP, and will lead to larger errors in the processed phase images. Generally speaking, SHARP works best with filter sizes of 6-10 pixels, as shown in previous results.

KEY RESEARCH ACCOMPLISHMENTS

The following list of key research accomplishments is based on the “Statement of Work” described in our funded grant. In this first year,

- We have simulated a numerical/digital brain model through forward simulations with known magnetic susceptibility values assigned to 11 tissues inside the brain. This simulation has included the partial volume effect, Gibbs ringing, and tissue spin densities in magnitude MR images.
- We have built several 4-straw or 3-straw agar gel phantoms with different concentrations of nanoparticles and gadolinium mixed with distilled water and/or gelatin in straws. Different diameters of straws were tried.
- We have imaged the nanoparticle and gadolinium phantoms at two different orientations with an 11-echo susceptibility weighted imaging (SWI) sequence and a 14-echo spin echo sequence on our 3T MRI machine. The two different orientations include the cases when straws are parallel and perpendicular to the main field.
- We have built the SHARP program originally developed by Schweser et al. [2011].
- We have polished the high-pass filter program and the quadratic fit program for the background phase removal from MR images.
- We have built our own algorithm to remove the background phase.
- We have found that we can relatively easy to quantify susceptibility from larger straws with our CISSCO method applied to MR images. We can also quantify susceptibility with CISSCO from smaller straws with larger uncertainties plus the wall effect. Thus we have decided to use straws with diameters of roughly 6.3 mm and to prepare solutions of each material with the following targeted magnetic susceptibility values: 2 ppm, 1 ppm, 0.5 ppm, and 0.25 ppm in SI system.
- We have applied SHARP, high-pass filter, quadratic fit, and our own algorithm individually to SWI images for removing the background fields. After each of those procedures, we have quantified the susceptibility of each straw from at least 4 echoes from SWI. We have compared results between those methods.
- We have measured the concentrations of the aforementioned nanoparticle and gadolinium solutions with ICP-AES (inductively coupled plasma atomic emission spectroscopy).
- We have quantified relaxation rates R_2 and R_2^* of each aforementioned concentration from MR images and have estimated its associated uncertainty. We have found that R_2 and R_2^* are about the same for gadolinium samples, but not the same for nanoparticle samples. Furthermore, R_2 and R_2^* values depend on whether gadolinium or nanoparticles are mixed with distilled water or with gelatin. While we believe that these results depend on the diffusion constants in water and gel, the ratios between the changes of R_2 or R_2^* of substances in water and in gel are consistently different. We thus conclude that R_2 and R_2^* are not reliable measurements for magnetic susceptibility of substances. Nonetheless, quantified susceptibility values agree well with each other within uncertainties for the same concentration of samples. Therefore, we have postponed the quantifications of R_2 or R_2^* for ferritin and calcium solutions.
- We have built two 4-straw agar gel phantoms with different concentrations of ferritin and calcium mixed with distilled water in straws.
- We have imaged the ferritin and calcium phantoms at two different orientations with an 11-echo SWI and a 14-echo spin echo sequence on our 3T MRI machine. The two different orientations include the cases when straws are parallel and perpendicular to the main field.
- We have quantified the susceptibility of each solution with CISSCO from at least 4 echo times, based on phase distributions outside each straw, with the applications of the high-pass filter and SHARP individually to remove the background field.
- We have also quantified the phase value inside each straw to examine whether these phase values agree with the susceptibility values quantified from our CISSCO method.
- We have found that phase values inside straws containing gadolinium, calcium, and ferritin are sometimes 10% deviated from the phase values calculated from the susceptibility values obtained from CISSCO.
- We have identified some basic issues in the SHARP method and have estimated its errors on our digital brain model. In fact, we have studied errors of quantified susceptibility values with SHARP, high-pass filter, and a variable high-pass filter on our numerical brain model.
- We continue to improve different methods/programs mentioned above, to develop our own susceptibility quantification method, and to compare results from different methods.

REPORTABLE OUTCOMES

Manuscripts, abstracts, or presentations with partial supports from this grant:

- W. Zheng, H. Nichol, S. Liu, Y.-C. N. Cheng, and E. M. Haacke, *Measuring iron in the brain using quantitative susceptibility mapping and X-ray fluorescence imaging*, NeuroImage, vol. 78, pp. 68-74, 2013.
- *Applications of Short Echo QSM*, a talk presented by E. M. Haacke in the Second QSM Workshop, Cornell University, Ithaca, New York, USA, July 26, 2013.
- *CISSCO Method for Measuring Susceptibility*, a talk presented by Y.-C. N. Cheng in the Second QSM Workshop, Cornell University, Ithaca, New York, USA, July 27, 2013.

Funding applied for based on work supported by this award:

- GE/NFL, Title: Accurate Magnetic Susceptibility and Volume Measurements with Error Analyses of Each Cerebral Microbleed and Tissue from MRI as Biomarkers in the Mild Traumatic Brain.

Employment or research opportunities applied for and/or received based on experience/training supported by this award:

- A graduate student in Physics, He Xie, has passed his Ph.D. prospectus examine in early September 2013 with some of the work described above. He is now a Ph.D. candidate.

CONCLUSION

We have accomplished most tasks provided in the Statement of Work. The above list of key accomplishments can already serve as the conclusion. In brief, our CISSCO method can accurately quantify the magnetic moment of a cylindrical object. When the cross section of the object is known, we can calculate the magnetic susceptibility. The accuracy achieved by CISSCO on the object with a diameter of a few pixels cannot be achieved by any other susceptibility quantification methods. In addition, we have studied the effects due to four background phase removal methods. Currently we have found the inconsistencies between phase values inside a straw and expected values estimated from quantified susceptibilities. We have shown that the issues can be due to the use of the high-pass filter and we further suspect that the issues can also be due to the use of SHARP (one of the background phase removal method). We will conduct a few more simulations and resolve this issue. Furthermore, we have found that the relaxation rate (R_2 or R_2^*) measurements are not consistent and depending on the solid or liquid state of a sample, the relaxation rates can be different, even for the same concentration of a material. This will be important for the MR community to be aware. We will also need to spend time to write and publish our presented work above.

Our numerical brain model will continue to be a tool for tests. In the next annual period, as listed in the Statement of Work, we will use or build molds to prepare samples with arbitrary geometries and quantify the susceptibility of each sample. We will also need to improve our own background phase removal method to a 3D method. In addition to existing susceptibility quantification methods, we also want to develop a better method. These will be challenging tasks in this coming annual period.

REFERENCES

- Y.-C. N. Cheng, C.-Y. Hsieh, J. Neelavalli, and E. M. Haacke, *Quantifying effective magnetic moments of narrow cylindrical objects in MRI*, Physics in Medicine and Biology, vol. 54, pp. 7025-7044, 2009.
- Y.-C. N. Cheng, J. Neelavalli, and E. M. Haacke, *Limitations of calculating field distributions and magnetic susceptibilities in MRI using a Fourier based method*, Physics in Medicine and Biology, vol. 54, pp. 1169-1189, 2009b.
- P. Gillis, A. Roch, and R. A. Brooks, *Corrected equations for susceptibility-induced T2-shortening*, Journal of Magnetic Resonance, vol. 137, pp. 402-407, 1999.
- E. M. Haacke, R. W. Brown, M. R. Thompson and, R. Venkatesan, Magnetic Resonance Imaging: Physical Principles and Sequence Design, New York: Wiley, 1999.
- E. M. Haacke, Y.-C. N. Cheng, M. J. House, Q. Liu, J. Neelavalli, R. J. Ogg, A. Khan, M. Ayaz, W. Kirsch, and A. Obenaus, *Imaging iron stores in the brain using magnetic resonance imaging*, Magnetic Resonance Imaging, vol. 23, no. 1, pp. 1-25, 2005.
- E. M. Haacke, J. Tang, J. Neelavalli, and Y.-C. N. Cheng, *Susceptibility mapping as a means to visualize veins and quantify oxygen saturation*, Journal of Magnetic Resonance Imaging, vol. 32, pp. 663-676, 2010.
- S. H. Koenig and K. E. Kellar, *Theory of 1/T1 and 1/T2 NMRD profiles of solutions of magnetic nanoparticles*, Magnetic Resonance in Medicine, vol. 34, pp. 227-233, 1995.
- M. A. Schofield and Y. Zhu, *Fast phase unwrapping algorithm for interferometric applications*, Optics Letters, vol. 28, no. 14, pp. 1194-1196, 2003.
- F. Schweser, A. Deistung, B. W. Lehr, and J. R. Reichenbach, *Quantitative imaging of intrinsic magnetic tissue properties using MRI signal phase: An approach to in vivo brain iron metabolism?*, NeuroImage, vol. 54, pp. 2789-2807, 2011.
- Y. Shen, Y.-C. N. Cheng, G. Lawes, J. Neelavalli, C. Sudakar, R. Tackett, H. P. Ramnath, and E. M. Haacke, *Quantifying magnetic nanoparticles in non-steady flow by MRI*, Magnetic Resonance Materials in Biology, Physics, and Medicine, vol. 21, no. 5, pp. 345-356, 2008.
- R. M. Weisskoff and S. Kiihne, *MRI susceptometry: image-based measurement of absolute susceptibility of MR contrast agent and human blood*, Magnetic Resonance in Medicine, vol. 24, pp. 375-383, 1992.
- D. A. Yablonskiy and E. M. Haacke, *Theory of NMR signal behavior in magnetically inhomogeneous tissues: the static dephasing regime*, Magnetic Resonance in Medicine, vol. 32, pp. 749-763, 1994.
- W. Zheng, H. Nichol, S. Liu, Y.-C. N. Cheng, and E. M. Haacke, *Measuring iron in the brain using quantitative susceptibility mapping and X-ray fluorescence imaging*, NeuroImage, vol. 78, pp. 68-74, 2013.

APPENDICES

The paper by Zheng et al. is attached.



Measuring iron in the brain using quantitative susceptibility mapping and X-ray fluorescence imaging

Weili Zheng^a, Helen Nichol^b, Saifeng Liu^c, Yu-Chung N. Cheng^a, E. Mark Haacke^{a,c,*}

^a HUH-MR Research/Radiology, Wayne State University, Detroit, MI, USA

^b Department of Anatomy & Cell Biology, University of Saskatchewan, Saskatoon, SK, Canada

^c School of Biomedical Engineering, McMaster University, Hamilton, Ontario, Canada

ARTICLE INFO

Article history:

Accepted 3 April 2013

Available online 13 April 2013

Keywords:

Brain iron

Ferritin

Quantitative susceptibility mapping (QSM)

X-ray fluorescence imaging (XRF)

ABSTRACT

Measuring iron content in the brain has important implications for a number of neurodegenerative diseases. Quantitative susceptibility mapping (QSM), derived from magnetic resonance images, has been used to measure total iron content in vivo and in post mortem brain. In this paper, we show how magnetic susceptibility from QSM correlates with total iron content measured by X-ray fluorescence (XRF) imaging and by inductively coupled plasma mass spectrometry (ICPMS). The relationship between susceptibility and ferritin iron was estimated at 1.10 ± 0.08 ppb susceptibility per μg iron/g wet tissue, similar to that of iron in fixed (frozen/thawed) cadaveric brain and previously published data from unfixed brains. We conclude that magnetic susceptibility can provide a direct and reliable quantitative measurement of iron content and that it can be used clinically at least in regions with high iron content.

© 2013 Elsevier Inc. All rights reserved.

Introduction

Iron is an important endogenous biomarker for many neurological diseases and normal aging (Haacke et al., 2005; Schenck and Zimmerman, 2004). Previous histological work has shown that focally elevated iron deposition is associated with various neurological and psychiatric disorders, including multiple sclerosis (MS) (LeVine, 1997), Alzheimer's disease (Bouras et al., 1997; Hallgren and Sourander, 1960; LeVine, 1997), Huntington's disease (Chen et al., 1993; Dexter et al., 1991) and Parkinson's disease (Chen et al., 1993; Dexter et al., 1991). Increased iron accumulation has been detected in chronic hemorrhage, MS lesions, cerebral infarction, anemia, thalassemia, hemochromatosis, and NBIA (neurodegeneration with brain iron accumulation) (Haacke et al., 2005). An in vivo non-invasive and quantitative estimation of non-heme iron deposition (predominantly ferritin) is essential to understand the cause of iron accumulation and its distribution patterns as well as its physiological role in any given disease (Bartzokis et al., 2007; Gerlach et al., 1994; Ke and Qian, 2003).

A variety of methods have been used in the past to quantify iron using magnetic resonance imaging (MRI) (Haacke et al., 2005). The standard workhorses in this area are T2 (House et al., 2007; Jensen et al., 2010; Mitsumori et al., 2012) and T2* (or $R2^* = 1/T2^*$) imaging methods that create T2* or R2* maps derived from multi-echo gradient (recalled) echo magnitude images. The latter are particularly useful since gradient echo sequences are very sensitive to the local susceptibility induced

magnetic field inhomogeneity due to iron (Bartzokis et al., 1993; Haacke et al., 1989, 2005; Ordidge et al., 1994; Peters et al., 2007; Reichenbach et al., 1997). Further, T2* or R2* maps provide an important contrast mechanism to investigate brain tissue microstructure and to detect abnormal levels of brain iron (Bartzokis et al., 2007; Bouras et al., 1997; Chen et al., 1993; Dexter et al., 1991; Haacke et al., 2005, 2009; Hallgren and Sourander, 1960; LeVine, 1997; Wallis et al., 2008).

In this paper, we focus on susceptibility measurements from phase images. Phase has been used as a means to measure iron content (Haacke et al., 2007). However, phase is dependent on the geometry of the object and so it can be misinterpreted. The solution lies in using a susceptibility map reconstructed from the phase information. In theory, this approach is independent of field strength, echo time, the object's relative orientation to the main field and the object's shape (Cheng et al., 2009b; de Rochefort et al., 2010; Haacke et al., 2010; Kressler et al., 2010; Li et al., 2011; Liu et al., 2009; Marques and Bowtell, 2005; Schweser et al., 2011; Shmueli et al., 2009; Wharton and Bowtell, 2010; Yao et al., 2009). Recent work has suggested that susceptibility changes in the basal ganglia, thalamus and other deep gray matter nuclei have better correlation with iron concentration than phase information (Bilgic et al., 2012; Fukunaga et al., 2010; Langkammer et al., 2012b; Schweser et al., 2011, 2012; Shmueli et al., 2009; Wharton and Bowtell, 2010; Yao et al., 2009) and, therefore, quantitative susceptibility mapping (QSM) may provide a good means to study tissue iron content.

Currently, the neuroscience community relies upon the 50 year old data on iron in cadaveric brains published by Hallgren and Sourander (Hallgren and Sourander, 1958). Total iron in cadaveric brain has been measured using synchrotron X-ray fluorescence (XRF) iron mapping

* Corresponding author at: HUH-MR Research/Radiology, Wayne State University, 3990 John R Street, Detroit, MI 48201, USA. Fax: +1 313 745 9182.

E-mail address: nmrimging@aol.com (E.M. Haacke).

Table 1
Methodology and data processing.

	ICPMS	XRF	SWI Background phase removal	QSM
Ferritin samples	✓	✓	Quadratic fitting	Forward fitting
Cadaveric brain		✓	SHARP	Truncated k-space division (Haacke et al., 2010)

(Hopp et al., 2010; Zheng et al., 2012), proton-induced X-ray emission mapping (Butz et al., 2000), inductively coupled plasma mass spectrometry (ICPMS) measurements (Langkammer et al., 2010, 2012a) and atomic absorption spectrometry measurements (House et al., 2007). Among these, the first two techniques can provide a voxel by voxel quantification of iron content which can then be compared with MR iron quantification.

In this paper, our goal is to develop an absolute quantification scale by separating the iron induced susceptibility change from other potential sources by comparing ferritin-gelatin phantoms with quantified XRF iron maps of basal ganglia from cadaver brains and ICPMS iron values.

Materials and methods

Preparation of ferritin phantoms

Horse spleen ferritin (Ref. F4503, Sigma-Aldrich, USA) was used to prepare ferritin-gelatin phantoms. The iron concentration as determined by the supplier using ICPMS was 7.13 ± 0.15 mg/ml. The ferritin solution was first diluted by adding 4 ml of original solution with 16ml warm 7% gelatin resulting in a stock solution with iron concentration of about 1426 ± 30 μ g/ml. This stock solution was serially diluted six times in warm gelatin by a factor of 2 each time. The ferritin-doped gelatin solutions as well as pure gelatin were loaded into straws and then embedded in a pure gelatin matrix. Total iron was measured in aliquots of the ferritin-doped gelatin by XRF and ICPMS. See the detailed scheme of the experiment in Table 1.

Rapid scanning X-ray fluorescence (RS-XRF)

All XRF measurements were conducted at the Stanford Synchrotron Radiation Lightsource (SSRL). RS-XRF images of ferritin phantoms and cadaveric brain were acquired at wiggler beam line 10–2 at SSRL. The samples were mounted onto a set of motorized stages oriented at 45° to the incident beam. The incident beam (12 keV) passing through a tantalum aperture produced a $100 \mu\text{m} \times 100 \mu\text{m}$ spot on the sample which was raster-scanned in the beam using a dwell time of 15 ms/point. Fluorescent energy windows were centered for Fe (6.21–6.70 keV) as well as all other biologically interesting elements, scatter and total incoming counts. Elements were quantified in μg iron/g wet tissue by comparison of signal strength with XRF calibration standards ($\pm 5\%$ uncertainty) (Micromatter, Vancouver, BC, Canada) according to Hopp and colleagues (Hopp et al., 2010) using Sam's Microanalysis kit (Webb, 2010). An area of the ferritin-doped gelatin block was mapped and average counts were compared with XRF calibration standards.

Inductively coupled plasma mass spectrometry

To confirm the total iron content of the ferritin phantoms, 5 ml samples were taken from the straws after MR imaging and the iron content was determined by ICPMS using an ELAN 9000 system (PerkinElmer, Waltham, MA, USA) (American Environmental Testing

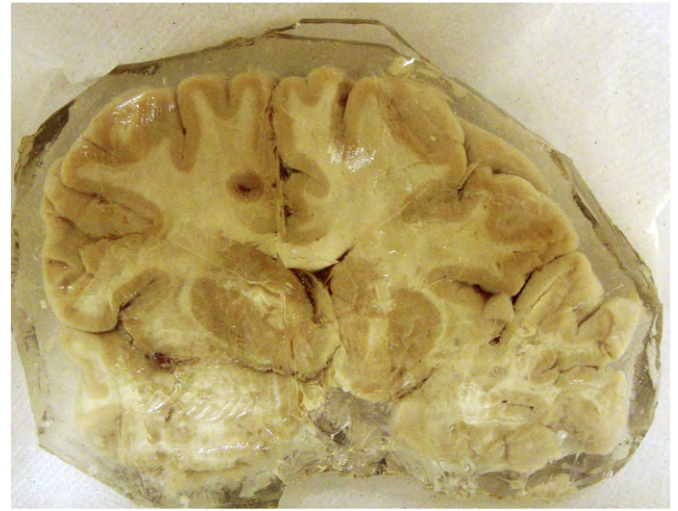


Fig. 1. Photograph of the cadaveric brain sample in gelatin.

Laboratory Inc., California). The samples were diluted to the range acceptable for ICPMS via serial dilutions.

Preparation of the cadaveric brain sample

One frozen coronal section (96 mm long \times 132 mm wide \times 5 mm thick) of human cadaveric multiple sclerosis (MS) brain (MS 3852) (see Fig. 1) was obtained from the Human Brain and Spinal Fluid Resource Center, Los Angeles, CA, under the University of Saskatchewan ethics approval BioREB 06-250. Coronal sections showed extensive irregular demyelination throughout the brainstem. There were also a few small scattered demyelinating periventricular foci (bilateral). The surface of the sample (a 5 mm thick section) showed patchy areas of slight rarefaction without significant axonal loss or change in oligodendrocyte density. There were varying degrees of associated gliosis. The areas of rarefaction were associated with extensive demyelination. To reduce storage artifacts such as leaching of metals, fresh autopsy brain was flash frozen and the slices were shipped on dry ice and stored frozen until they were thawed by immersion in buffered formalin. After 6 h of fixation, the brain slice was drained and sealed in plastic prior to initial synchrotron imaging of the surface of the slice. To resolve regions of interest, the slices were embedded in gelatin for MR imaging. The brain hemispheres were sectioned to expose the region of interest and then the slice was sealed in metal-free thin polypropylene film. RS-XRF images were acquired and quantified at SSRL (see the detailed scheme of the experiment in Table 1).

MR imaging and image processing

Imaging and phase processing of ferritin samples

MR data of ferritin samples were collected on a 3 T Siemens Verio system using a multi-echo susceptibility weighted imaging (SWI) sequence with 11 echoes (TR = 40 ms, FA = 15°). The resolution was $1 \text{ mm} \times 1 \text{ mm} \times 1 \text{ mm}$ with a matrix of $256 \times 256 \times 128$. The shortest echo time was 5 ms with a 2.39 ms increment for the other 10 echoes. Magnitude and phase images were reconstructed from the raw data for each individual and combined channel. The geometry of the ferritin samples was segmented from multi-echo spin echo images (TR = 2000 ms, resolution $0.22 \text{ mm} \times 0.22 \text{ mm} \times 3 \text{ mm}$).

In order to reconstruct a susceptibility map, a pristine phase map was required. That is, the phase was unwrapped and all spurious phase information was removed. Phase images (TE = 21.73 ms) were unwrapped using Prelude in FSL (Jenkinson, 2003). To remove

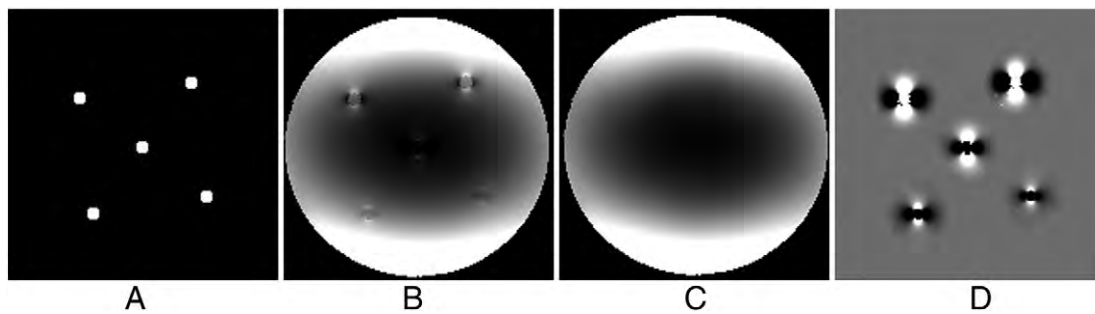


Fig. 2. Removing the background phase (TE = 21.73 ms). A) Geometry of the straws segmented from the spin echo images. B) Original phase. C) Background phase after extrapolation of magnetic fields into the straw regions. D) Subtraction of C from B to reveal pristine dipole effects due to the iron in the straws.

the low spatial frequency background field effects, phase from regions outside the straws were chosen, where there were minimal remnant dipole effects. First, a circular mask with a radius three times that of the straw was defined and centered on each straw and all the information inside this mask was removed from the images. The remaining signal was fit with a quadratic function and extrapolated back into the masked region. Then the estimated dipole phase was obtained by subtracting this modified background phase from the original phase. The susceptibility inside each of the ferritin straws was assumed to be uniform and was estimated using a least squares fitting of the forward simulated dipole phase with the estimated phase (Neelavalli et al., 2009). All the steps were performed in MATLAB R2009a. The results of each step are shown in Fig. 2.

Imaging and image processing of cadaveric brain

MR images were collected on a 3 T Siemens Verio system using the same 11 echo SWI sequence but with different imaging parameters. The coronal images were acquired with a resolution 0.5 mm × 0.5 mm in phase encoding and readout direction and 0.7 mm in the slice select direction with a readout bandwidth of 465 Hz/pixel, a field-of-view of 256 mm × 192 mm with Nx = 512, Ny = 384 and Nz = 40. The shortest echo time was 5.68 ms with a 2.57 ms increment for the other 10 echoes. MR phase images (TE = 8.25 ms) were first unwrapped using Prelude in FSL (Jenkinson, 2003) and then the background phase was removed using TSVD-SHARP (Schweser et al., 2011) with a kernel size of 5 mm. An initial estimation of the susceptibility distribution was obtained using truncated k-space division, with a threshold value of 0.1. Due to the presence of some air bubbles near the brain tissue, the streaking artifacts would mask several important regions in the susceptibility map. Thus, the air bubbles were first extracted from the susceptibility map by setting a threshold, since air has a much higher susceptibility relative to water than that of brain tissue. The extracted susceptibility maps of the air bubbles were used to predict their induced field variation through a forward field calculation. Finally, the predicted fields induced by the air bubbles were removed from the SHARP (Schweser et al., 2012) processed field map. The central region of these air bubbles in phase images was set to be zero, in order to reduce the streaking artifacts caused by the noise inside the bubble. This newly processed field map was used to generate the

final susceptibility maps, using a truncated k-space division with a threshold of 0.1 (Haacke et al., 2010) via SPIN (Signal Processing in NMR, Detroit, MI, USA) software.

Results

Correlation between susceptibility and ferritin iron content

The susceptibilities (TE = 21.73 ms) of the five empty straws embedded in gelatin were estimated at $(9.46 \pm 0.015; 9.64 \pm 0.015; 9.46 \pm 0.016; 9.65 \pm 0.013; 9.46 \pm 0.015)$ ppm. Assuming that the susceptibility difference between the air and gel is 9.4 ppm (Cheng et al., 2009a), the total susceptibility measurement including the background removal, straw geometry segmentation error and least squares fitting had a bias of 1.42%.

The measured susceptibilities (TE = 21.73 ms) and iron concentrations of the six ferritin samples are listed in Table 2. The dipolar phase pattern outside the straw from the sample with the lowest iron concentration ($39 \pm 6 \mu\text{g Fe/ml}$) had its sign reversed compared with other samples. This sample shows a negative susceptibility of -14ppb when using the forward fitting approach. One possible explanation for this could be a small baseline shift coming from an imperfect background removal. Since the iron concentration range that can be measured with XRF is broad, there was no need for dilution. In contrast, ICPMS requires dilution of samples to make iron concentration in the proper range for analysis. The results in Table 2 show that the iron content measured by two approaches (XRF and ICPMS) was essentially the same. The correlation slopes in Fig. 3 obtained from ICPMS ($1.11 \pm 0.06 \text{ ppb per } \mu\text{g iron/ml}$) and XRF imaging ($1.10 \pm 0.08 \text{ ppb per } \mu\text{g iron/ml}$) were close and both were less than the theoretical estimation of $1.27\text{ppb per } \mu\text{g iron/ml}$ from Schenck (1992).

Correlation between susceptibility and iron in cadaveric brain

In order to correlate the susceptibility and XRF iron maps, images from both methods were co-registered (Fig. 4). ROIs marked in each image were used for a voxel by voxel comparison of susceptibility and iron measurements (Table 3). At TE = 8.25 ms, the correlation equations were found to be $Y = 0.80(\pm 0.01)$ (ppb susceptibility

Table 2
Susceptibilities of ferritin phantoms as quantified from SWI phase data (TE = 21.73 ms) and iron concentrations measured by XRF and ICPMS. Data are shown as mean \pm one standard deviation.

	Sample no. 1	Sample no. 2	Sample no. 3	Sample no. 4	Sample no. 5	Sample no. 6	Gelatin solution (7%)
Susceptibility (ppb) (N = 19,205)	840 ± 2.4	428 ± 1.3	271 ± 0.9	101 ± 0.4	39 ± 0.3	-14 ± 0.2	N.A. for forward fitting
XRF iron concentration ($\mu\text{g/ml}$) (N = 961)	790 ± 94	395 ± 44	229 ± 32	110 ± 27	77 ± 16	(Not available)	(Not available)
ICPMS iron concentration ($\mu\text{g/ml}$)	772 ± 115	448 ± 67	240 ± 36	127 ± 19	66 ± 10	39 ± 6	0.23 ± 0.11

Standard deviation includes the spatial distribution variation in the straws.

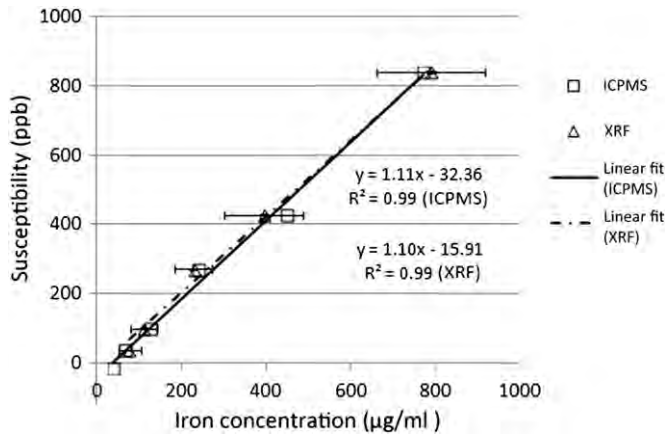


Fig. 3. Correlation between susceptibility measured by MRI and total iron measured by ICPMS and XRF for ferritin phantoms.

per μg iron/g wet tissue) $\times X$ (μg iron/g wet tissue) + 10.87(± 2.9) (ppb susceptibility) and $Y = 0.79(\pm 0.02) \times X - 3.66(\pm 4.2)$ (ppb susceptibility) for left and right hemisphere, respectively, as shown in Fig. 5 (A, B). The phase images at TE = 21.1 ms were also

processed, the fitted equations were $Y = 0.78(\pm 0.02) \times X - 4.36(\pm 4)$ (ppb susceptibility) and $Y = 0.79(\pm 0.01) \times X - 5.22(\pm 2.8)$ (ppb susceptibility) for left and right hemispheres respectively. The slopes (0.80 and 0.79 ppb susceptibility per μg iron/g wet tissue) determined from the TE = 21.1 ms data were similar to those from TE = 8.25 ms (0.78 and 0.79). Although phase is clearly modified as a function of echo time, tissue susceptibility change is expected to be and here is shown to be independent of echo time (Haacke et al., 2010). The estimated susceptibility based on our simulation of the inverse process using the structures of a similar size showed an underestimate or bias of -14% .

Discussion

Using ferritin phantoms and a cadaveric brain sample, we have found that the susceptibility correlates reasonably well with the iron measured by XRF and/or ICPMS (Fig. 3). The cadaveric brain used in the study was from a person with multiple sclerosis. It is commonly assumed that the iron in normal and pathological MS brains is predominantly stored in the form of ferritin. As long as this assumption holds, the MS pathology will not affect the susceptibility/iron correlation slope. Our correlation of iron content with susceptibility for cadaveric brains (Fig. 5) was comparable with that obtained by Langkammer et al. (2012b). This is expected since we used SHARP with the same

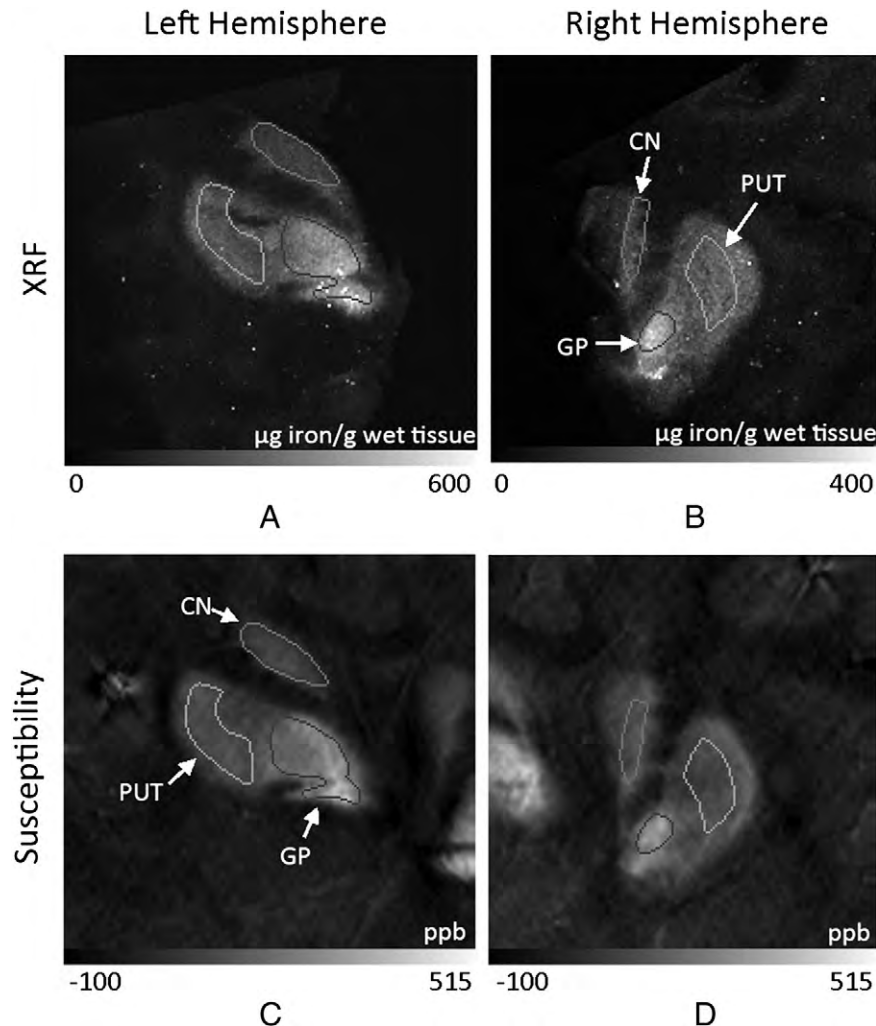


Fig. 4. Iron quantified from XRF Fe mapping (A, B) for left and right hemispheres; putative iron quantified as susceptibility (TE = 8.25 ms) (C, D). Images are co-registered and the ROIs used for a pixel by pixel correlation are outlined in both images. CN: caudate nucleus. PUT: putamen. GP: globus pallidus. ROIs were defined by excluding the edges in the map for each structure.

Table 3

Average susceptibility of a cadaveric brain as quantified from SWI phase data (TE = 8.25 ms) and Fe measured using XRF imaging. ROIs are defined in Fig. 4. Data are shown as mean \pm one standard deviation.

	CN (left)	PUT (left)	GP (left)	CN (right)	PUT (right)	GP (right)
Susceptibility (ppb)	111 \pm 25	152 \pm 18	273 \pm 73	105 \pm 31	121 \pm 24	242 \pm 40
Iron estimated by XRF ($\mu\text{g/g}$ wet tissue)	153 \pm 28	210 \pm 35	338 \pm 73	135 \pm 28	179 \pm 26	277 \pm 40

Mean is estimated as the average within the ROI. Standard deviation includes the spatial distribution variation within the ROI.

parameters to remove the background fields. The SWIM approach used in this paper underestimates the susceptibility by 14% for deep gray matter structures according to our simulations. The homogeneity-enabled incremental dipole inversion (HEIDI) method used by Langkammer et al. (2012b) underestimates the susceptibility by about 7% (Langkammer et al., 2012b; Schweser et al., 2012). Our slope ($0.8 / (1-14\%) \approx 0.93$) is close to that in Langkammer et al. (2012b) ($0.89 / (1-7\%) \approx 0.957$) for deep gray matter when these biases are accounted for. Since the cadaveric brain in our experiment was formalin fixed and those in Langkammer et al. (2012b) were unfixed, this suggests that fixation may not change tissue susceptibility in deep gray matter.

However, the slope of 0.59 ppb susceptibility per μg iron/g wet tissue obtained from our in vivo data (Haacke, 2012) and other single orientation results that used Hallgren and Sourander's equation as the iron baseline (Shmueli et al., 2009; Wharton and Bowtell, 2010) was smaller than the 0.8 ppb susceptibility per μg iron/g wet tissue obtained from our cadaveric brain data, even though they were processed with the same methods. Thus, there appears to be a difference between in vivo and ex vivo susceptibilities and their correlation with iron. The reason for this is unclear but could be due to the freezing and fixation process which could affect local susceptibilities of the tissue.

Formalin fixation might change MR signal but previous work on myelin susceptibility (Lee et al., 2012; Liu et al., 2011) demonstrated that the effect of formalin fixation on the susceptibility changes due to myelin was subtle. The similar iron/susceptibility slopes of fixed brain in our work and of the unfixed brains in the work of Langkammer and colleagues (Langkammer et al., 2012b) further supports the view that formalin fixation has negligible effect on susceptibility. The effects of fixation on R2 and thus R2* values, however, are known to be substantial (Dawe et al., 2009; Lee et al., 2012; Pfefferbaum et al., 2004; Schmierer et al., 2008) and are beyond the scope of this paper.

The susceptibility/iron correlation slopes obtained from cadaveric and in vivo brains in Table 4 are generally smaller than the theoretical slope of 1.32 ppb susceptibility per μg iron/g wet tissue except for the slope obtained with myelin correction in Schweser et al. (2011). One possible reason for the smaller slope from the in vivo human brains is that there are still some forms of iron that are MR invisible although these may be in other species that are known to be present at low levels (Hopp et al., 2010). A second explanation for smaller slopes seen in our work (Haacke, 2012) and other work (Shmueli et al., 2009; Wharton and Bowtell, 2010) is that Hallgren and Sourander's measurements of total iron (Hallgren and Sourander, 1958) may not be accurate. Third, susceptibility mapping is known to have a bias and leads to a smaller slope, but this bias can be potentially corrected (J. Liu et al., 2012; T. Liu et al., 2012; Schweser et al., 2012; Wharton and Bowtell, 2010). Other possible factors that have been explored include contributions of myelin (Duyn et al., 2007; Liu et al., 2011; Ogg et al., 1999), chemical exchange between water and macromolecular protons (Luo et al., 2010; Shmueli et al., 2011; Zhong et al., 2008) and microstructure orientation (He and Yablonskiy, 2009; Lee et al., 2010; Liu, 2010). Indeed, it could well be a combination of all these sources that lead to different measurements of iron in vivo and ex vivo. Despite these imperfections, the slopes for susceptibility versus iron content are generally consistent between both ex vivo studies (this paper and Langkammer et al., 2012b) and in vivo studies using similar susceptibility mapping methods (see Table 4) (Haacke, 2012; Shmueli et al., 2009; Wharton and Bowtell, 2010).

Conclusion

Our results suggest that susceptibility changes from iron measured in ex vivo studies reasonably reflect iron content even for in vivo studies, although the predicted values may be underestimated. Our study further demonstrates that the correlation of susceptibility with iron is consistent with other results in the literature and is independent of echo time and orientation. Thus, susceptibility would appear to be a direct and reliable quantitative indication of iron, especially for brain

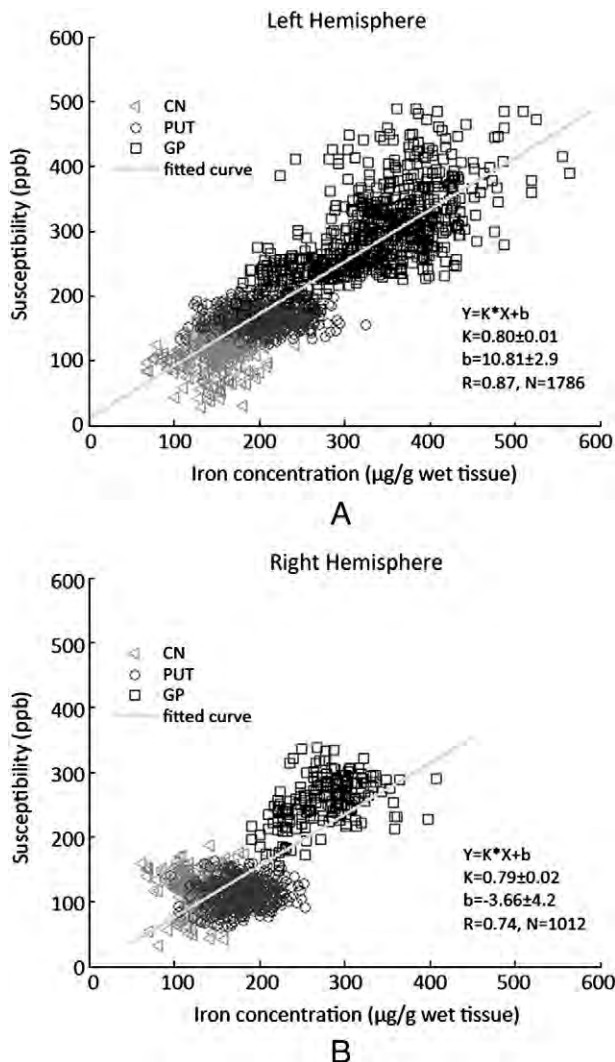


Fig. 5. Correlation between susceptibility and XRF iron measurements for all data points taken from each of the regions demarcated in Fig. 4. A: fitting for left hemisphere; B: fitting for right hemisphere.

Table 4
Correlation between susceptibility mapping and iron concentration.

Authors	Correlation slope ^a	Structures	Background removal	QSM method ^b	Myelin correction	Field (Tesla)	Sample	Iron
This paper	1.11	N.A.	Quadratic fitting	Forward fitting	N.A.	3 T	Ferritin	ICPMS
This paper	1.10	N.A.	Quadratic fitting	Forward fitting	N.A.	3 T	Ferritin	XRF
This paper	0.80	GP, PUT, CN	SHARP	TKD ¹ (SO)	No	3 T	MS cadaveric brain (fixed)	XRF
Haacke (2012)	0.59	GP, PUT, CN	SHARP	TKD ¹ (SO)	No	3 T	In vivo brains	H&S ^c
Shmueli et al. (2009)	0.56	PUT, RN, SN	Polynomial fitting	TKD ² (SO)	No	7 T	In vivo brain	H&S
Wharton and Bowtell (2010)	0.75/0.6	GP, SN, RN, PUT, CN, TH, GM	Simulated geometric effect + fitting	TKD ³ (MO/SO)	No	7 T	In vivo brains	H&S
Langkammer et al. (2012a)	0.89	GP, PUT, CN, TH	SHARP	HEIDI (SO)	No	3 T	Unfixed cadaveric brains	ICPMS
Schweser et al. (2011)	1.30	GP, SN, DN, PUT, CN, TH, WM, GM	SHARP	MO regularization	Yes	3 T	In vivo brains	H&S

^a The unit of the slope for human brain is susceptibility/μg iron/g wet tissue ($\rho = 1.04\text{g/ml}$ at 36.5°C); the unit of the slope for the ferritin solution is ppb susceptibility/μg iron/ml and the corresponding theoretical value is 1.27.

^b SO: single orientation; MO: multiple orientation; TKD: thresholded k-space division. TKD¹: Haacke et al., 2010; TKD²: Shmueli et al., 2009; TKD³: (Wharton and Bowtell, 2010).

^c H&S: (Hallgren and Sourander, 1958).

regions with high iron content. Susceptibility mapping provides a reliable tool for clinical investigations of iron that could be used to study changes in iron over time or within a given age-matched population.

Acknowledgments

This work is supported by the Canadian Institutes of Health Research (CIHR)/Heart and Stroke Foundation of Canada (HSFC) Synchrotron Medical Imaging Team Grant #CIF 99472.

This work was supported in part by the Telemedicine and Advanced Technology Research Center (TATRC) at the U.S. Army Medical Research and Materiel Command (USAMRMC) through award W81XWH-12-1-0522. The views, opinions and/or findings contained in this report are those of the author(s) and should not be construed as an official government position, policy or decision unless so designated by other documentation.

Portions of this research were carried out at the Stanford Synchrotron Radiation Lightsources, a Directorate of SLAC National Accelerator Laboratory and an Office of Science User Facility operated for the U.S. Department of Energy Office of Science by Stanford University. The SSRL Structural Molecular Biology Program is supported by the DOE Office of Biological and Environmental Research, and by the National Institutes of Health, National Center for Research Resources, Biomedical Technology Program (P41RR001209).

The authors would like to thank Sam Webb at the Stanford Synchrotron Radiation Lightsources and Angela Auriat at the Dept. of Neurosurgery, Stanford University for their help in collecting XRF data. We thank Zahid Latif, Yang Xuan, Yimin Shen for their assistance with the MR protocols, and Dr. Wei Feng and Dr. Jaladhar Neelavalli for their help on susceptibility mapping. The authors would also like to thank Dr. Karin Shmueli at NINDS, National Institute of Health for her valuable discussions of the literature.

Conflict of interest

The authors have no conflicts of interest.

References

- Bartzokis, G., Aravagiri, M., Oldendorf, W.H., Mintz, J., Marder, S.R., 1993. Field dependent transverse relaxation rate increase may be a specific measure of tissue iron stores. *Magn. Reson. Med.* 29, 459–464.
- Bartzokis, G., Tishler, T.A., Lu, P.H., Villablanca, P., Altschuler, L.L., Carter, M., Huang, D., Edwards, N., Mintz, J., 2007. Brain ferritin iron may influence age- and gender-related risks of neurodegeneration. *Neurobiol. Aging* 28, 414–423.
- Bilgic, B., Pfefferbaum, A., Rohlfing, T., Sullivan, E.V., Adalsteinsson, E., 2012. MRI estimates of brain iron concentration in normal aging using quantitative susceptibility mapping. *Neuroimage* 59, 2625–2635.
- Bouras, C., Giannakopoulos, P., Good, P.F., Hsu, A., Hof, P.R., Perl, D.P., 1997. A laser microprobe mass analysis of brain aluminum and iron in dementia pugilistica: comparison with Alzheimer's disease. *Eur. Neurol.* 38, 53–58.
- Butz, T., Flaggmeyer, R.-H., Heitmann, J., Jamieson, D.N., Legge, G.J.F., Lehmann, D., Reibetanz, U., Reinert, T., Saint, A., Spemann, D., Szymanski, R., Tröger, W., Vogt, J., Zhu, J., 2000. The Leipzig high-energy ion nanoprobe: a report on first results. *Nucl. Instrum. Methods Phys. Res. B* 161–163, 323–327.
- Chen, J.C., Hardy, P.A., Kucharczyk, W., Claiberg, M., Joshi, J.G., Vourlas, A., Dhar, M., Henkelman, R.M., 1993. MR of human postmortem brain tissue: correlative study between T2 and assays of iron and ferritin in Parkinson and Huntington disease. *Am. J. Neuroradiol.* 14, 275–281.
- Cheng, Y.C.N., Hsieh, C.Y., Neelavalli, J., Haacke, E.M., 2009a. Quantifying effective magnetic moments of narrow cylindrical objects in MRI. *Phys. Med. Biol.* 54, 7025–7044.
- Cheng, Y.C.N., Neelavalli, J., Haacke, E.M., 2009b. Limitations of calculating field distributions and magnetic susceptibilities in MRI using a Fourier based method. *Phys. Med. Biol.* 54, 1169–1189.
- Dawe, R.J., Bennett, D.A., Schneider, J.A., Vasireddi, S.K., Arfanakis, K., 2009. Postmortem MRI of human brain hemispheres: T2 relaxation times during formaldehyde fixation. *Magn. Reson. Med.* 61, 810–818.
- de Rochefort, L., Liu, T., Kressler, B., Liu, J., Spincemaille, P., Lebon, V., Wu, J.L., Wang, Y., 2010. Quantitative susceptibility map reconstruction from MR phase data using Bayesian regularization: validation and application to brain imaging. *Magn. Reson. Med.* 63, 194–206.
- Dexter, D.T., Carayon, A., Javoy-Agid, F., Agid, Y., Wells, F.R., Daniel, S.E., Lees, A.J., Jenner, P., Marsden, C.D., 1991. Alterations in the levels of iron, ferritin and other trace metals in Parkinson's disease and other neurodegenerative diseases affecting the basal ganglia. *Brain* 114, 1953–1975.
- Duyn, J.H., van Gelderen, P., Li, T.Q., de Zwart, J.A., Koretsky, A.P., Fukunaga, M., Li, T.Q., 2007. High-field MRI of brain cortical substructure based on signal phase. *Proc. Natl. Acad. Sci. U. S. A.* 104, 11796–11801.
- Fukunaga, M., Li, T.Q., van Gelderen, P., de Zwart, J.A., Shmueli, K., Yao, B., Lee, J., Maric, D., Aronova, M.A., Zhang, G., 2010. Layer-specific variation of iron content in cerebral cortex as a source of MRI contrast. *Proc. Natl. Acad. Sci. U. S. A.* 107 (8), 3834–3839.
- Gerlach, M., Ben-Shachar, D., Riederer, P., Youdim, M.B., 1994. Altered brain metabolism of iron as a cause of neurodegenerative diseases? *J. Neurochem.* 63, 793–807.
- Haacke, E.M., 2012. Quantitative measurements of iron. *Clinical Intensive Course, Advanced Neuroimaging 1*. Int. Soc. Mag. Reson. Med., 20 (Melbourne, Australia, http://www.ismrm.org/12/WK_Neuro1.htm).
- Haacke, E., Tkach, J., Parrish, T., 1989. Reducing T² dephasing in gradient field-echo imaging. *Radiology* 170, 457–462.
- Haacke, E.M., Cheng, N.Y., House, M.J., Liu, Q., Neelavalli, J., Ogg, R.J., Khan, A., Ayaz, M., Kirsch, W., Obenaus, A., 2005. Imaging iron stores in the brain using magnetic resonance imaging. *Magn. Reson. Imaging* 23, 1–25.
- Haacke, E.M., Ayaz, M., Khan, A., Manova, E.S., Krishnamurthy, B., Gollapalli, L., Ciulla, C., Kim, I., Petersen, F., Kirsch, W., 2007. Establishing a baseline phase behavior in magnetic resonance imaging to determine normal vs. abnormal iron content in the brain. *J. Magn. Reson. Imaging* 26, 256–264.
- Haacke, E.M., Makki, M., Ge, Y., Maheshwari, M., Sehgal, V., Hu, J., Selvan, M., Wu, Z., Latif, Z., Xuan, Y., Khan, O., Garbern, J., Grossman, R.I., 2009. Characterizing iron deposition in multiple sclerosis lesions using susceptibility weighted imaging. *J. Magn. Reson. Imaging* 29, 537–544.
- Haacke, E.M., Tang, J., Neelavalli, J., Cheng, Y.C.N., 2010. Susceptibility mapping as a means to visualize veins and quantify oxygen saturation. *J. Magn. Reson. Imaging* 32, 663–676.
- Hallgren, B., Sourander, P., 1958. The effect of age on the non-haemin iron in the human brain. *J. Neurochem.* 3, 41–51.
- Hallgren, B., Sourander, P., 1960. The non-haemin iron in the cerebral cortex in Alzheimer's disease. *J. Neurochem.* 5, 307–310.
- He, X., Yablonskiy, D.A., 2009. Biophysical mechanisms of phase contrast in gradient echo MRI. *Proc. Natl. Acad. Sci. U. S. A.* 106, 13558–13563.

- Hopp, K., Gh Popescu, B.F., McCrea, R.P.E., Harder, S.L., Robinson, C.A., Haacke, E.M., Rajput, A.H., Rajput, A., Nichol, H., 2010. Brain iron detected by SWI high pass filtered phase calibrated with synchrotron X-ray fluorescence. *J. Magn. Reson. Imaging* 31, 1346–1354.
- House, M.J., Pierre, T.G.S., Kowdley, K.V., Montine, T., Connor, J., Beard, J., Berger, J., Siddaiah, N., Shankland, E., Jin, L.W., 2007. Correlation of proton transverse relaxation rates (R2) with iron concentrations in postmortem brain tissue from Alzheimer's disease patients. *Magn. Reson. Med.* 57, 172–180.
- Jenkinson, M., 2003. A fast, automated, n-dimensional phase unwrapping algorithm. *Magn. Reson. Med.* 49, 193–197.
- Jensen, J.H., Tang, H., Tosti, C.L., Swaminathan, S.V., Nunez, A., Hultman, K., Szulc, K.U., Wu, E.X., Kim, D., Sheth, S., Brown, T.R., Brittenham, G.M., 2010. Separate MRI quantification of dispersed (ferritin-like) and aggregated (hemosiderin-like) storage iron. *Magn. Reson. Med.* 63, 1201–1209.
- Ke, Y., Qian, Z.M., 2003. Iron misregulation in the brain: a primary cause of neurodegenerative disorders. *Lancet Neurol.* 2, 246–253.
- Kressler, B., de Rochefort, L., Liu, T., Spincemaille, P., Jiang, Q., Wang, Y., 2010. Nonlinear regularization for per voxel estimation of magnetic susceptibility distributions from MRI field maps. *IEEE Trans. Med. Imaging* 29, 273–281.
- Langkammer, C., Krebs, N., Goessler, W., Scheurer, E., Ebner, F., Yen, K., Fazekas, F., Ropele, S., 2010. Quantitative MR imaging of brain iron: a postmortem validation study. *Radiology* 257, 455–462.
- Langkammer, C., Krebs, N., Goessler, W., Scheurer, E., Yen, K., Fazekas, F., Ropele, S., 2012a. Susceptibility induced gray-white matter MRI contrast in the human brain. *Neuroimage* 59, 1413–1419.
- Langkammer, C., Schweser, F., Krebs, N., Deistung, A., Goessler, W., Scheurer, E., Sommer, K., Reishofer, G., Yen, K., Fazekas, F., Ropele, S., Reichenbach, J.R., 2012b. Quantitative susceptibility mapping (QSM) as a means to measure brain iron? A post mortem validation study. *Neuroimage* 62, 1593–1599.
- Lee, J., Shmueli, K., Fukunaga, M., van Gelderen, P., Merkle, H., Silva, A.C., Duyn, J.H., 2010. Sensitivity of MRI resonance frequency to the orientation of brain tissue microstructure. *Proc. Natl. Acad. Sci. U. S. A.* 107, 5130–5135.
- Lee, J., Shmueli, K., Kang, B.-T., Yao, B., Fukunaga, M., Gelderen, P., Palumbo, S., Bosetti, F., Silva, A.C., Duyn, J.H., 2012. The contribution of myelin to magnetic susceptibility-weighted contrasts in high-field MRI of the brain. *Neuroimage* 59, 3967–3975.
- LeVine, S.M., 1997. Iron deposits in multiple sclerosis and Alzheimer's disease brains. *Brain Res.* 760, 298–303.
- Li, W., Wu, B., Liu, C., 2011. Quantitative susceptibility mapping of human brain reflects spatial variation in tissue composition. *Neuroimage* 55, 1645–1656.
- Liu, C., 2010. Susceptibility tensor imaging. *Magn. Reson. Med.* 63, 1471–1477.
- Liu, T., Spincemaille, P., de Rochefort, L., Kressler, B., Wang, Y., 2009. Calculation of susceptibility through multiple orientation sampling (COSMOS): a method for conditioning the inverse problem from measured magnetic field map to susceptibility source image in MRI. *Magn. Reson. Med.* 61, 196–204.
- Liu, C., Li, W., Johnson, G.A., Wu, B., 2011. High-field (9.4 T) MRI of brain dysmyelination by quantitative mapping of magnetic susceptibility. *Neuroimage* 56, 930–938.
- Liu, T., Xu, W., Spincemaille, P., Avestimehr, A.S., Wang, Y., 2012a. Accuracy of the morphology enabled dipole inversion (MEDI) algorithm for quantitative susceptibility mapping in MRI. *IEEE Trans. Med. Imaging* 31, 816–824.
- Liu, J., Liu, T., Rochefort, L., Ledoux, J., Khalidov, I., Chen, W., Tsiouris, A.J., Wisniew, C., Spincemaille, P., Prince, M.R., Wang, Y., 2012b. Morphology enabled dipole inversion for quantitative susceptibility mapping using structural consistency between the magnitude image and the susceptibility map. *Neuroimage* 59, 2560–2568.
- Luo, J., He, X., d'Avignon, D.A., Ackerman, J.J.H., Yablonskiy, D.A., 2010. Protein induced water 1H MR frequency shifts: contributions from magnetic susceptibility and exchange effects. *J. Magn. Reson.* 202, 102–108.
- Marques, J.P., Bowtell, R., 2005. Application of Fourier-based method for rapid calculation of field inhomogeneity due to spatial variation of magnetic susceptibility. *Concepts Magn. Reson. B Magn. Reson. Eng.* 25, 65–78.
- Mitsumori, F., Watanabe, H., Takay, N., Garwood, M., Auerbach, E.J., Michaeli, S., Mangia, S., 2012. Toward understanding transverse relaxation in human brain through its field dependence. *Magn. Reson. Med.* 68, 947–953.
- Neelavalli, J., Cheng, Y.-C.N., Jiang, J., Haacke, E.M., 2009. Removing background phase variations in susceptibility weighted imaging using a fast, forward-field calculation. *J. Magn. Reson. Imaging* 29, 937–948.
- Ogg, R.J., Langston, J.W., Haacke, E.M., Steen, R.G., Taylor, J.S., 1999. The correlation between phase shifts in gradient-echo MR images and regional brain iron concentration. *Magn. Reson. Imaging* 17, 1141–1148.
- Ordidge, R., Gorell, J., Deniau, J., Knight, R., Helpert, J., 1994. Assessment of relative brain iron concentrations using T2-weighted and T2*-weighted MRI at 3 Tesla. *Magn. Reson. Med.* 32, 335–341.
- Peters, A.M., Brookes, M.J., Hoogenraad, F.G., Gowland, P.A., Francis, S.T., Morris, P.G., Bowtell, R., 2007. T2* measurements in human brain at 1.5, 3 and 7 T. *Magn. Reson. Imaging* 25, 748–753.
- Pfefferbaum, A., Sullivan, E.V., Adalsteinsson, E., Garrick, T., Harper, C., 2004. Postmortem MR imaging of formalin-fixed human brain. *Neuroimage* 21, 1585–1595.
- Reichenbach, J., Venkatesan, R., Yablonskiy, D., Thompson, M., Lai, S., Haacke, E., 1997. Theory and application of static field inhomogeneity effects in gradient-echo imaging. *Magn. Reson. Imaging* 7, 266–279.
- Schenck, J.F., 1992. Health and physiological effects of human exposure to whole-body four-Tesla magnetic fields during MRI. *Ann. N. Y. Acad. Sci.* 649, 285–301.
- Schenck, J.F., Zimmerman, E.A., 2004. High-field magnetic resonance imaging of brain iron: birth of a biomarker? *NMR Biomed.* 17, 433–445.
- Schmierer, K., Wheeler-Kingshott, C.A.M., Tozer, D.J., Boulby, P.A., Parkes, H.G., Yousry, T.A., Scaravilli, F., Barker, G.J., Tofts, P.S., Miller, D.H., 2008. Quantitative magnetic resonance of postmortem multiple sclerosis brain before and after fixation. *Magn. Reson. Med.* 59, 268–277.
- Schweser, F., Deistung, A., Lehr, B.W., Reichenbach, J.R., 2011. Quantitative imaging of intrinsic magnetic tissue properties using MRI signal phase: an approach to in vivo brain iron metabolism? *Neuroimage* 54, 2789–2807.
- Schweser, F., Sommer, K., Deistung, A., Reichenbach, J.R., 2012. Quantitative susceptibility mapping for investigating subtle susceptibility variations in the human brain. *Neuroimage* 62, 2083–2100.
- Shmueli, K., de Zwart, J.A., van Gelderen, P., Li, T.Q., Dodd, S.J., Duyn, J.H., 2009. Magnetic susceptibility mapping of brain tissue in vivo using MRI phase data. *Magn. Reson. Med.* 62, 1510–1522.
- Shmueli, K., Dodd, S.J., Li, T.Q., Duyn, J.H., 2011. The contribution of chemical exchange to MRI frequency shifts in brain tissue. *Magn. Reson. Med.* 65, 35–43.
- Wallis, I.W., Paley, M.N.J., Graham, J.M., Grunewald, R.A., Wignall, E.L., Joy, H.M., Griffiths, P.D., 2008. MRI assessment of basal ganglia iron deposition in Parkinson's disease. *J. Magn. Reson. Imaging* 28, 1061–1067.
- Web, S.M., 2010. AIP Conf. Proc. 1365, 196–199. <http://dx.doi.org/10.1063/1.3625338>.
- Wharton, S., Bowtell, R., 2010. Whole-brain susceptibility mapping at high field: a comparison of multiple- and single-orientation methods. *Neuroimage* 53, 515–525.
- Yao, B., Li, T.Q., Gelderen, P.V., Shmueli, K., de Zwart, J.A., Duyn, J.H., 2009. Susceptibility contrast in high field MRI of human brain as a function of tissue iron content. *Neuroimage* 44, 1259–1266.
- Zheng, W., Haacke, E.M., Webb, S., Nichol, H., 2012. Imaging of stroke: a comparison between X-ray fluorescence and magnetic resonance imaging methods. *Magn. Reson. Imaging* 30, 1416–1423.
- Zhong, K., Leupold, J., von Elverfeldt, D., Speck, O., 2008. The molecular basis for gray and white matter contrast in phase imaging. *Neuroimage* 40, 1561–1566.